Universidade de Aveiro Departamento de Fisica
2017

Samaneh Ranjbarrizi

Desenvolvimento de Células Solares de Kesterite: Melhoria da Camada Absorvente e da Arquitectura da Célula

Development of Kesterite Solar Cell: Improvement of Absorber layer and Cell Architecture

Universidade de Aveiro Departamento de Fisica
2017

Samaneh Ranjbarrizi

Desenvolvimento de Células Solares de Kesterite: Melhoria da Camada Absorvente e da Arquitectura da Célula

Development of Kesterite Solar Cell: Improvement of Absorber layer and Cell Architecture

Dissertação apresentada à Universidade de Aveiro para cumprimento dos requisitos necessários à obtenção do grau de Doutor em Engenharia Física, realizada sob a orientação científica do Doutor António F. da Cunha, Professor Auxiliar do Departamento de Física da Universidade de Aveiro

Apoio financeiro da FCT e do FSE no âmbito do SFRH/BD/78409/2011 Quadro Comunitário de Apoio.

To my husband Reza.

o júri

presidente

Prof. Doutor João Carlos Matias Celestino Gomes da Rocha
Professor Catedrático, Departamento de Química,Universidade de Aveiro

Prof. Doutor João Manuel de Almeida Serra
Professor CatedráticoFaculdade de Ciências, Universidade de Lisboa

Prof. Doutor Luís Manuel Cadillon Martins Costa
Professor Associado com Agregação, Departamento de Fisica, Universidade de Aveiro

Prof. Doutor João Pedro Santos Hall Agorreta de Alpuim
Professor Auxiliar, Departamento de Fisica,Universidade do Minho

Prof. Doutor António Ferreira da Cunha
Professor Auxiliar, Departamento de Fisica, Universidade de Aveiro **(Orientador)**

Doutor Pedro Manuel Parracho Salome
Investigador, Laboratório Ibérico de Nanotecnologia (INL), Braga

Acknowledgments

After an interesting period of research in the past four years, writing this note to thank people who helped me to reach here. This period was a big learning opportunity and valuable experience for me; scientifically and personally. I had the opportunity to be supervised and to work with very good people that without their support, this accomplishment would not have been possible.
I would like to thank my PhD supervisor Prof. Dr. Antonio Cunha for his valuable guidance, immense knowledge, great support of my research and his patience with me. I appreciate his valuable time especially during the correction of this dissertation and his insightful comments.
I would like to thank CIGS TF-PV group in imec for their wonderful collaboration. A scientific group in a very friendly environment with excellent social interaction. During my internship in imec, I was supported and supervised by Dr. Marc Meuris, Dr. Guy Brammertz, and Dr. Bart Vermang. Their generous support, continuous encouragement, and excellent cooperation provided me valuable opportunities to excel my research. This internship was a big learning opportunity and valuable experience for me. I would like to thank Dr. Afshin Hadipour for his great contribution to my research. I would like to thank Prof. Dr. Jef Poortmans for his great support, kind attention and insightful comments.
It was a great pleasure to work in imec-PV lab with Sylvester, Souhaib, Aniket, Daniel, Nikhil, Siddhartha and Zijiang. I acknowledge the help of my colleagues, researchers, technicians and administrative staffs in imec.
I would like to thank my colleagues in I3N and University of Aveiro. Thanks to Prof. Dr. Rosário Correia for the help on Raman measurements. Thanks to Dr. Rajesh Menon for his help and contrinution. Thanks to my good friend Dr. Pegah Mirzadeh for helping me deal with the administrative issues when I was abroad. Also, I would like to acknowledge the administrative staffs of University of Aveiro and physics department for their kind attention and help.
I acknowledge FCT for financial support of my PhD program.
Countless thanks to my mother, my father, my sister and my brothers, for great love, support and encouragement throughout my life and during PhD study.
Last but not least, thank you, Reza. Thanks for your patience, love and support.

Samaneh Ranjbar

palavras-chave

Kesterite, $Cu_2ZnSnSe_4$ Células solares, absorvente de CZTSe, evaporacão por feixe de electrões, precursor, selenização, propriedades optoelectrónicas, passivação de interface, interface posterior de Mo/CZTSe, p-n junção

resumo

Células solares baseadas em *Kesterites,* $Cu_2ZnSn(S,Se)_4$ (CZTSSe), estão a ser investigadas como um alternativa de mais baixo custo às células solares de elevada eficiência baseadas em CIGS. Em compostos de *kesterite*, elementos abundandes na natureza como Zn and Sn são usados em vez de elementos raros como In e Ga na *calcopirite* CIGS. Mesmo tendo propriedades optoelectrónicas promissoras, como elevada absorcão e *bandgap* próximo do ideal, o desempenho das células solares de *kesterites* ainda fica aquém do requerido para a sua exploração em larga escala.

Nesta tese, são apresentadas três abordagens seguidas para melhorar o desempenho das células solares de CZTSe: modificacão de (1) camada absorvente de CZTSe, (2) da interface Mo/CZTSe e (3) da junção CZTSe/CdS.

O fabrico da camada absorvente de CZTSe é conseguido por meio de um processo em 2-passos, onde se inclui a evaporacão por feixe de electrões (*e-beam*) das camadas Sn/Zn/Cu precursoras seguida de um tratamento térmico rápido usando o gás de H_2Se (passo de *selenização*). São apresentados resultados do estudo de optimização da espessura, da ordem das camadas percursoras, e do caudal de H_2Se.

O efeito da espessura das camadas percusoras nas propriedades químicas e morfológicas do filme de CZTSe foi estudado. As propriedades optoelectrónicas foram investigadas por meio de medições da fotoluminescência resolvidas no tempo (TR-PL), curvas currente-tensão (J-V) e capacidade-tensão (C-V).

A interface posterior de Mo/CZTSe foi alterado através da introdução por meios químicos de uma película de MoO_3 na interface. A medição das curvas de currente-tensão das células solares com e sem MoO_3 foram efectuadas a diferentes temperaturas. O efeito da modificação da interface posterior nas propriedades optoelectrónicas de dois tipos de células com diferentes espessuras da camada absorvente foi estudado.

A junção CZTSe/CdS foi modificada pela introdução de uma camada ultra-fina de TiO_2. O efeito desta alteração nas propriedades optoelectrónicas da célula photovoltaica foi estudado.

Uma compreensão mais profunda da junção CZTSe/TiO_2/CdS foi alcançada por meio da realização de *microscopia electrónica de transmissão* e *da análise do perfil de composição química..*

Neste estudo foi possivel obter uma eficiência maxima de 7.8% para células solares com a estrutura: SLG/Mo/CZTSe/CdS/i-ZnO/AZO. Finalmente são apresentadas algumas sugestões para desenvolvimentos futuros, visto ser necessário mais optimização das condições de deposição dos precursores e da *sua selenização* para melhorar ainda mais a qualidade da camada absorvente e desempenho das células solares.

keywords

Kesterite, $Cu_2ZnSnSe_4$ solar cells, absorber layer, e-beam evaporation, selenization, opto-electronic characterization, interface passivation, rear contact, p-n jucntion.

abstract

Kesterite $Cu_2ZnSn(S,Se)_4$ (CZTSSe) solar cells are being investigated as a cost effective alternative for high efficiency CIGS solar cells. In kesterite, earth abundant Zn and Sn elements replace rare In and Ga in chalcopyrite CIGS. Despite promising optoelectronic properties of kesterite like high absorption coefficient and near to ideal band gap, the performance of kesterite solar cells is still lower than the required for large scale exploitation.

This thesis includes 3 main approaches to improve the performance of CZTSe solar cells: modification of (1) CZTSe absorber layer (2) Mo/CZTSe interface and (3) CZTSe/CdS junction.

We fabricated CZTSe absorber layer by a two-step approach including e-beam evaporation of Sn/Zn/Cu stacked precursors followed by an annealing step using H_2Se gas (selenization step) in a rapid thermal processing system.

Several parameters of the fabrication process were studied and suitable conditions of precursor thickness, precursor order, and H_2Se flow rate were presented.

The effect of thickness of precursors on chemical and morphological properties of CZTSe films was studied. The optoelectronic properties of the solar cells were investigated using time-resolved photoluminescence (TR-PL), PL, current density-voltage (J-V) and capacitance-voltage measurements.

Mo/CZTSe rear interface was modified by introducing a solution processed MoO_3 interfacial layer. Current-voltage curves of solar cells with and without MoO_3 layer were measured at different temperatures. The effect of the modification of rear surface on optoelectronic properties of two types of solar cells with thin and thick absorber layers was studied.

CZTSe/CdS junction was modified by introducing an ultra-thin TiO_2 layer. The effect of this modification on optoelectronic properties of solar cells was studied. Transmission electron microscopy and compositional profile analysis were performed to gain a deeper understanding of the CZTSe/TiO_2/CdS junction.

The best efficiency of a SLG/Mo/CZTSe/CdS/i-ZnO/AZO solar cell in this study was 7.8 %. Some suggestions for future work are presented. It is suggested that further optimization of the precursors and selenization conditions are required to improve the quality of absorber layer and the performance of solar cells.

Table of Contents

List of Figures

List of Tables

List of abbreviations and symbols

α	absorption coefficient (cm^{-1})
A	ideality factor
AM1.5	Air Mass 1.5
CBD	chemical bath deposition
CIGS	$Cu(In,Ga)Se_2$
CZTS	Cu_2ZnSnS_4
CZTSe	$Cu_2ZnSnSe_4$
CZTSSe	$Cu_2ZnSn(S,Se)_4$
EDS	energy dispersive spectroscopy
E_g	band gap energy (eV)
EQE	External quantum efficiency
FF	fill factor
FWHM	full width at half maximum
GDOES	glow discharge optical emission spectroscopy
η	conversion efficiency
h	Plank’s constant
I_{SC}	short circuit current
J_0	dark saturation current
J	current density
J_{SC}	short circuit current density
λ	wavelength
N_a	concentration of acceptors (cm^{-3})
N_d	concentration of donors (cm^{-3})
PV	photovoltaic
q	electron charge
RTP	rapid thermal processing
SLG	soda lime glass
SEM	scanning electron microscopy
TCO	transparent conductive oxide
TEM	transmission electron microscopy
TF	tube furnace
TR-PL	Time-resolved photoluminescence
υ	frequency
V	voltage
V_{OC}	open circuit voltage (V)
W	depletion width
XRD	X-ray diffraction

1 Introduction

1.1 Photovoltaics for renewable energy

One of the most important necessities in human life is energy. Despite recent development of renewable energy sources; the fossil fuels are the dominant source of energy. However fossil fuels can not last forever, they are the main source of greenhouse gas emissions and the price of these fuels is a challenging issue. On the other hand, there are renewable and environmentally friendly resources of energy like solar, wind, geothermal energy, biofuels, etc. There are enormous efforts to make these alternative energy resources economically viable to use, to meet the increasing demand for energy while reducing the side effects of fossil fuels. One of the most accessible and widely distributed resources of renewable energy is photovoltaic (PV), also known as solar energy. A photovoltaic device converts the sunlight into the electricity based on the photovoltaic effect. The solar energy is widely distributed and accessible in almost everywhere around the world. It can be harvested in small scale for rural electrification as well as in large scales for multi-megawatt power plants for big industries and city applications. These advantages do not widely apply to several renewable energy alternatives in terms of geographical availability or economic issues. Photovoltaic electricity generation still contributes only about 1% to the word's electricity generation [1]. The initial investment is the main obstacle to the wide application of PV energy as the main source of electricity generation. Further development of semiconductor industry and manufacturing techniques are required to reveal the full potential of photovoltaic energy.

1.2 Thin film solar cells

The first generation of solar cells is based on Si wafer technologies including two major categories, mono-crystalline Si and multiy-crystalline Si technologies. Although the conversion efficiencies of these traditional solar cells are quite high near the theoretical limits (up to 26.3 % and 21.3 % for mono-Si and multi-Si solar cells, respectively [2]), high embodied energy is required for their fabrication process.

Thin film solar cells including $Cu(In,Ga)(S,Se)_2$ (CIGS), $CuIn(S,Se)_2$ (CIS), CdTe and amorphous Si are the second generation of solar cells. Thin film solar cells are based on direct band gap semiconductors, thus only a few microns thickness of the absorber layer is enough to absorb the complete solar spectrum. In addition to the decrease of raw materials consumption, film solar cells are also less sensitive to the impurities as compared to the Si-wafer based solar cells, hence their production cost can be cheaper. Moreover, the possibility of producing transparent and flexible thin film solar cells can fulfill new applications such as large area building integrations, facades, windows, wearable devices, etc. So far, high conversion efficiencies up to 22.6 % and 22.1 % have been achieved in laboratory scale for CIGS and CdTe [2], respectively and commercial modules based on CIGS and CdTe technologies have been marketed. However, the use of rare and expensive elements such as Indium, Gallium and tellurium [3,4] and heavy metal Cd restricts significantly the production capacity of the mentioned technologies. Recently emerging thin film technologies such as kesterite, perovskite, organic solar cells, quantum dot solar cells, etc. have attracted the attention of PV community. Kesterite $Cu_2ZnSn(S,Se)_4$ (CZTSSe) has gained attention as an environmentally benign alternative to the leading technologies CIGS and CdTe. Kesterite CZTSSe has some similar optoelectronic properties with high efficient chalcogenide CIGS and it consists of earth abundant and inexpensive elements. While the air and temperature stability is an issue for the emerging PV technologies such as perovskite solar cells, kesterite solar cells have a good air and temperature stability.

1.3 $Cu_2ZnSn(S,Se)_4$ Crystal structure

CZTSSe is derived from the chalcopyrite structure of $CuInS_2$ by replacing In atoms with Sn and Zn atoms, as illustrated schematically in **Figure 1-1**. This substitution leads to two main crystal structures: (i) kesterite (space group I4) and (ii) stannite (space group I4 2m). These tetragonal structures are very similar. The only difference is the stacking order of Cu and Zn along the c-axis. In kesterite structure, Cu-Sn/Cu-Zn/Cu-Sn cationic layers are arranged along the c-axis. In stannite structure, the arrangement is Cu/Zn-Sn/Cu as shown in **Figure 1-2** [5,6]. It’s not easy to distinguish kesterite and stannite structures by X-Ray diffraction due to the very similar atomic form factor of Cu^{2+} and Zn^{+} that are neighbors in the periodic table. Neutron scattering can be used to determine the cation distribution in CZTSSe as Cu and Zn have different neutron scattering length [7,8]. According to ab initio calculations kesterite has slightly lower formation energy, as compared to the stannite phase, thus it is thermodynamically more stable [9]. S. Schorr suggested that CZTS have a phase transition from kesterite to stannite at around 870 °C [8].

I	II	III	IV	VI	
	Cd			Te	II-VI
Cu		In		Se	I-III-VI_2
Cu	Zn		Sn	S/Se	I_2-II-IV-VI_4

Figure 1-1 CZTSSe is derived from the chalcopyrite structure of $CuInS_2$ by replacement of In atoms with Sn and Zn atoms.

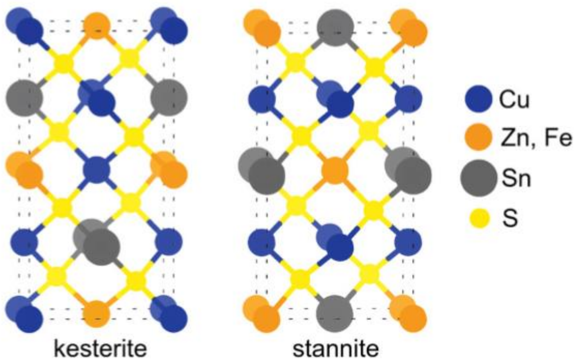

Figure 1-2 Illustration of kesterite and stannite structures [5].

1.4 Optoelectronic properties of CZTSSe

The optical studies indicate that CZTSSe is a direct band gap p-type semiconductor with an absorption coefficient above 10^4 cm^{-1} that is suitable for photovoltaic applications. Band gap has been estimated to be around 1.0 eV for $Cu_2ZnSnSe_4$ [10] and 1.5 eV for Cu_2ZnSnS_4 [11]. Several groups have tried to tune the band gap by: (i) adding both S and Se anions to the compound and changing the S/(S+Se) ratio [12,13], (ii) substituting part of the Sn amount with Ge [14] or Si [15–17] and part of Cu amount with Ag [18].

1.5 Defects

Defects have an important impact on the optoelectronic properties of semiconductors. Doping of CZTSSe is due to the intrinsic defects, similar to the intrinsic doping properties of CIGS. Doping density in CZTSSe is reported in the range of 10^{15} to 10^{20}cm^{-3}[19–22], depending on the sample preparation condition and the composition of the kesterite compound [23–25]. Usually, the shallow defects contribute to the carrier concentration of the material while the deep defects act as traps and recombination centers. There are several possible intrinsic point defects in kesterite structure such as vacancies (V_{Cu}, V_{Zn}, V_{Sn} and $V_{(S,Se)}$), antisites (Cu_{Zn}, Zn_{Cu}, Cu_{Sn}, Sn_{Cu}, Zn_{Sn} and Sn_{Zn}) and self-interstitial defects (Cu_i, Zn_i and Sn_i) [21]. Chen et al. calculated transition-energy levels for the mentioned intrinsic defects, as shown in **Figure 1-3** [21]. Formation of the mentioned point defects in kesterite depends on the stoichiometry. According to the literature carrier concentration of kesterite is mainly due to the Cu_{Zn} acceptor defects. Formation of donor defects such as Zn_{Cu} and compensated cluster defects such as [Cu_{Zn}+Zn_{Cu}] and [V_{Cu}+ Zn_{Cu}] are also likely. These defects lead to a p-type conductivity for CZTSSe along with a high degree of compensation [21].

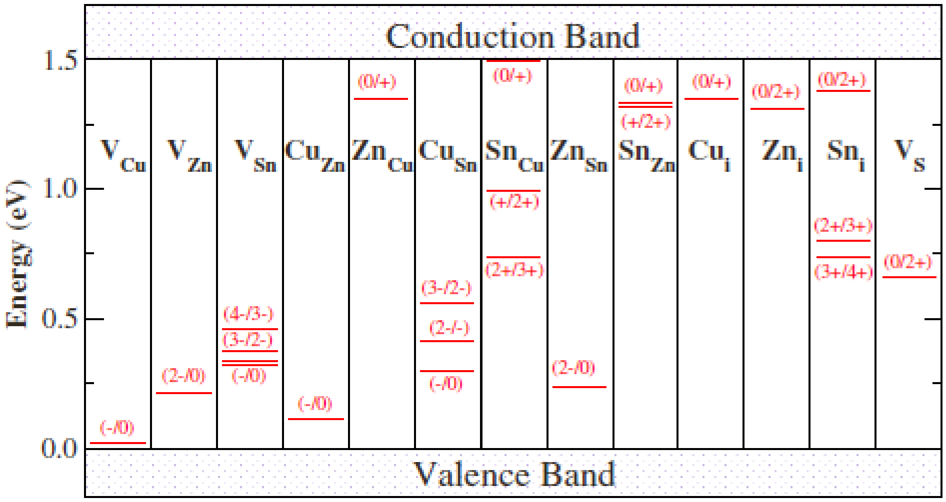

Figure 1-3 The transition energy levels of the intrinsic defects in the band gap of CZTS [21].

1.6 Formation reaction of CZTSSe

F. Hergert and R. Hock proposed there are two reaction paths for the formation of CZTSSe based on crystallographic models:

(i) $Cu_2X/CuX + ZnX + SnX/SnX_2 \rightarrow CZTX$

(ii) (a) $CuX_2/CuX + SnX/SnX_2 \rightarrow Cu_2SnX_3$

(b) $Cu_2SnX_3 + ZnX \rightarrow CZTX$

Where X is the chalcogen S or Se [26]. By applying in-situ X-ray diffraction measurements during the annealing process of electrodeposited Cu–Zn–Sn precursor, Schurr et al. also showed the formation of kesterite happens through a solid state reaction between Cu_2SnS_3 and ZnS. They showed the formation of Cu_2SnS_3 can be through two different reaction paths depending on the metallic ratios of the precursors [27].

1.7 Secondary phases

Fabricating high-quality single phase CZTSSe is very challenging because of (i) a narrow stable region of CZTSSe in the phase diagram, (ii) decomposition reactions at the rear and the top surface of CZTSSe during the annealing process in S or Se atmosphere. As shown in section 1.6, CZTS(Se) can be synthesized through chemical reactions between ZnS(Se), $Cu_2S(Se)$, and $SnS(Se)_2$. Olekseyuk et al. presented a phase diagram of the Cu_2S–ZnS–SnS_2 pseudo-ternary system at 670 K. According to this phase diagram, shown in **Figure 1-4**, single phase Cu_2ZnSnS_4 exists only in a very narrow region (region 1 in **Figure 1.4**). In all other regions, there are always some secondary phases along with CZTS [28]. Hence the formation of secondary phases such as ZnS(Se), $SnS(Se)_x$, $CuS(Se)_x$, and $Cu_2SnS(Se)_3$ are likely in off-stoichiometric region. $SnS(Se)_x$, $CuS(Se)_x$ and $Cu_2SnS(Se)_3$ have low band gap and they can reduce the shunt resistance significantly. Highest efficiencies for CZTSSe so far is recorded for Cu-poor and Zn-rich regime of the phase diagram in which formation of low band gap $SnS(Se)_x$, $CuS(Se)_x$ and $Cu_2SnS(Se)_3$ are less likely [29,30]. ZnS(Se) is shown to be the dominant secondary phase under the Cu-poor and Zn-rich growth condition. ZnS(Se) has a wide bandgap

(~3.54 eV for ZnS and ~2.82 eV for ZnSe) and it is not considered as a very harmful phase. However, the formation of big clusters of ZnS(Se) can decrease the active region of the absorber layer and decrease the J_{SC}. A Zn-rich composition leads to a spatial inhomogeneity and it may lead to band gap fluctuation since the different phases in the compound have different band gaps.

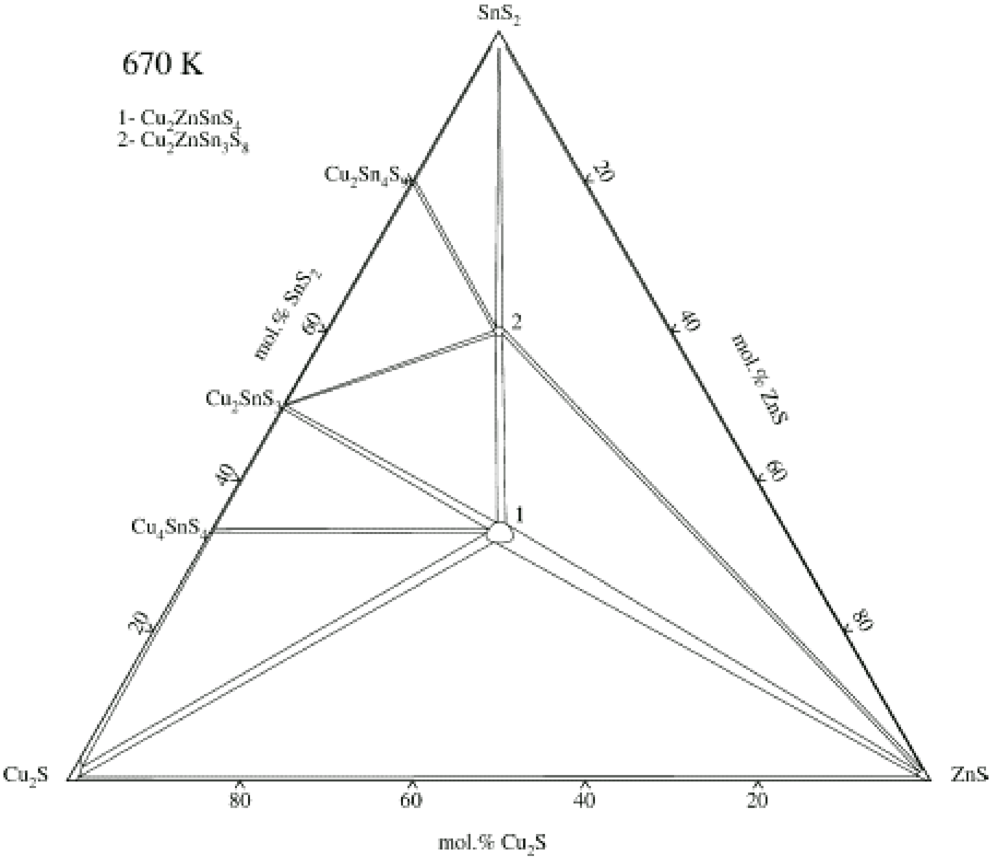

Figure 1-4 Phase diagram of Cu_2S–SnS_2–ZnS system at 670 K [10].

1.7.1 Decomposition reactions

In addition to the very narrow single-phase regime in the phase diagram, decomposition reactions that happen during the annealing step lead to the formation of secondary phases. These reactions at (i) Molybdenum (Mo) rear interface and (ii) top surface of CZTSSe make the fabrication of single-phase kesterite compound even more challenging. Scragg et al. showed the instability of Mo and easily reduction of Sn during the selenization/sulfurization process can lead to the decomposition of CZTSSe [31,32]. This decomposition reaction can be shown by this reaction:

$$2Cu_2ZnSnSe_4 + Mo \rightarrow 2\ Cu_2Se + 2\ ZnSe + 2\ SnSe + MoSe_2$$

Thus the formation of detrimental secondary phases such as $CuS(Se)_x$, SnSe and $MoSe_2$ are very likely at the rear surface. The decomposition of CZTSSe at the rear surface also leads to the formation of voids in this region. The existence of voids and secondary phases at Mo/CZTSSe rear surface is widely reported in kesterite solar cells [31,33,34]. These imperfections at the rear surface are detrimental to the performance of solar cells. The pores at the rear surface are not good for the adhesion of the film and they can suppress the charge carrier transport and decrease the J_{SC}. The decomposition of CZTSSe at the rear interface may introduce deep defects such as Se and Sn vacancies that increase the recombination rate at the rear interface and decrease of the open circuit voltage (V_{OC}). To avoid the decomposition reaction at the Mo rear interface, introducing an inert interfacial layer between Mo and CZTSe such as TiN [32,35], ZnO [36], TiB [34], Ag [37], MoO_{3-X} [38], etc has been suggested by several groups.

Decomposition of CZTSSe from the top surface during the selenization/sulfurization is also reported in the literature. Weber et al. indicated a decomposition reaction for CZTS from the top surface through the reactions shown schematically in **Figure 1-5**. According to their study evaporation of SnS and consequently Sn loss is significant at pressures around 10^{-2} Pa and temperature above 350 $^{\circ}$C but this decomposition can be suppressed by using inert gasses and increasing the pressure during the annealing process [39].

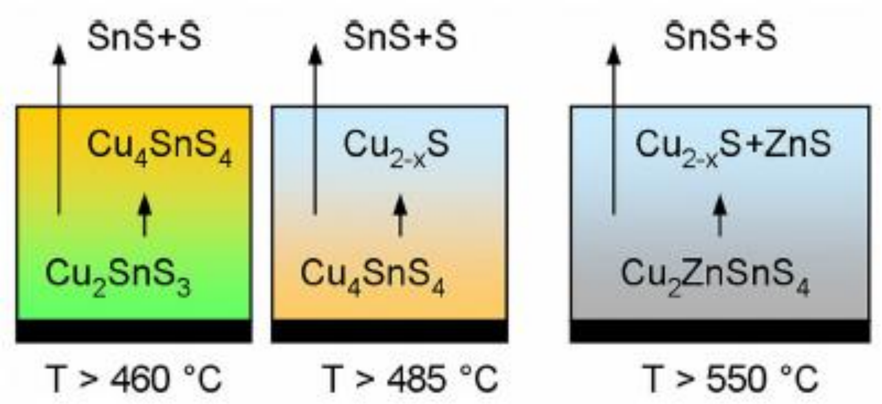

Figure 1-5 Schematic representation of reactions at the top surface of CZTS [39].

1.8 Fabrication techniques of kesterite

Generally, the fabrication methods of kesterite compound can be classified into one-step and two-step methods and these methods also can be also divided into the vacuum and non-vacuum techniques. In one-step methods, all the elements are incorporated into the kesterite compound in one step. In two-step techniques, first, a precursor containing only the metals or metals and a small amount of sulfur is deposited at low temperatures by vacuum or non-vacuum techniques. In the second step, the as-deposited precursors are annealed using Sulfur/Selenium vapor or H_2S/H_2Se gas. The two-step methods are more common in kesterite technology and generally, most of the best efficiencies for kesterite solar cells have been reported by two-step techniques [19].

1.8.1 Vacuum-based deposition methods

The vacuum-based methods usually include physical vapor deposition (PVD) techniques such as evaporation techniques, DC and RF magnetron sputtering and pulsed laser deposition. Cu_2ZnSnS_4 (CZTS) material was firstly reported in 1988 by Ito and Nakazawa at Shinshu University, using a sputtering technique [40]. In 1996, Katagiri et al prepared the first CZTS thin film solar cell with an SLG/Mo/CZTS/CdS/TCO structure. CZTS thin films were prepared by an e-beam evaporation of Zn/Sn/Cu stack, followed by a sulfurization using H_2S at 500 $^{\circ}$C.

This first CZTS solar cell had a conversion efficiency of 0.66 % and an open-circuit voltage of 400 mV [41]. This group continually improved the fabrication techniques of CZTS absorber layer. Using co-sputtering technique and optimizing the sulfurization condition they achieved 6.7% efficiency in 2009 [42]. Since then different groups prepared CZTS and CZTSSe solar cells using vacuum based deposition of precursors followed by annealing in chalcogenide gas. In 2008 Moriya et al fabricated a CZTS solar cells using pulsed laser deposition (PLD) technique with 0.64 % efficiency and 336 mV V_{OC} [43]. So far the highest efficiency of 5.85 % is reported for a CZTS solar cell prepared by PLD technique [44]. Wang et al. (2010) fabricated CZTS solar cells by thermal evaporation of precursors followed by annealing in Sulfur vapor and they reported 6.8 % conversion efficiency and 587 mV V_{OC}. K. Sun et al. prepared CZTS solar cells by sulfurization of co-sputtering of Cu/ZnS/SnS precursors within sulfur containing atmosphere. They achieved 9.2 % efficiency for solar cells with $Zn_{1-x}Cd_xS$ buffer layer [45]. G. Brammertz et al. prepared CZTSe solar cells by selenization of DC sputtered $Cu_{10}Sn_{90}$/Zn/Cu stack followed by selenization using H_2Se gas and they achieved up tp 9.7 % efficiency for solar cells with 1 cm^2 area in 2013 [46]. Lee et al. reported a CZTSe solar cell with 11.6 % and 0.43 cm^2 area using thermal co-evaporation technique followed by selenization on a hot plate [47].

1.8.2 Nonvacuum deposition methods

Non-vacuum techniques such as spray-pyrolysis, electrochemical deposition and spin coating are promising techniques for cost effective and easy fabrication of kesterite compounds. K.Woo et al. reported an ethanol-based ink technique for preparation of CZTSSe absorber layers and they reported the fabrication of CZTSSe solar cell with 7.2 % efficiency [48]. Mitzi et al. reported the highest efficiency of 12.6 % for CZTSSe kesterite solar cells using a hydrazine solution based process [49,50]. However, this method is not suitable and economical for large scale productions due to the use of hydrazine reagent.

1.9 Structure of kesterite solar cell

The structure of CZTSSe solar cells is adopted from CIGS solar cells. In **Figure 1-6** (left) a CZTSSe solar cell structure is illustrated schematically, a SEM image of this multilayer structure is also shown in **Figure 1-6** (right). This adopted structure may not be the ideal structure for kesterite solar cell and it can be modified in order to enhance the performance of the kesterite solar cells. Several studies indicated that Mo is not an ideal back contact for kesterite solar cell as it is unstable during the fabrication of absorber layer [31,51]. The band alignment between Mo back contact and kesterite absorber layer is the second issue regarding the back contact in kesterite solar cells. Mo/CZTSSe rear interface is reported to be a Schottky barrier [52], however, the formation of a MoS_2/$MoSe_2$ layer at the rear surface can lead to an ohmic contact [53]. Although a few studies reported on using alternative back contacts including transparent conducting oxide glass substrates such as ITO and FTO [54] in kesterite solar cells, so far Mo-coated glass substrate was the most common back contact. It is suggested that using interfacial layers is beneficial to enhance the quality of rear surface and consequently the performance of the kesterite solar cells [32,33,35,36,38,51,55].

The other important layer in kesterite solar cell is the n-type layer, known as buffer layer. CdS layer is the most common buffer layer in kesterite solar cells and the best efficiency has been achieved using this buffer layer [50]. A few studies also reported alternative buffer layers such as $Zn_{1-x}Sn_xO_y$ [56], $Zn_{1-x}Cd_xS$ [45] and ZnS [57] in kesterite solar cells. Theoretical studies indicated the band alignment between the buffer layer and absorber layer affects the electrical properties of the solar cells [58]. The band alignment between CdS buffer layer and CZTS is a

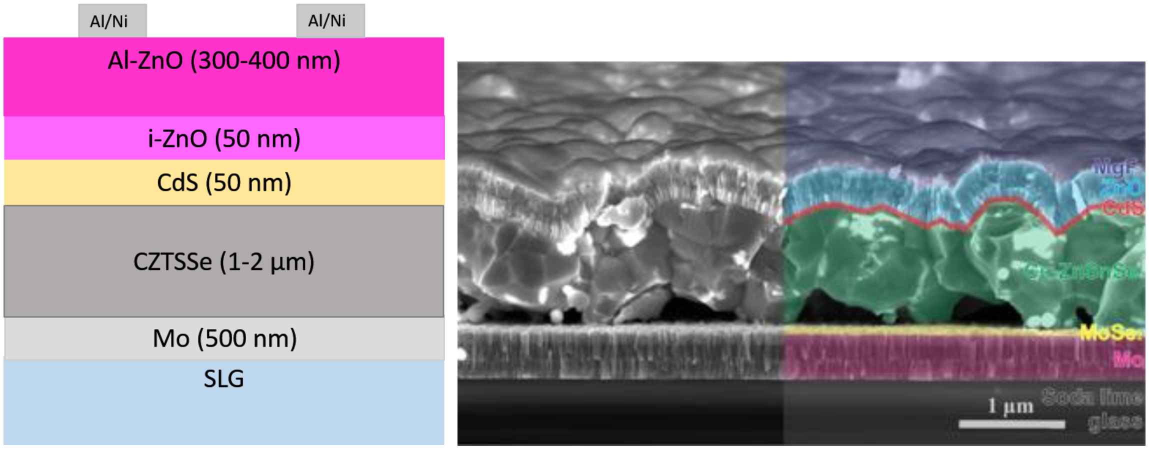

Figure 1-6 Scheme of a standard kesterite solar cell (left) and cross-sectional SEM image of a CZTSe solar cell (right).

cliff-like band alignment in which the conduction band of the absorber layer is higher than the one in CdS [59]. The cliff-like band alignment can be a barrier to the injected electrons under forward bias, thus increase the recombination at the p-n junction and decrease the V_{OC} [58]. The CZTSe/CdS is reported to be a spike-like band alignment with an offset below 0.4 eV. A spike-like band alignment is not a barrier for the injected electrons but for the photo-generated electrons. If the conduction band offset is lower than 0.4 eV the photo-generated electrons can transport by thermionic emission. Thus a spike like band alignment does not decrease the V_{OC} but it may decrease the J_{SC} if it is higher than 0.4 eV [58]. Another issue regarding the kesterite/CdS buffer layer interface is the presence of defects and dangling bonds [60,61]. Passivation of the p-n junction can decrease the recombination via these defects and improve the V_{OC}. So far ultra-thin interfacial layers such as Al_2O_3 and TiO_2 layers deposited by atomic layer deposition (ALD) techniques are used for passivation of a p-n junction in kesterite solar cells [60–62].

1.10 Kesterite solar cells challenges

Kesterite compounds are considered as promising candidates for cost-effective and abundant thin film solar cells. However, so far device performance of kesterite solar cells is limited to around 12 % that is still far away from the commercial level. One of the main flaws of kesterite solar cell is its low open circuit voltage (V_{OC}), thus a large V_{OC} deficit from the bandgap ($E_g/q-V_{OC}$). Many theoretical and experimental studies have been dedicated to understanding the main reasons for large V_{OC} deficit and reduce it. These efforts can be categorized to three main approaches: (1) Improving the absorber layer to reduce the bulk recombination via the tail states and potential fluctuations in the bands. The high density of charged defects [63,64], Cu-Zn disorders [65], secondary phases [66,67], grain boundaries [68], etc. are counted as the possible reasons of the tail states in kesterite compounds. (2) Improving the rear contact by introducing an interfacial layer such as TiN [32,51,69], MoO_{3-X} [33,38], etc., between Mo and absorber layer in order to address two main problems that are attributed to the Mo rear contact in kesterite solar cells: (i) the decomposition reactions at the rear interface due to the instability of Mo rear contact that leads to the formation of secondary phases and voids at the rear surface, (ii) a Schottky barrier at the Mo/kesterite interface that decreases the hole transport and increases the recombination at the rear interface. (3) Improving the p-n junction in kesterite solar cells by: chemical cleaning using KCN [70,71], ammonium sulfide [72], etc. to remove the secondary phases, optimization of CdS buffer layer deposition [73,74], introducing ultra-thin interfacial metal oxides like Al_2O_3 [61,62] and TiO_2 [60] to passivate the p-n junction, and introducing alternative buffer layers [45,56,57].

1.11 The structure of this research

In this thesis, several approaches are investigated in order to overcome the three main problems in kesterite solar cells: absorber layer, Mo back interface and CZTSe/CdS p-n junction. Improving the bulk quality of the absorber layers is our main objective in chapter 3,4 and 5. We studied several processing parameters in order to improve the CZTSSe and CZTSe absorber layer. In chapter 6 the issues related to the Mo rear contact are discussed and a solution processed MoO_{3-X} layer is introduced to improve the back contact. In Chapter 7 an ultra-thin layer of TiO_2 is introduced for passivation of the p-n junction.

2 Experimental techniques

Fabrication of CZTSSe and CZTSe thin films in this study was performed by a two-stage process, the first step consists of deposition of precursors on Mo-coated SLG and the second step includes annealing the precursors in the Se-containing atmosphere. Deposition of Zn/SnS_2/CuS precursors was performed in PV lab of the University of Aveiro, using a hybrid thermal evaporation/RF-sputtering system. Deposition of metallic Sn/Zn/Cu precursors was performed in imec- PV lab using an e-beam evaporation technique.

2.1 Preparation of Mo-coated SLG substrates

In this study, Mo-coated SLG was used as the back contact in CZTSe solar cells. In PV lab of the university of Aveiro, we deposited Mo on 1 mm thick 3×3 cm^2 SLG substrates using a DC sputtering system as will be explained in next section. In imec PV lab, we used 3 mm thick SLG substrates on which a 400 nm of Mo was deposited by Guardian company. We cut the Mo-coated SLG sheets into 5×5 cm^2 substrates. Then to remove the oxides, fingerprints, and organic residues from the surface of the substrates, we cleaned the substrates by soaking in a 1 molar NH_4OH solution for 3 min, rinsing in deionized water and drying with an N_2 gun.

2.1.1 Deposition of Mo using DC sputtering

Sputtering is a physical vapor deposition (PVD) technique. In the sputtering system a target acts as a cathode and is connected to a high direct current/alternating current (DC/RF). Anode is the substrate holder that is grounded. In the evacuated chamber, a noble gas such as Ar is introduced to create a plasma environment. A glow discharge is initiated By applying a critical voltage and the collision of energetic ions ejects target atoms which are deposited on the substrate [75]. In magnetron sputtering, a magnetic field is applied in order to confine the electrons near the target vicinity. The trapped electrons have more chance to collide with argon atoms. Magnetron sputtering allows to reduce the working gas pressure; thus particles collide the substrate with higher energy that leads to higher deposition rates. In addition by trapping the electrons near the target the substrate temperature is reduced and the quality of the film improves [75].

We deposited Mo on 3×3 cm^2, 1 mm thick soda-lime glasses (SLG) substrates. SLG substrates were cleaned in consecutive ultrasonic baths of acetone, ethanol and deionized water for 10 min each and dried using an N_2 flux. A bilayer Molybdenum (Mo) film was deposited on the cleaned substrates using a DC magnetron sputtering system in which the distance between the substrates and target was 10 cm. The Mo target purity was N3. The base pressure of the chamber was about 5×10^{-6} mbar before the deposition using a turbo pump backed by a rotary pump. Using Ar as the sputtering gas, the work pressure in the chamber could be changed between 1×10^{-3} and 1×10^{-2} mbar. A bilayer Mo was sputtered in a two-step deposition process. First, an ultra-thin layer of Mo was sputtered using 0.04 kW power for 2 min at a high working pressure of 2×10^{-2} mbar. In the second step, Mo was deposited at 0.1 kW power for 6 min at a low pressure of about 10^{-3} mbar. This deposition recipe had been already optimized by Salome et.al [76]. The reason of two-step deposition first at high and then low pressure is to achieve good adhesion along with low resistivity for the Mo film to be a good ohmic contact for the high-temperature process kesterite solar cell. The sheet resistances of the Mo-coated films were measured using a four point probe to be below 1 **Ω□**.

2.2 Deposition of multi-stacked Zn/SnS_2/CuS precursors

When the target is a conducting material a direct current (DC) is appropriate for the sputtering however sputtering of an insulator target leads to accumulation of positive charges. To avoid the charge build up, an alternating current (AC) voltage is applied in radio frequency (RF) sputtering and an impedance matching network is required between the power supply and the discharged chamber [75].

We prepared SLG/Mo/8×(Zn/SnS_2/CuS) stacks using a hybrid evaporation/sputtering system. Thermal evaporation was used for deposition of Zn because of the availability of this system in our lab and also because evaporating elemental Zn has been found to be more reproducible than sputtering while RF sputtering of SnS_2 and CuS was reproducible. In this process, Zn pellets with purity of N5 were thermally evaporated while SnS_2 and CuS were sputtered successively using RF magnetron sputtering of the compound targets. The purity of SnS_2 and CuS targets was N4. This process was repeated in eight periods to prepare multi-stacked layers of precursors. The deposition times were set to deposit 180 nm of Zn, 320 nm of SnS_2 and 660 nm of CuS, confirmed by step profilometry. The base pressure of the deposition chamber was about 10^{-5} mbar before the deposition using a diffusion pump backed by a rotary pump. The deposition was done in an Ar atmosphere at a working pressure of 4.0×10^{-3} mbar.

2.3 Deposition of Sn/Zn/Cu precursors

In electron beam evaporation technique (also known as e-beam) a beam of electrons scan the surface of the source material and evaporate or sublimate it from the surface. By applying a very high voltage (10 kV) to a filament an electron beam will create. This beam is magnetically directed into the crucible where the source material is placed. The crucible is water cooled in order to avoid the diffusion of impurities from the crucible. Usually, we use graphite crucible for Sn, Zn, and Cu. Sn, Zn, and Cu were deposited sequentially on Mo-coated SLG substrates by e-beam evaporation in a Pfeiffer PLS 580A tool. The tool was a multiple crucible rotary e-Guns so deposition of multilayer stacks of different materials in one deposition run was possible. Before starting the deposition a base pressure of about 10^{-5} mbar was achieved after 1-hour pumping using a turbo-pump. Sn/Zn/Cu stack precursors were deposited in 1 deposition run without breaking the vacuum by 10 kV accelerating voltage and the deposition rate was 1 nm/s for Sn and Cu and 0.7 nm/s for Zn. The electron beam was swept on the surface of the target in a triangular pattern during the deposition to heat the material more evenly. The thickness of the coated film was controlled by a quartz crystal. Samples were rotated during the deposition for improving the homogeneity of the films. In each e-beam evaporation, we could deposit 18 samples.

2.4 Selenization in rapid thermal processing system

Pure selenide CZTSe absorber layers were prepared by selenization of SLG/Mo/Sn/Zn/Cu precursors in a rapid thermal processor (RTP) using an AnnealSYS AS-One 150 tool. The schematic of RTP system is depicted in **Figure 2-1**. **Figure 2-2 (left)** shows our RTP chamber when it is in the open position. The system was attached to N_2, H_2, H_2Se and H_2S lines and an XDS5 dry scroll pump to avoid oil contamination in the chamber. It was possible to perform the annealing under vacuum or up to 1 atm in the presence of an N_2 background. The heating was performed from the top with halogen lamps. A thermocouple inserted to the graphite susceptor to control the temperature. The standard selenization process includes annealing the SLG/Mo/Sn/Zn/Cu precursors using 10 % H_2Se gas diluted in N_2 for 15 min at 460 °C with 1 °C/s heating rate, as this selenization receipt is shown in Figure 2-2 (right).

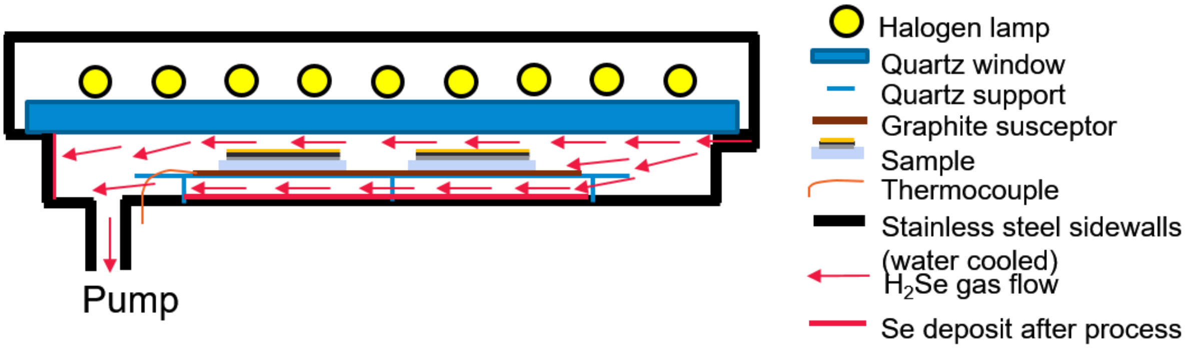

Figure 2-1 Scheme of selenization chamber

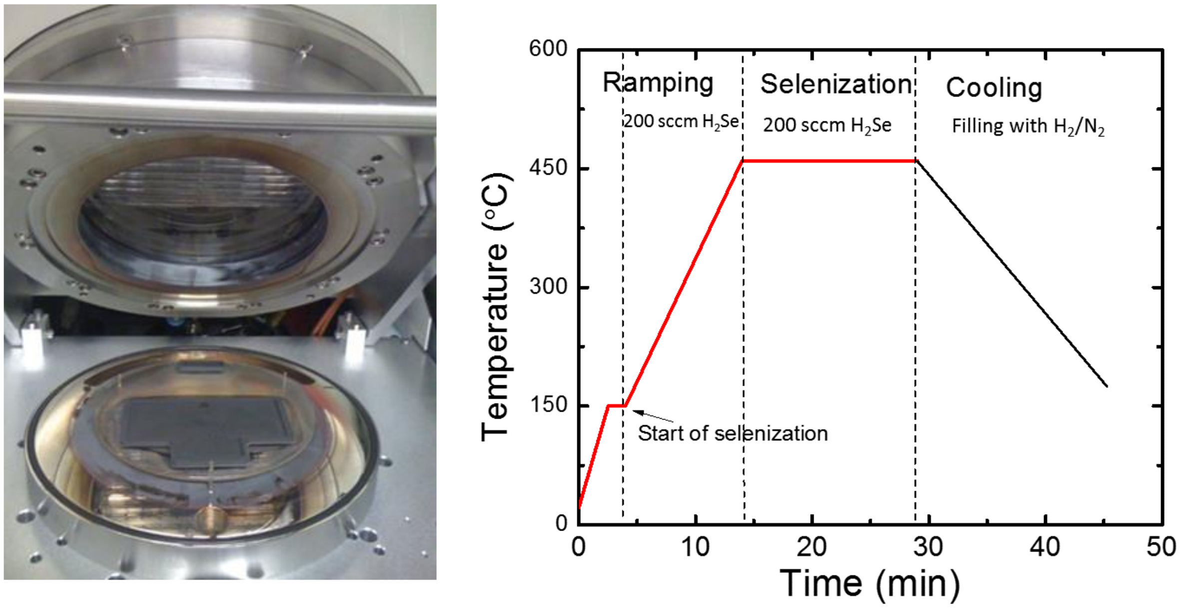

Figure 2-2 RTP chamber in its open position (left) selenization recipe (right).

2.5 Solar cell processing

The as-deposited absorber layers were subjected to a standard KCN treatment in which samples were dipped in a 5 wt % KCN solution in H_2O for 2 min, followed by rinsing the samples in deionized water and drying with an N_2 gun. KCN etching is beneficial for improving the performance of the CZTSe solar cells performance because it removes secondary phases such as Cu_xSe, SnSe, Se and oxides such as SnO as shown in [70]. The CdS was deposited as an n-layer by chemical bath deposition at 65 $^{\circ}$C using $Cd(CH_3CO_2)_2$ and $SC(NH_2)_2$ in the aqueous NH_3 medium for 7 minutes. Solar cells were then completed by successive RF magnetron sputtering of intrinsic ZnO (~ 50 nm) and Al-doped ZnO (~ 300-400 nm) and finally e-beam evaporation of a Ni (50 nm)/Al (1µm)/Ni (50 nm) finger contact pattern through a shadow mask. Solar cells with 0.5 cm^2 area were laterally isolated by needle scribing of the devices. **Figure 2-3** shows the picture of one of our devices including 32 solar cells.

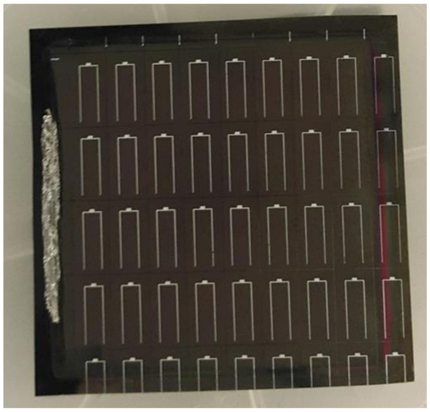

Figure 2-3 One of the devices fabricated in this study including 32 solar cells.

2.6 Characterization techniques

2.6.1 Current density-voltage measurement

Current density-voltage measurement (J-V) under standard illumination condition, 100 mW/cm^2 AM1.5 spectrum at 25 $^{\circ}$C is one of the most important methods for characterizing the solar cells. Open circuit voltage (V_{OC}), short-circuit current density (J_{SC}), fill factor (FF) and solar cell efficiency (η) can be determined directly from the illuminated J-V curve, as shown in **Figure 2-4**. J_{SC} is the current density when voltage is zero. V_{OC} is the voltage when current is zero. FF is the ratio of the product of voltage and current density at the maximum power obtained from the solar cell (V_{mp} and J_{mp}) to the product of V_{OC} and J_{SC}. Efficiency is defined as the fraction of the incident power that is converted to the electricity:

$$\eta = \frac{P_{out}}{P_{in}} = \frac{V_{of} \times I_{sc} \times FF}{P_{in}} \qquad \text{Equation 2-1}$$

Where I_{SC} is the short circuit current. η is measured under standard illumination condition 100 mW/cm^2 AM1.5 spectrum, thus the input power for our typical solar cells with 0.5 cm^2 area is 50 mW.

The J-V curve of an ideal solar cell can be obtained by superposition of the J-V curve of solar cell diode in dark plus the photo-generated current (J_L):

$$J\,(V) = J_0\left[\exp\left(\frac{qV}{kT}\right) - 1\right] - J_L \qquad \text{Equation 2-2}$$

Where J_0 is the dark saturation current. In a thin film solar cell, the effect of parasitic losses has to be considered, therefore for a real solar cell:

$$J\,(V) = J_0\left[\exp\left(\frac{q(V-R_sJ)}{AkT}\right) - 1\right] + \frac{V-R_sJ}{R_{sh}} - J_L \qquad \text{Equation 2-3}$$

Where R_s is series resistance, R_{sh} is shunt resistance and A is ideality factor. The R_s, R_{sh}, A and J_0 can be determined from illuminated and dark J-V curves using a procedure explained by Hegedus and Shafarman [77]. This procedure is illustrated in **Figure 2.5** and is explained in the following steps. The illuminated and dark J–V characteristics were measured using an AM1.5 g Oriel solar simulator system and a MATLAB code was used for the J-V analysis.

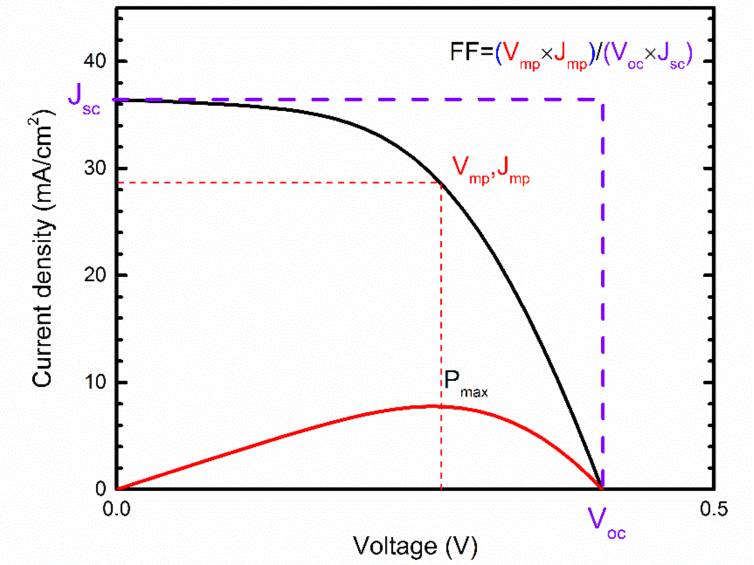

Figure 2-4 Current density (black line) and power (red line) versus voltage for a typical CZTSe solar cell. The short-circuit current density (J_{sc}), open-circuit voltage (V_{oc}) points and the maximum power point (V_{mp}, I_{mp}) are marked in the curve.

(a) A linear plot of illuminated and dark J–V curve with sufficient data. Usually, for CZTSe solar cells we measure J-V curves from -1.0 to 1.0 V.

(b) A plot of derivative of J with respect to V (dJ/dV) near J_{sc} and in reverse bias determines the shunt conductance, $G = 1/R_{sh}$. Shunt resistance can be obtained as the reverse of shunt conductance from illuminated and dark J-V curves as shown in **Figure 2.5b**.

(c) A plot of dV/dJ versus $(J+J_{sc})^{-1}$, will yield a straight line with intercept R_s assuming that photogenerated current J_L is voltage independent and $J_L = J_{sc}$. A linear fit to this curve gives an intercept of R_s and a slope AkT/q from which A can be calculated.

(d) A semilogarithmic plot of J-V after corrections for R_{sh} and R_s. Applying a linear fit to the corrected J-V plot, the intercept gives J_0 and the slope is q/AkT. This value of A agrees with the value obtained in step 3 for well-behaved solar cells.

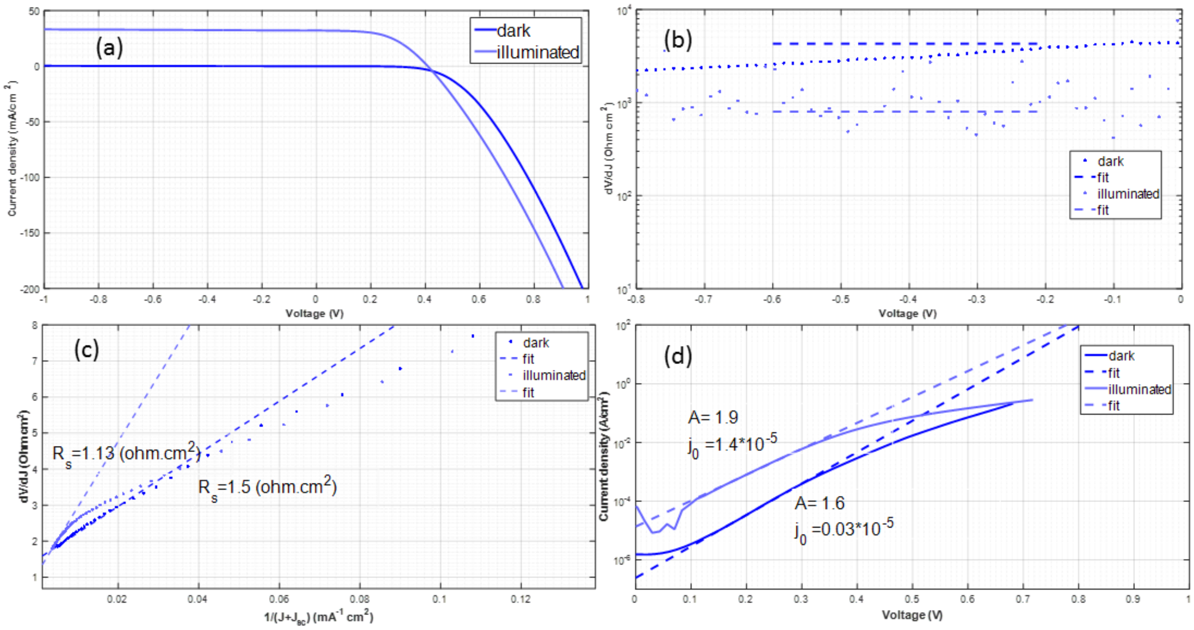

Figure 2-5 Hegedus and Shafarman procedure to obtain diode parameters from the J-V curve, (a) dark and illuminated J-V, (b) shunt resistance obtained by dV/dJ in the range of (-0.1,0) V, (c) series resistance obtained in the range of (0.9,1.0) V and ideality factor (A) and J_0 obtained by a log plot of corrected J-V.

2.6.2 Capacitance-Voltage (C-V) measurement

Capacitance-voltage (C-V) measurements were performed to obtain the doping concentration and the depletion width of CZTSe solar cells. The C-V was measured at room temperature using an Agilent 4980A LCR-meter as a function of frequency varying from 10 kHz to 100 kHz and bias voltage from −2 V to 0.5 V, while AC voltage was 30 mV.

In CZTSe solar cells the measured capacitance is attributed to the p-n$^+$ junction formed between CZTSe absorber layer (p-type) and CdS buffer layer (n-type). The Mott-Schottky model was used for approximating the doping density of the absorber layer:

$$\frac{1}{C^2} = \frac{2(V_{bi} - V)}{A^2 q \varepsilon N} \qquad \text{Equation 2-4}$$

Where C is the measured capacitance, A is the area, q is the electron charge, ε the dielectric permittivity of CZTSe, N is the doping concentration of CZTSe, V is the applied dc bias and V_{bi} is the built-in voltage. Thus by fitting a linear line to the plot of $1/C^2$ as a function of V (known as Mott-Schottky plot), one can derive the doping density (N).

Depletion region width (W) can be calculated as:

$$W = \sqrt{\frac{2\varepsilon(V_{bi} - V)}{qN}} \qquad \text{Equation 2-5}$$

Since W varies by the bias voltage, a plot of N versus W(V) gives the doping density profile across some portion of the absorber layer. In thin film solar cells N gives the shallow carrier density $|N_a - N_d|$ (N_a is the doping density of acceptors and N_d is the doping density of donors) plus the charge emitted from or captured at deep states that can respond in the ac period [77,78].

2.6.3 External quantum efficiency measurement

External quantum efficiency (EQE) measurement is a useful technique to quantify the spectral response of a solar cell and identify the origins of J_{sc} losses. The EQE is defined as the ratio of the number of carriers collected by the solar cell to the number of incident photons at each wavelength. EQE system measures the spectral response of the solar cell by focusing the light into a small spot of the solar cell and measuring the generated current as a function of wavelength. One can derive the J_{sc} from EQE measurement using this equation:

$$J_{sc} = q \int_{\lambda_1}^{\lambda_2} \varphi(\lambda)^{AM1.5} . EQE(\lambda) d\lambda \qquad \text{Equation 2-6}$$

Where q is the charge of electron and $\varphi(\lambda)^{AM1.5}$ is the photon flux. λ_1 and λ_2 are the lowest and largest wavelengths of the measurement range (for CZTSe solar cells a range of 300-1500 nm is appropriate). We measured the EQE of our solar cells at room temperature using a laboratory-built system with a grating monochromator-based dual-beam setup under chopped light from a Xe lamp.

2.6.4 Time-resolved photoluminescence (TR-PL) measurement

In time-resolved photoluminescence technique, a pulsed laser illuminates the sample and excites electrons from the valence band to the conduction band. These generated carriers recombine back to the equilibrium state and the resulting photoluminescence (PL) intensity is measured as a function of time. The radiative recombination rate depends linearly on the number of minority carriers. In p-type material $p_0 >> n_0$ and:

$$R_{rad} = B[p_0(\mathbf{r}) + p(\mathbf{r}, t)]n(\mathbf{r}, t) \qquad \text{Equation 2-7}$$

Where B is the radiative recombination constant, p_0 is the concentration of holes and p and n are the excess hole and electron concentrations. **r** and t represent space and time, respectively. In low injection conditions, $p << p_0$, and according to the Equation 2-7 the rate of radiative recombination is linearly proportional to the number of minority carriers. In high injection condition, $p >> p_0$, and PL signal is proportional to p^2 and even though the situation is more complicated but still the excess carrier concentration can be tracked by the decay of the PL signal. The PL decay tracks minority carrier recombination, even if it is mainly due to non-radiative processes such as Shockley-Read-Hall (SRH) or Auger recombination [79]. **Figure 2-6** shows a TR-PL measurement of a CZTSe solar cell. Usually, this PL decay signal consists of two different exponential decays. First, the signal decays at a fast rate which is interpreted as the separation of charges due to the built-in field of the device. Then the signal decays at a slower rate which is considered as the minority carrier lifetime in the bulk of the absorber layer due to the different radiative and non-radiative recombination channels [80].

In this work, low injection TR-PL measurements were acquired at room temperature by a Hamamatsu C12132. C12132 is a near infrared compact fluorescence lifetime spectrometer that contains a YAG LASER for excitation light, variable neutral density (ND) filter for adjusting excitation light level, iris (aperture) and ND filter for adjusting emission light level, filter for cutting excitation light, automatic monochromator and two types of PMT (photomultiplier tube) detectors (VIS and NIR). Using this system, an area of 3 mm diameter of samples was illuminated by a 532 nm laser with 15 kHz repetition rate, 1.3 ns pulse width, and 1.0 mW average power.

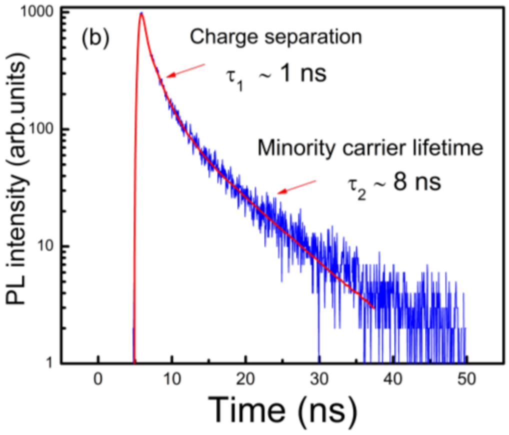

Figure 2-6 TR-PL measurement of a CZTSe solar cell.

2.6.5 Photoluminescence measurement

Photoluminescence (PL) measurements were performed with Hamamatsu C12132. The PL spectrum of kesterite solar cells is usually an asymmetric broadband spectra and the PL peak position is often at lower energies, as compared to the band gap of kesterite semiconductors. The observed broad PL peak with this redshift as compared to the band gap and its dependence on the excitation power and temperature indicate the existence of potential fluctuation and tail states in bands [81,82].

2.6.6 Transmission electron microscopy (TEM)

High angle annular dark field scanning transmission electron microscopy (HAADF-STEM) images and energy dispersive X-ray (EDX) maps were acquired using an FEI Osiris microscope and Titan^3 microscope equipped with a Super-X detector and operated at 200 kV. The specimens for TEM were prepared using the focused ion beam (FIB) technique, on a Be support. EDX maps were generated from the intensity of the Mo-K, Se-K, Cu-K, Cd-L, Zn-K, Sn-L, S-K, Ti-K, O-K, C-K lines.

2.6.7 X-Ray diffraction technique

X-ray diffraction (XRD) is a useful technique to characterize the crystal structure of materials and identify the phases present in the films. Identifying secondary phases ZnS(Se) and $Cu_2Sn(S(Se))_3$ with XRD is very difficult as they have very similar XRD pattern to CZTS(Se). A complementary technique such as Raman spectroscopy is required to distinguish these phases [6]. However it is possible to identify CZTSSe, Sn(S,Se), $Sn(S,Se)_2$ and $Cu_{2-x}(S,Se)$ using XRD. Using Scherrer’s equation, one can also estimate the crystallite size:

$$D = \frac{K\lambda}{B\cos(\theta)} \qquad \text{Equation 2-8}$$

Where D is the crystallite size, K is a dimensionless factor around 0.9, λ is the X-ray wavelength, B is the full width at half maximum (FWHM) and θ is the Bragg angle.

2.6.8 Glow discharge optical emission spectroscopy (GDOES)

In Glow discharge optical emission spectroscopy (GDOES), the sample is bombarded by the glow discharge Ar plasma source and an optical spectrometer is used as the real-time detection to determine the elemental depth profiles as a function of the thickness. The sputtering process is very fast and the sputtering rate is of the order of μm/min.

Here, compositional depth profiles of elements are recorded by GDOES using a Horiba Scientific GD-Profiler 2 operated in RF-mode at powers of 26 W and argon pressures of 5 mbar. The measurement spot has a diameter of 4 mm and a depth-resolution within the absorber of about 60 nm is achieved.

2.6.9 Raman spectroscopy

Raman spectroscopy relies on inelastic scattering where a laser beam interacts with molecular vibrations (phonons). This interaction leads to a shift of laser photon energy that is unique for different molecules and can be used for identification of the materials. The frequency difference between the scattered light and the incident light is called Raman shift that is usually in the unit of wavenumber (cm^{-1}). A Raman spectrum is a plot of the intensity of the scattered light as a function of Raman shift. Raman spectroscopy is very useful characterization technique for identifying CZTSSe and other secondary phases that may form during the fabrication process such as $Cu_2SnS(Se)_3$, SnS(Se)/$SnS(Se)_2$,ZnS(Se) [11]. Using Raman spectroscopy it is possible to estimate the amount of x=[S]/[Se]+[S] ratio in the CZTSSe compound. A_1 vibration mode of CZTSSe is related to the vibration of anions while the cations are fixed. This A_1 vibration mode is at ~ 338 cm^{-1} for pure sulfide CZTS and around 196 cm^{-1} for pure selenide CZTSe. For the intermediate values of x the Raman spectrum shows a bimodal behavior in which the A_1 peak of CZTSe shifts to higher values and the A_1 peak of CZTS shifts to lower values [83,84], as shown in **Figure 2-7** [84].

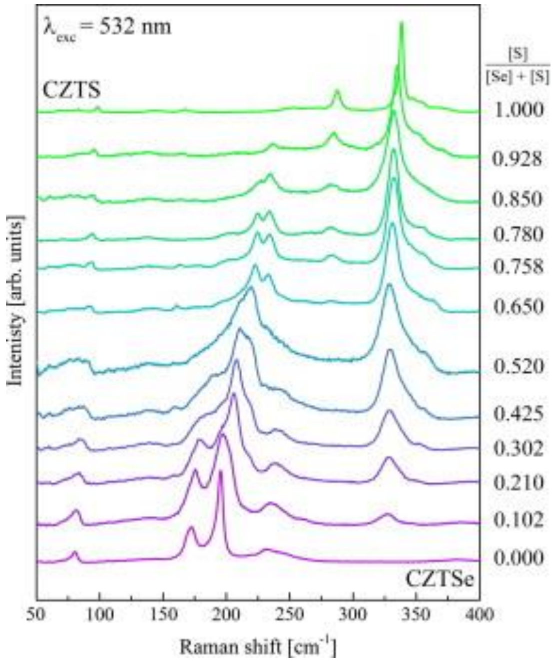

Figure 2-7 Raman spectra of CZTSSe thin films with different S/(S+Se) ratio measured with 532.0 nm excitation wavelength [84].

2.7 Reflection and transmission measurement

To estimate the band gap of the kesterite absorber layers, we prepared absorbers on glass substrates and the reflection and transmission spectra of these samples were measured using a Shimadzu UV3600 spectrophotometer equipped with an integrating sphere. The absorption coefficient, α, is given by:

$$\alpha = \frac{-1}{d}\ln\left[\frac{-(1-R)^2+\sqrt{(1-R)^4+4T^2R^2}}{2TR^2}\right] \qquad \text{Equation 2-9}$$

Where d is the thickness of the film, R is the reflectance, and T is the transmittance spectra. For a direct bandgap semiconductor such as kesterite, bandgap can be derived by this equation:

$$\alpha \propto \sqrt{h\upsilon - E_g} \qquad \text{Equation 2-10}$$

Where h is the Plank’s constant, υ is the frequency, and E_g is the bandgap energy. So one can obtain the band gap energy from a linear fit to $(\alpha.h\nu)^2$ plot versus photon energy hυ (known as Tauc’s plot) [6].

3 Optimizing the selenization condition of Zn/SnS$_2$/CuS precursors

Recent studies indicate an improvement by incorporation of both S and Se in kesterite compound so as to form $Cu_2ZnSn(S_x,Se_{1-x})_4$ alloy, known as CZTSSe [48,85]. The best efficiency recorded so far for kesterite solar cell (12.6 %) belongs to a $Cu_2ZnSn(S_x,Se_{1-x})_4$ (CZTSSe) having a $[S]/([S]+[Se])$ ratio of about 30% [50]. The variation of sulfur to selenium ratio in this compound changes the structural, electrical and optical properties of the film [21].

In this study, we investigate the effect of selenization conditions on the structural and morphological properties of CZTSSe thin films. CZTSSe thin film is prepared in a two-step process, first, the deposition of Zn/SnS$_2$/CuS precursors on the Mo-coated glass using the hybrid sputtering-evaporation technique and then annealing in a Se vapor environment. The selenization was performed using two different approaches including a tube furnace and a rapid thermal processing system. The annealing conditions were varied and their effects on the film properties were studied.

3.1 Experimental details

3.1.1 Selenization in a tube furnace and a rapid thermal processing system

$Cu_2ZnSn(S,Se)_4$ (CZTSSe) thin films were prepared by selenization of Zn/SnS$_2$/CuS precursors. Fabrication of Zn/SnS$_2$/CuS precursors has been already explained in section 2.2. The precursors were selenized using two different approaches- one using a conventional Tube Furnace (TF) and the other using a Rapid Thermal Processing system (RTP). In the first approach, precursors were selenized by placing them inside a graphite box within the TF, along with 140 mg of selenium pellets with purity of N5. The pressure inside the graphite box was kept constant during the annealing at 600 mbar using N_2 gas. The precursors were selenized at various temperatures including 350, 400, 450, 480 and 500 $^{\circ}$C for 5 min and then cooled down naturally, as shown in **Figure 3-1**. In the second approach, about 2 μm thick layer of Se was deposited over identical precursor stacks after which they were annealed in RTP furnace using N_2 + 5 % H_2 gas at a pressure of 1 atm. The heating rate and annealing time, in this case, were fixed at 1 °C/s and 2 min, respectively. The precursors were annealed at maximum annealing temperatures of 400, 450, 500 and 525 °C. Bearing in mind that in RTP the heating rate was higher and the time at maximum temperature was shorter than in the tube furnace, selenization at slightly lower temperatures has been chosen in the case of the tube furnace in order to decrease the loss of sulfur during the annealing. Still, a good overlap in the temperature ranges of both annealing processes has been ensured. The samples are named according to the type of selenization method and their maximum temperature. For example, sample selenized using TF at 500 °C was named as Se-TF-500 and that using RTP at 500 °C was named as Se-RTP-500.

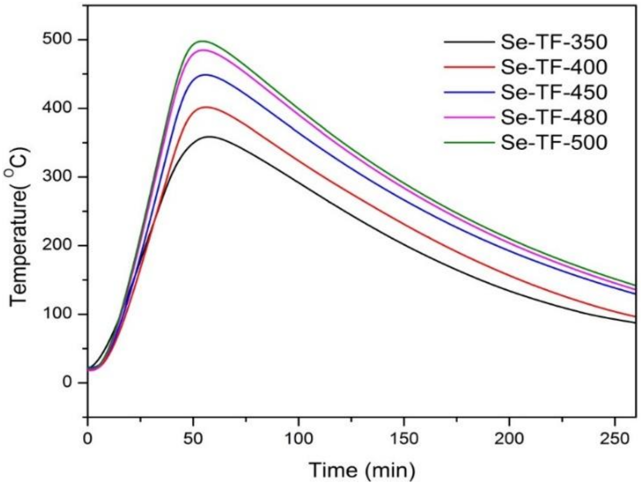

Figure 3-1 Temperature profile of selenization at different temperatures in TF.

3.2 Morphological and chemical characterizations

The morphology and the composition of the films were investigated by scanning electron microscopy (SEM) and energy dispersive spectrometry (EDS), using an SU-70 Hitachi combined with a Rontec EDS system, and the acceleration voltages of 4 kV and 25 kV were used for cross-sectional SEM and EDS, respectively. The cross-sectional SEM images of CZTSSe films selenized using the tube furnace are shown in **Figure 3-2 (a)** to **(d)**. The multilayer structure of Se-TF-350 is related to the initial precursor stack, indicating that a selenization temperature of 350 °C is not enough for the full conversion of the precursors to CZTSSe. It could be observed that the grain size increased as the selenization temperature is increased. At 500 °C the grain size is about 1 µm and the film morphology has improved compared to that at lower temperatures. **Figure 3-2 (e)** to **(f)** corresponds to the cross-sectional SEM images of the samples selenized in RTP furnace at different temperatures. Similar to that observed in SEM images of the TF annealed samples, in the case of RTP annealed samples also, a critical annealing temperature (450 °C) is observed, below which the precursor stack does not inter-diffuse completely to form a compact film of CZTSSe.

Figure 3-4 (a) and (b) show the top view SEM images of the sample selenized at 400 °C in TF at different magnifications. **Figure 3-3** (a) and (b) show the top view SEM images of the samples selenized at 400 and 450 °C in RTP, respectively. The surface of the samples selenized at 400 °C in TF and RTP consist of crystal-like formations with well-defined facets. These structures are copper selenide phases and were confirmed by Raman and XRD measurements which will be presented in the next section. By increasing the temperature to 450 °C, these well-defined crystalline structures become globular like formations.

The composition of the samples was measured by EDS and the results are given in **Table 3-1.** The EDS measurements revealed that the TF and RTP annealed samples were copper and zinc rich. This is evident from the presence of copper selenide crystals over the sample surface.

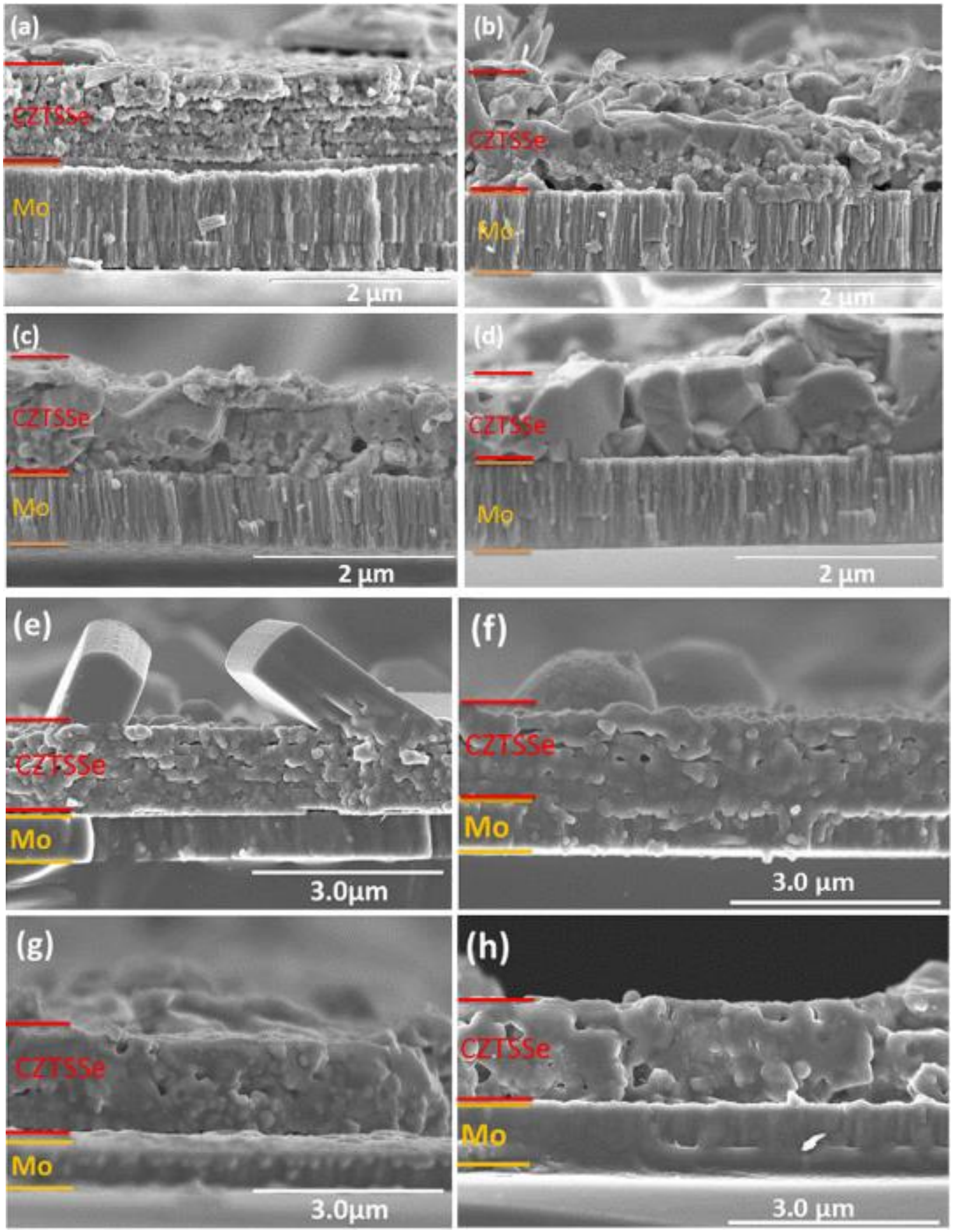

Figure 3-2 Cross-sectional SEM images of samples selenized in a tube furnace (TF) and a rapid thermal processor (RTP) at various temperatures: (a) Se-TF-350, (b) Se-TF-450, (c) Se-TF-480, (d) Se-TF-500, (e) Se-RTP-400, (f) Se- RTP-450, (g) Se- RTP-500 and (h) Se-RTP-525.

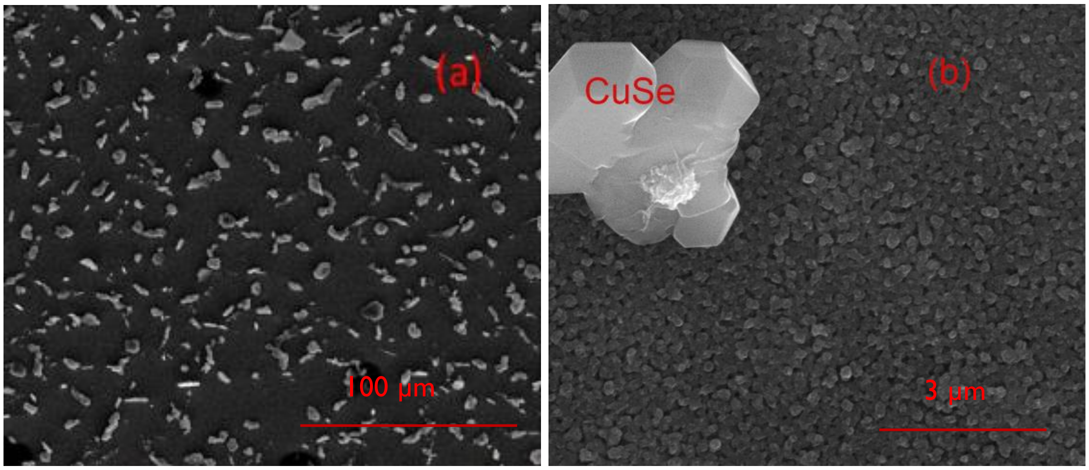

Figure 3-4 (a) and (b) Top view SEM images of Se-TF-400.

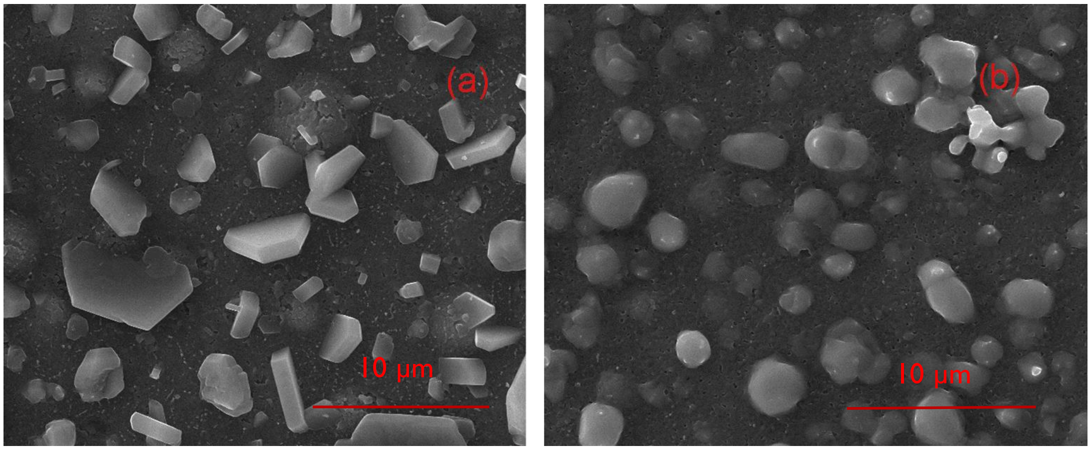

Figure 3-3 Top view SEM images of (a) Se-RTP-400 and (b) Se-RTP-450.

Table 3-1 Metal composition of the samples at various temperatures.

Sample	[Cu]/[Zn]	[Cu]/[Sn]	[Zn]/[Sn]	[Cu]/([Zn]+[Sn])
Se-TF-350	2.66	2.31	0.87	1.24
Se-TF-400	2.03	1.9	0.93	0.98
Se-TF-450	1.34	2.02	1.51	0.81
Se-TF-480	2.04	3.5	1.71	1.29
Se-TF-500	2.27	3.23	1.42	1.33
Se-RTP-400	1.95	3.56	1.82	1.26
Se-RTP-450	1.95	2.99	1.53	1.18
Se-RTP-500	1.76	2.77	1.57	1.08
Se-RTP-525	1.77	2.72	1.53	1.07

3.3 Structural and optical characterization

X-ray diffraction patterns were acquired using a XPert MPD Philips diffractometer in the Bragg–Brentano configuration (θ–2θ), using the Cu-Kα line (λ = 1.5406 Å), with the generator settings, 40 mA, and 45 kV. **Figure 3-5 (a)** shows XRD pattern of the TF annealed films under different selenization temperatures. The films annealed at 450 °C and above, show strong peaks corresponding to (112), (220), (204), (312) and (116) planes of tetragonal CZTSe, according to the International Center for Diffraction Data (ICDD), (Reference code: 04-010-6295). These results suggest that at temperatures above 450 °C all the sulfur contained in the precursor is replaced by the selenium supplied by the atmosphere during the annealing. For the films annealed at temperatures below 450 °C, there is a shift to higher diffraction angles. Considering the amount of peak shift with respect to that of pure CZTSe (27.16^o for (112) peak), the $[S]/([S]+[Se])$ ratio estimated using the empirical relation developed by Salome et al. [12], was 10 % and 78 %, respectively for samples Se-TF-400 and Se-TF-350. The existence of CuSe

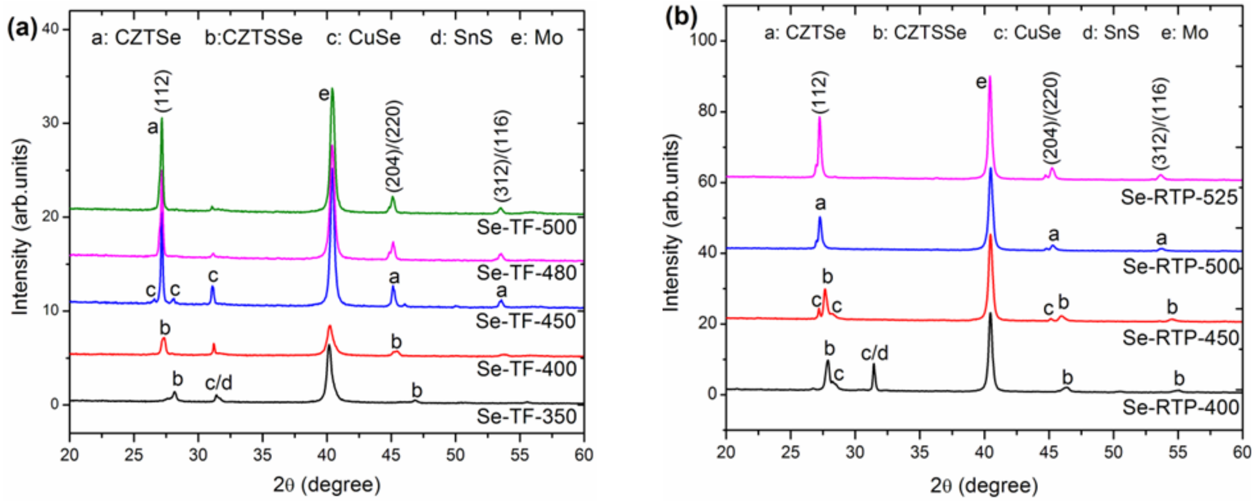

Figure 3-5 XRD patterns of samples selenized (a) using a tube furnace (TF), and (b) a rapid thermal processor (RTP), at various temperatures.

(Ref code: 01-086-1239 and 00-034-0171) is also indicated by XRD. XRD patterns of the RTP annealed samples are given in **Figure 3-5 (b).** In case of RTP annealed samples also, estimation of Se incorporation was done by identifying the amount of shift in diffraction peak (112) in the XRD pattern. For the Se-RTP-400, this peak is at 27.87^{o} which is at a considerably higher (lower) position than that of pure CZTSe (CZTS) ($2\theta=27.16^{o}$; ICDD card no. 04-010-6295 for CZTSe and $2\theta=28.44^{o}$; ICDD card no.01-080-8225 for CZTS). This is clearly an indication of the formation of CZTSSe. With the increase in selenization temperature, the peak slowly shifts to lower values suggesting that more and more Se is being incorporated. The estimated ratio of $[\mathrm{S}]/([\mathrm{S}]+[\mathrm{Se}])$ is given in **Table 3-2**. In addition to the main peaks, peaks corresponding to the secondary phases are also observed in the diffraction pattern. For Se-RTP-400 a secondary peak could be seen at a diffraction angle of 31.45^{o}. This could be due to either CuSe ($2\theta=31.11^{o}$; ICDD card no.01-086-1239) or due to SnS ($2\theta=31.52^{o}$; ICDD card no. 04-004-3833); or may be due to both. The presence of CuSe is evident from the cross-sectional SEM images whereas that of SnS may be justified from the fact that the layers of precursors are not completely inter-diffused at this temperature and that SnS_2 might have decomposed to SnS. The variation of (112) peak position and crystallite size with annealing temperature for TF and RTP annealed samples is given in **Table 3-2**. The crystallite size was evaluated from the XRD data using the Scherrer formula. The $[\mathrm{S}]/([\mathrm{S}]+[\mathrm{Se}])$ ratio estimated from the XRD analysis indicate that in both methods increasing the temperature will increase the incorporation of selenium and the loss of sulfur. The results also show that at the same temperatures, there is a higher amount of sulfur in RTP annealed samples compared to the TF annealed ones, due to the shorter annealing time in RTP that decreases the loss of sulfur during the annealing. The shorter annealing time is possible and chosen in RTP to ensure higher sulfur contents at higher temperatures than those observed in the tube furnace in which short annealing times are difficult to achieve due to the thermal inertia of the system.

Table 3-2 (112) peak position, Full Width at Half Maximum (FWHM) and crystallite size of samples selenized in a tube furnace (TF) and a rapid thermal processor (RTP) at various temperatures.

Sample	(112) peak position (degree)	FWHM (degree)	Crystallite size (nm)	[S]/[S]+[Se] (%)
Se-TF-350	28.16	0.38	21.5	78
Se-TF-400	27.30	0.30	27.2	10
Se-TF-450	27.17	0.15	54.5	< 1
Se-TF-480	27.17	0.14	58.4	< 1
Se-TF-500	27.17	0.14	58.4	< 1
Se-RTP-400	27.87	0.28	29.6	55
Se-RTP-450	27.68	0.25	33.1	41
Se-RTP-500	27.28	0.20	41.3	9
Se-RTP-525	27.25	0.18	45.9	7

Figure 3-6 (a) shows the Raman spectra of TF annealed samples. Raman spectra of the samples annealed at 450 °C and higher temperatures have characteristic peaks at 173, 196, 235 cm^{-1} indicating the formation of pure CZTSe [10]. The samples annealed at lower temperatures shows a bimodal behavior in the Raman spectrum with peaks corresponding to A$_1$ vibrational modes of CZTSe and CZTS. However, the A$_1$ mode vibrations of CZTSe are shifted to higher wavenumbers whereas that of CZTS is shifted to lower wavenumbers. This clearly is an indication of the formation of a CZTSSe phase in which S atoms are partially replaced by Se. The intense peak in case of Se-TF-350 is at 333 cm^{-1} indicating the presence of CZTSSe, the other peak at 235 cm^{-1} may be related to CZTSe. Se-TF-400 has a small peak at 328 cm^{-1} that indicates the presence of CZTSSe, it also has an intense peak at 196 cm^{-1} corresponding to CZTSe and a shoulder at 202 cm^{-1} that may correspond to a CZTSSe phase. The peaks in the range 260-267 cm^{-1} in the spectra belong to CuSe phase. Raman spectra of RTP annealed films at 400 and 450 °C, as shown in **Figure 3-6 (a),** consist of two broad peaks centered at 215 and 330.5 cm^{-1}. However, it may be noted that the peak at 215 cm^{-1} is actually composed of two peaks one centered around 211cm^{-1} and the other at around 220.5 cm^{-1}. The peak at 211 cm^{-1} appears only as a shoulder to the peak at 220.5 cm^{-1} in Se-RTP-400. On increasing the annealing temperature to 450 °C, the intensity of this peak increases, indicating its association with CZTSSe, since more sulfur is being replaced by selenium with an increase in temperature. The peak at 330.5 cm^{-1} is also attributed to CZTSSe. At higher temperatures, this peak is almost completely suppressed and the spectra consist of only three peaks at 174, 197 and 234.5 cm^{-1} characteristic of CZTSe.

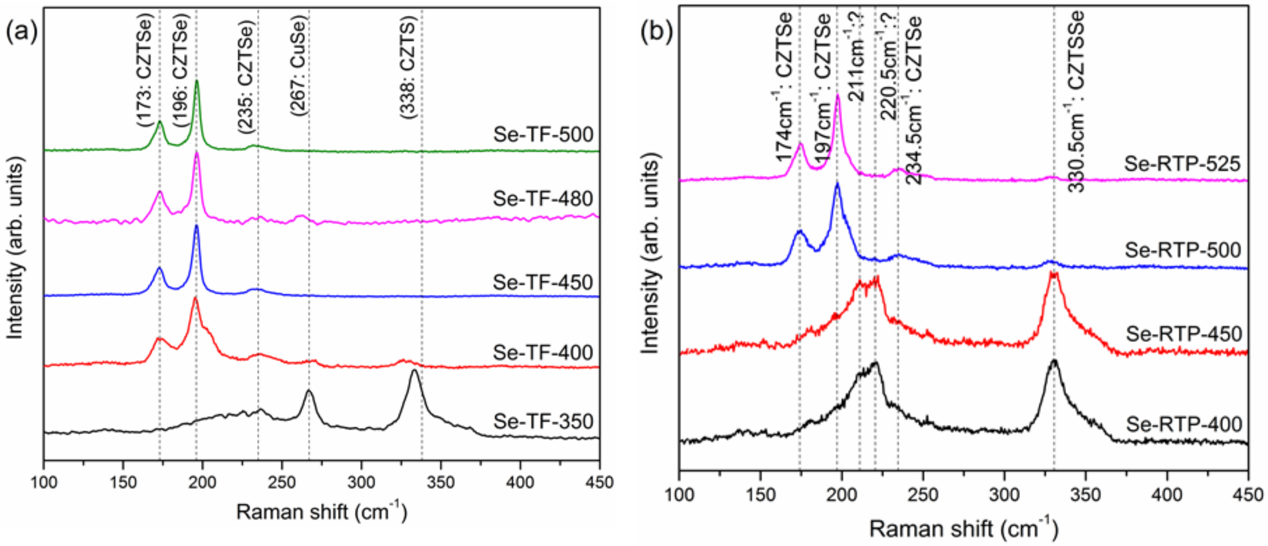

Figure 3-6 Raman spectra of samples selenized (a) using a tube furnace (TF), and (b) a rapid thermal processor (RTP) at various temperatures.

The reflection and transmission spectra of the samples selenized in TF were measured for samples prepared on SLG substrates using a Shimadzu UV3600 spectrophotometer equipped with an integrating sphere. The absorption coefficient was calculated, according to the procedure that was explained in chapter 2. As shown in **Figure 3-7 (a)** and **(b)**, the absorption coefficient of the samples selenized at different temperatures are above 10^4 cm^{-1} in the visible range and the bandgaps are below 0.98 eV, very close to the bandgap of pure CZTSe (1 eV). Bandgap measurements are consistent with other characterization techniques that indicate the formation of pure selenide compound using TF furnace.

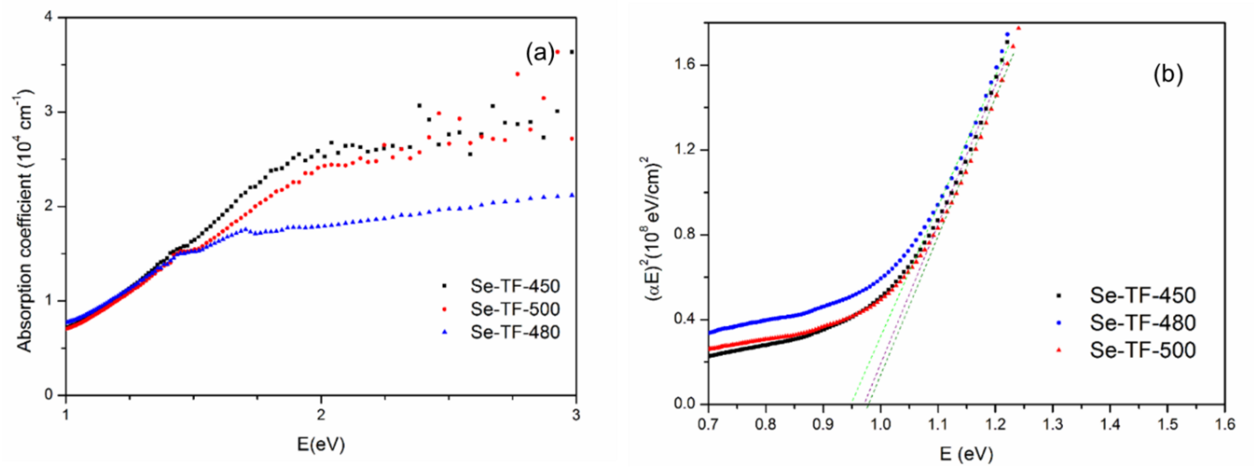

Figure 3-7 (a) Absorption coefficient, α of samples deposited on glass and selenized in a tube furnace as a function of energy (E), (b) $(\alpha E)^2$ as a function of energy.

With a large amount of CuSe secondary phases, we didn't consider to make solar cells from the absorber layers prepared by selenization of binary sulfide precursors. This large amount of CuSe can short circuit the solar cells as they have a small band gap. Thus in order to make solar cells, further optimization of the composition was necessary to reduce the formation of CuSe. Unfortunately, we couldn't continue this study due to the unavailability of the sulfide targets. Sulfide targets were more expensive than the metallic targets and they had a short lifespan, so we decided to abandon using the sulfide targets in our lab. The next studies of this thesis were performed in the imec-PV lab. The PV group in imec used a similar two-step vacuum based techniques to prepare kesterite solar cells. CZTSe films were prepared by selenization of e-beam evaporated metallic precursors using 10 % H_2Se gas in N_2 environment. The details of the fabrication and characterization techniques were explained in chapter 2 and in the following chapters the different approaches for improving the CZTSe absorber layer and CZTSe based solar cell will be explained.

3.4 Conclusions

The effect of selenization temperature on the structural and morphological properties of CZTSSe thin films obtained through the selenization of multi-stacked precursors using a conventional tube furnace (TF) and a rapid thermal processing system (RTP) was studied. From the cross-sectional SEM analysis, it was observed that at temperatures lower than 450 °C, irrespective of the selenization method, the precursor stack does not interdiffuse completely to form a compact layer of CZTSSe. The film formed at these temperatures consists of a sulfur-rich CZTSSe phase along with secondary phases of CuSe and SnS. At 450 °C, sulfur in the precursors is almost completely replaced by selenium in the conventional tube furnace whereas in RTP a much higher percentage of sulfur is observed due to the shorter annealing time that decreases the loss of sulfur. Above 450 °C, RTP selenization also resulted in Se-rich films. However, the results suggest that RTP selenization method could have an advantage over the conventional tube furnace in obtaining CZTSSe films at much shorter annealing time. This study also indicates that it’s not easy to control the amount of sulfur in CZTSSe only by incorporating sulfur in the precursors. To prepare high quality CZTSSe films an annealing at sulfur and selenium vapor is required.

4 Effect of absorber thickness on the performance of CZTSe solar cells

Absorber layer thickness is one of the most important physical factors affecting the kesterite solar cells performance. However, despite many studies about the influence of other parameters such as composition, morphology, etc., on kesterite solar cells there aren't many studies about the impact of kesterite absorber layer thickness. Ren et.al studied the effect of variation of absorber layer thickness for pure sulfide Cu_2ZnSnS_4 (CZTS) kesterite solar cells [86]. They prepared absorber layers by a two-step process including deposition of Cu/Zn/Sn/S precursors using an H_2S gas reactive sputtering system, followed by sulfurization of the precursors in a tube furnace at 560 ºC for 10 min in Ar atmosphere. Solar cells with different absorber layer thickness in the range of 500-2000 nm were prepared by changing the sputtering time of the precursors between 20–80 min. The solar cells with different thickness had efficiencies in the range of 3.0 % to 6.8 % and the best efficiency belongs to a solar cell in which the thickness of the absorber layer was 1500 nm. Their study indicated that J_{SC}, V_{OC} and consequently the efficiency of (CZTS) solar cells improve strongly by increasing the thickness while the improvement saturated at 1500 nm. In this study, we fabricated pure selenide $Cu_2ZnSnSe_4$ (CZTSe) films by selenization of e-beam evaporated Sn/Zn/Cu precursors. We changed the thickness of absorber layers by changing the thickness of Sn/Zn/Cu precursors. The effect of variation of the thickness of the absorber layers on the physical, optical and electrical properties of the solar cells is investigated. To the best of our knowledge, this is the first study that investigates the effect of CZTSe absorber layer thickness on the optoelectronic properties of selenide kesterite solar cells.

4.1 Fabrication of solar cells with different absorber layer thicknesses

In order to fabricate absorber layers with different thicknesses, we changed the thickness of Sn/Zn/Cu precursors systematically. Metallic layers with different thickness (See Table.1) were deposited using an e-beam evaporation system, as explained in section 2.3. The metallic ratios of precursors were kept constant in order to control the composition. In the second step, the Sn/Zn/Cu stacks were selenized by 10 % H_2Se gas diluted in N_2 for 15 min at 460 °C in a rapid thermal processing system with 1 °C/s heating rate. Absorber layers with thicknesses of ~ 300, 700, 1000, 1200 and 1700 nm were fabricated. The thickness of the absorber layers was measured by cross-sectional SEM images. Solar cell devices with different absorber layer thicknesses were prepared and in the following, the best results that have been achieved for these solar cells are discussed.

4.2 Morphological and chemical characterization

Top-view SEM images of CZTSe absorber layers with thicknesses of 300, 700, 1200 and 1700 nm are shown in **Figure 4-1(a)** to **(d)**, respectively. Cross-sectional SEM images of devices with 700, 1000, 1200 and 1700 nm thickness are shown in **Figure 4-2 (a)** to **(d)**, respectively. SEM images reveal by increasing the thickness, the morphology of the absorbers improves, the grain size increases and less voids and pinholes can be observed in the films.

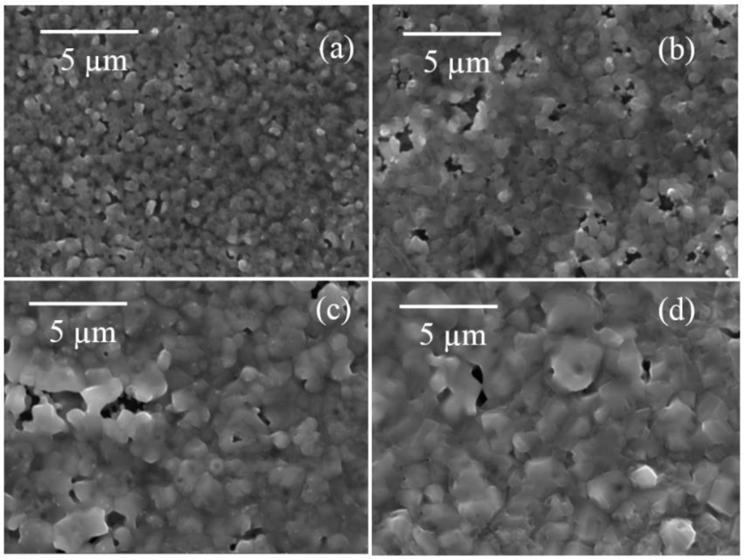

Figure 4-1 Top view SEM images of absorber layers: (a) to (d) absorbers with 300, 700, 1200, 1700 nm thickness.

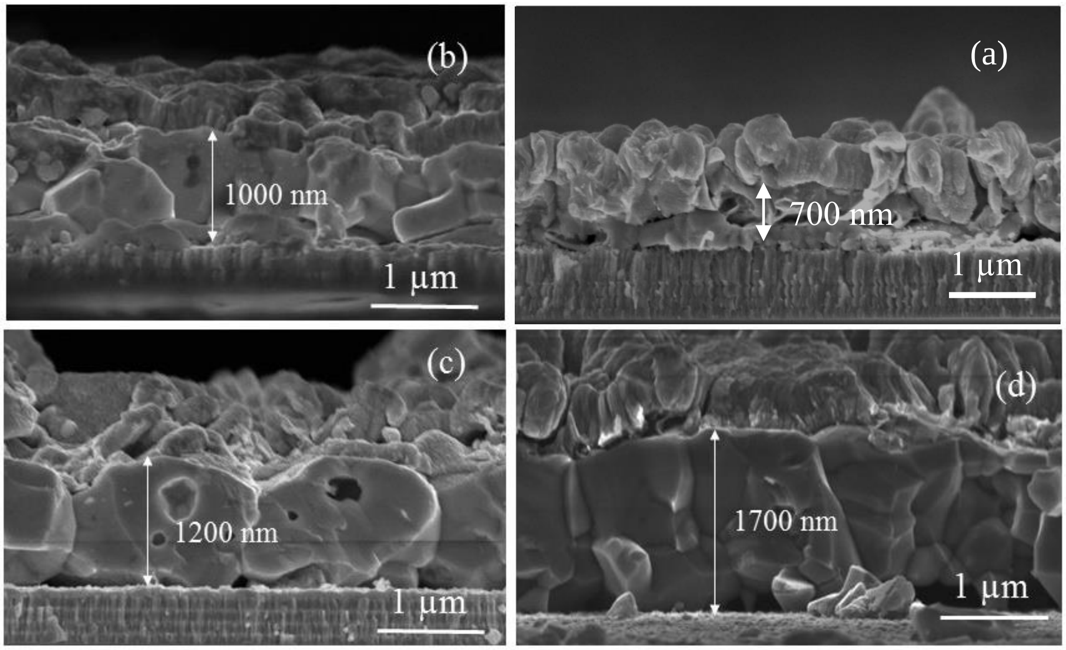

Figure 4-2 Cross sectional SEM images of absorber layers; (a) to (d) absorbers with 700, 1000, 1200, 1700 nm thickness.

The composition of the samples was measured by EDS and the results are given in **Table 4-1**. Although the metallic ratios were kept constant in order to control the composition and X-ray fluorescence measurement of initial precursors confirmed the expected thicknesses for all samples, the Cu/Sn decreases constantly by decreasing the thickness. The reason of Sn excess composition of the thinner samples is not quite clear, however, the faster interdiffusion of the three metal layers and consequently reduced the formation of volatile $SnSe_2$ might be the reason for the larger amount of Sn in the thinner samples as compared to the thicker samples. Moreover, the thinnest absorber layer has a very Zn-poor composition despite the same metallic ratios of the Sn(54)/Zn(26)/Cu(30) precursor compared to the other precursors. It might be possible that Zn loss is more severe in this sample that has only a thin layer of Cu (30 nm) covering the Zn layer.

Table 4-1 Metal composition of CZTSe absorbers with different thickness.

Thickness (nm) Sn/Zn/Cu	**Thickness (nm) After Selenization**	**Cu/Zn**	**Cu/Sn**	**Zn/Sn**	**Cu/(Zn+Sn)**
54/26/30	300	1.97	1.24	0.63	0.76
107/53/60	700	1.34	1.38	1.03	0.68
215/105/120	1000	1.51	1.59	1.06	0.77
260/126/145	1200	1.49	1.59	1.07	0.77
310/150/160	1700	1.71	1.74	1.04	0.86

4.3 Structural characterizations

The XRD pattern of absorber layers with different thicknesses, (See **Figure 4-3**) confirms the formation of CZTSe. Peaks corresponding to (112), (220), (204), (312) and (116) planes of CZTSe are indicated according to International Center for diffraction Data, (ICDD Reference code: 04-010-6295). The intensity of the peaks increases by increasing the thickness due to the improvement of the crystalline quality of the samples. Peaks corresponding to CuSe can be seen in all samples. Thin samples with 200 nm and 500 nm have peaks corresponding to SnSe as expected for Sn-rich composition in these samples, as well as broad peaks at 31.1 ^{o} and 56.0 ^{o} corresponding to $MoSe_2$. ($MoSe_2$: **04-004-8782**).

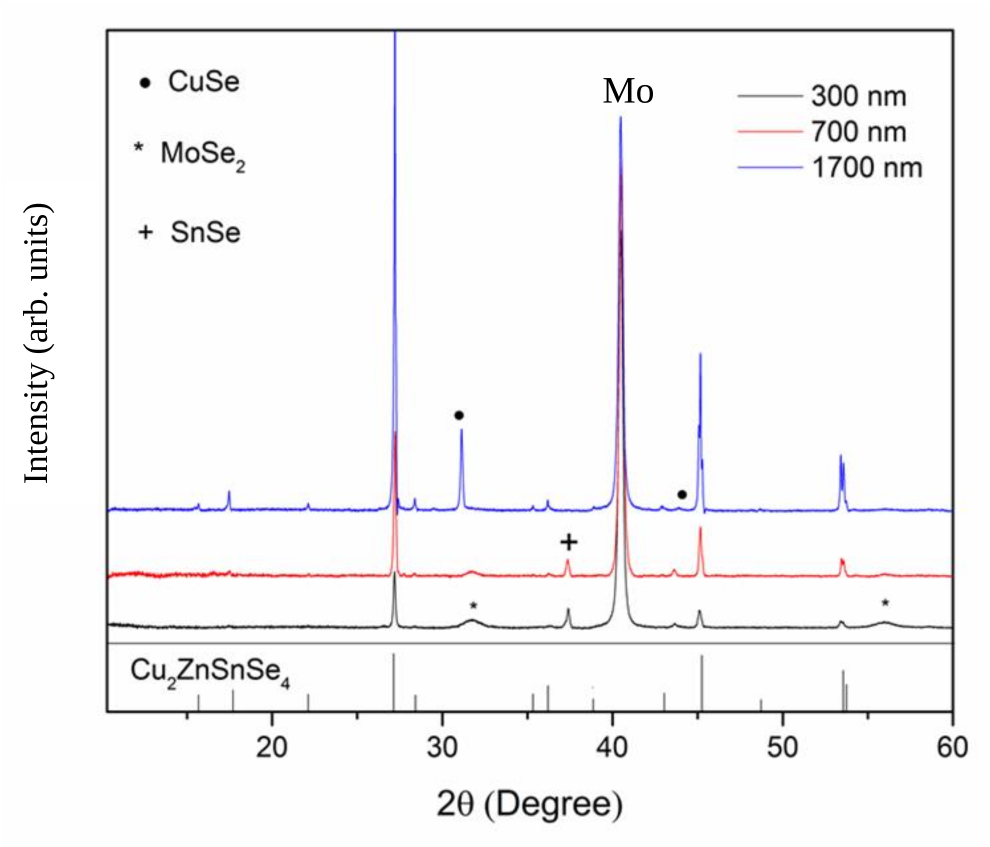

Figure 4-3 XRD pattern of the absorber layers with different thickness of 300, 700 and 1700 nm.

4.4 Optical characterizations

Figure 4-4 shows the room temperature photoluminescence (PL) of the solar cells. The position of the PL peak of the solar cells with different thickness is summarized in Table.2. By decreasing the thickness, the PL spectra become broader and the PL peak position shifts slightly towards lower energies. The PL peak of CZTSe is generally attributed to a donor to acceptor recombination in the presence of a large amount of band tail states and potential fluctuations [82]. The red shift of the PL spectra by decreasing the thickness might be due to a larger amount of band tail states in the thinner samples. The reason of larger tail states in thinner samples is

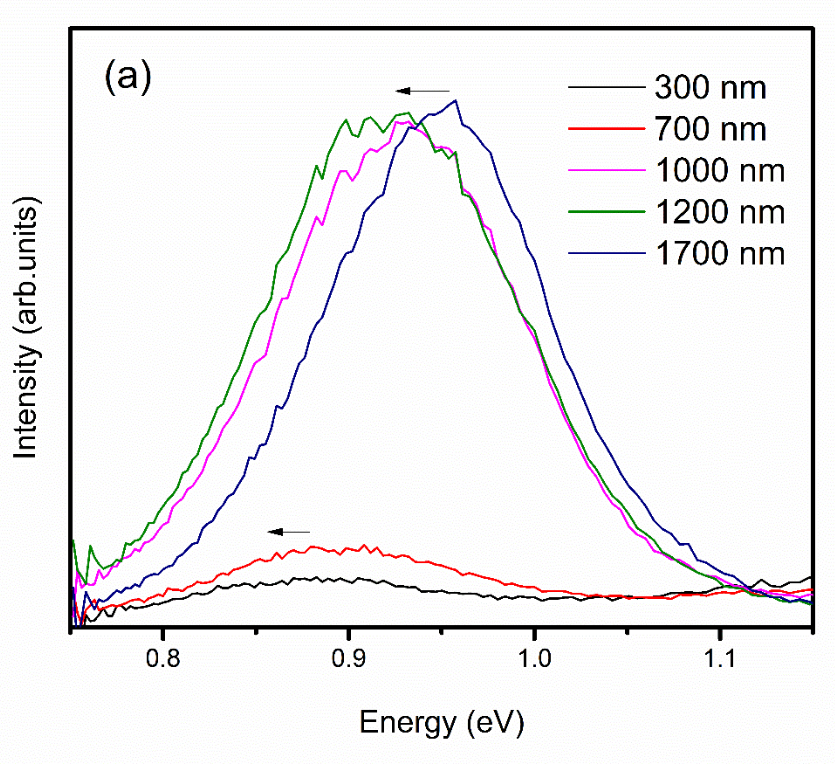

Figure 4-4 Room temperature Photoluminescence spectra of solar cells with different thicknesses.

not completely clear but it can be due to several reasons such as the Sn-rich composition which can lead to the formation of Sn_{Cu} and Sn_{Zn} deep defects or the formation of secondary phases with different band gaps that produce tail states and fluctuation in bands.

Figure 4-5 shows the minority carrier lifetime, τ_2 of solar cells with different thickness. The minority carrier lifetime is derived using a two exponential fit to the photoluminescence decay curve. The slower decay time usually is considered as the minority carrier lifetime [80]. The minority carrier lifetime of the samples increases by increasing the thickness and it reaches 8.4 ns when the thickness of absorber layer is 1700 nm. The enhancement of the minority carrier lifetime by increasing the thickness is correlated to the lower doping concentration that will be discussed in the next session (4.5 Electrical characterization). Also, the Sn-rich composition of ultra-thin samples may lead to electron trapping defects such as Sn_{Cu}, Sn_{Zn} or other compensated defect clusters that increase the recombination and degrade the minority carrier lifetime significantly.

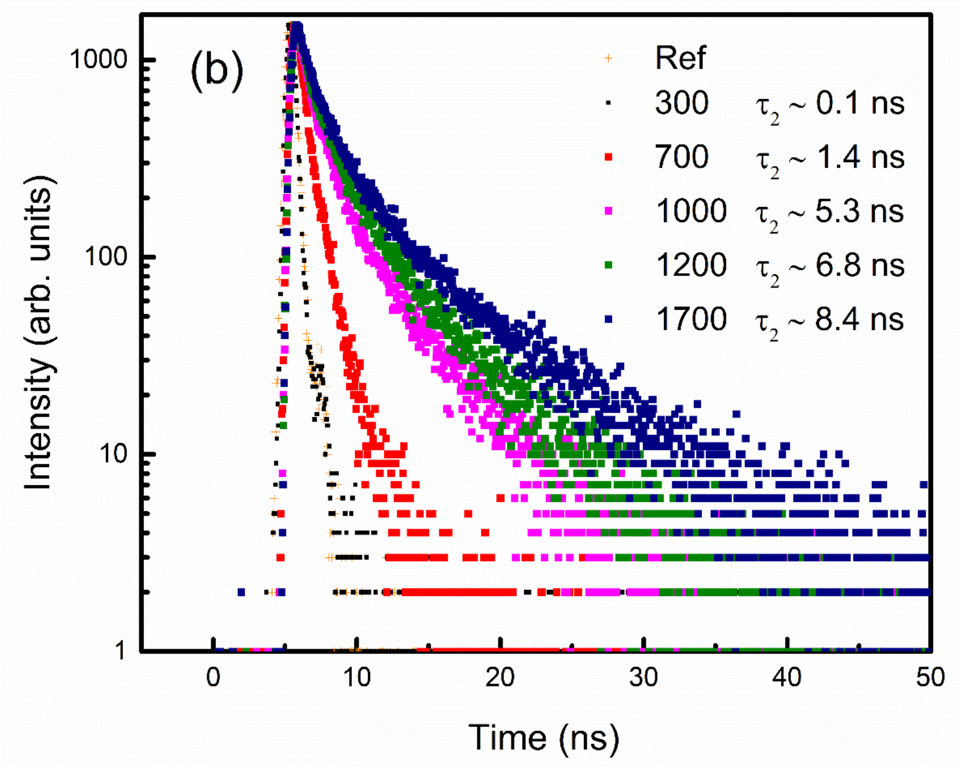

Figure 4-5 TR-PL spectra of solar cells with different thickness. τ_2 is the minority carrier lifetime.

4.5 Electrical characterizations

Figure 4-6 shows the doping density profile of the absorbers with different thicknesses obtained by Mott–Schottky plot from the C-V measurement at a frequency of 40 kHz. By increasing the thickness, the doping density (N_a) decreases substantially, thus the space charged region (SCR) becomes wider. The reason for this large variation of doping density with the absorber layer thickness is not quite clear but might also be related to the variation of the composition mainly the Cu to Sn ratio in the absorbers with different thickness. By increasing the thickness, the Cu to Sn ratio increases while the doping density decreases significantly (See **Figure 4-8 (a)**). Another possibility of variation of doping density with thickness might be the influence of the rear interface. By increasing the thickness, the edge of the space charge region where we measure the carrier concentration is less affected by the imperfections at the rear contact.

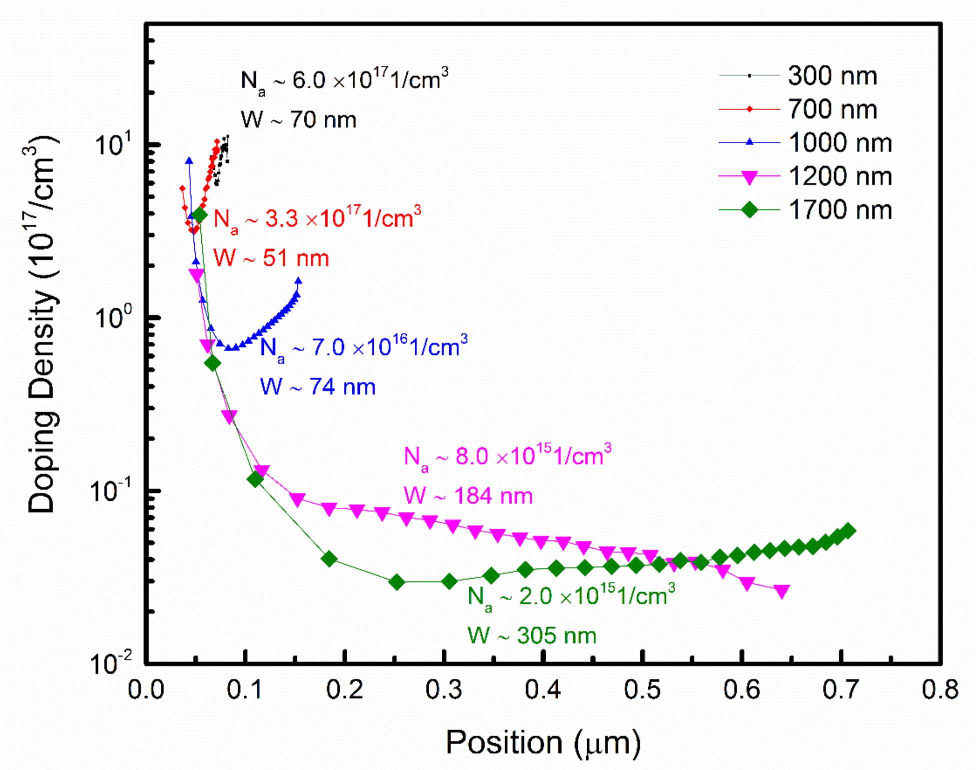

Figure 4-6 Doping density profile (N_a) of solar cells with different thicknesses derived from Mott–Schottky plot, W is the space charged region width.

Figure 4-7 shows the illuminated/dark J-V curve (solid/dashed lines) of the champion solar cells of each thickness. The corresponding cell parameters are derived from the procedure explained by Hegedus and Shafarman [77] and are summarized in **Table 4-2**. Shunt resistance, R_{sh} is very low when the absorber thickness is ≤ 1000 nm and it improves significantly to 512 Ω.cm^2 for the thickest sample since the CZTSe film becomes more compact. J_{SC} is very low when the thickness of the device is ≤1000 nm because of the incomplete collection of the solar spectrum. Further improvement of J_{SC} of samples thicker than 1000 nm can be attributed to a wider space charged region that facilitates the collection of carriers. **Figure 4-8 (c)** shows that by increasing the thickness from 1000 nm to 1700 nm the depletion region width increases from 70 nm to 300 nm and J_{SC} improves up to 36.4 mA/cm^2. The significant improvement of V_{OC} by increasing the thickness indicates the reduction of recombination currents and it is consistent with the enhancement of minority carrier lifetime (See **Figure 4-8(b)**). It can be observed that the first three samples have very low FF below 47 % while devices with 1200 nm and 1700 nm have a better behaved illuminated J-V curve in the reverse region and the FF improves to 54 %.

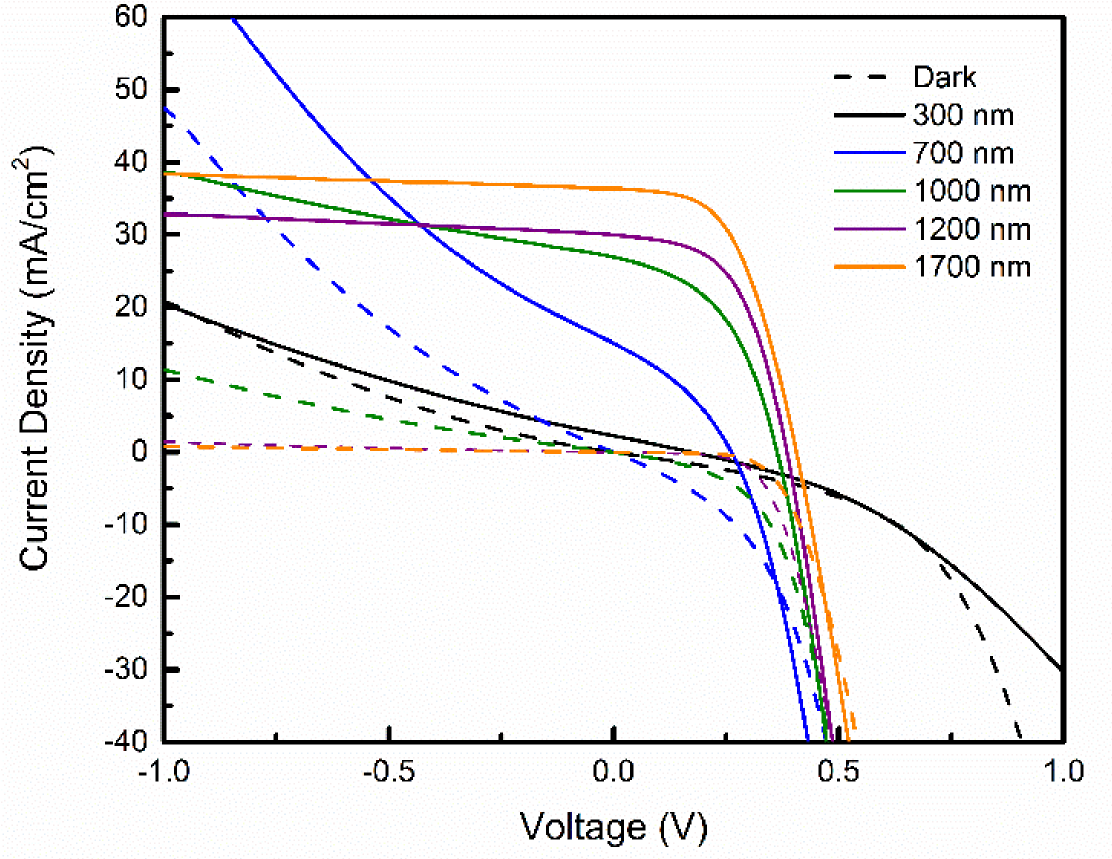

Figure 4-7 Current-voltage measurement of solar cells with different absorber thickness under dark (dashed line) and 1 sun illumination (solid line).

Table 4-2 Electrical and optical parameters of solar cells with different absorber thicknesses ;short circuit current (J_{sc}), open circuit voltage (V_{OC}), fill factor (FF), efficiency (η), shunt resistance (Rsh) and series resistance (Rs) are derived from illuminated J-V measurement. PL peak position and lifetime (**τ**) are derived from TR-PL measurement.

Thickness (nm)	**J_{SC}(mA/cm^2)**	**J_{SC} (EQE) (mA/cm^2)**	**V_{OC} (mV)**	**FF (%)**	**η (%)**	**R_{sh} (Ω.cm^2)**	**R_s (Ω.cm^2)**	**PL peak (eV)**	**τ (ns)**
300	2.3	_	175.0	25	0.1	68	2.07	0.89	0.1
700	15.2	_	262.0	34	1.4	31	1.16	0.89	1.4
1000	26.9	26.60	363.0	47	4.6	98	1	0.93	5.3
1200	30	34.92	385.0	54	6.2	277	1.26	0.91	6.8
1700	36.4	39.50	406.0	53	7.8	512	1.35	0.95	8.4

The EQE measurement is shown in **Figure 4-8 (d)** indicates that by increasing the thickness photocurrent collection improves especially at long wavelength region that can be mainly due to the longer minority carrier lifetime and wider space charged region.

In **Table 4-3** the values of ideality factor (A) and dark saturation current (J_0) of the solar cells with different thickness derived from dark (D) and illuminated (I) J-V measurement are shown. Also, doping density and the space charged region width derived from C-V measurements are summarized in **Table 4-3**. By decreasing the thickness, the ideality factor increases. Large ideality factor above 2 indicates peculiar recombination mechanisms such as tunneling enhanced recombination, donor-acceptor pair recombination or fluctuation of activation energy of the main recombination path [53]. By increasing the thickness from 700 nm to 1700 nm, the dark saturation current is decreasing. The decrease of the dark saturation current by increasing the thickness indicates the decrease of recombination and it is consistence with increasing of V_{OC} and lifetime.

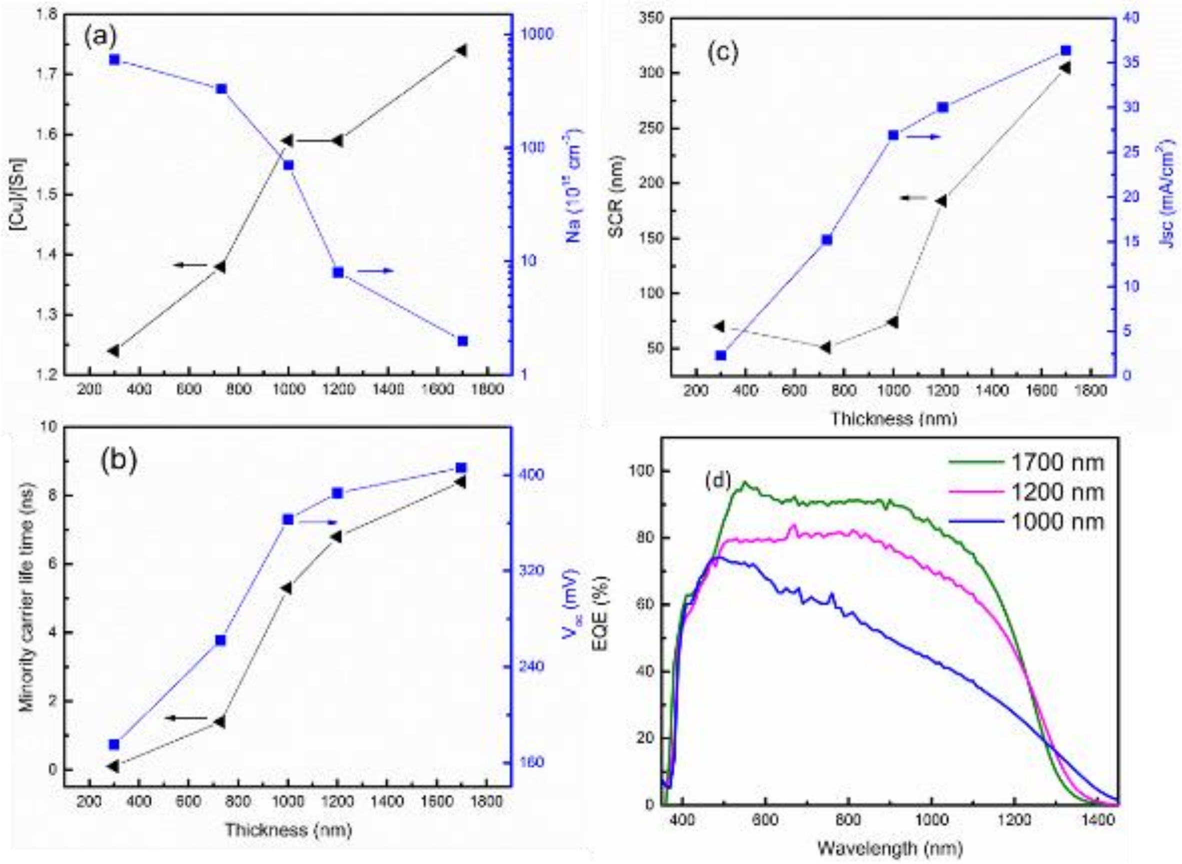

Figure 4-8 (a) Cu to Sn ratio and hole concentration (N_a), **(b)** Minority carrier lifetime and V_{OC}, **(c)** SCR and J_{sc} at various thickness. **(d)** External quantum efficiency (EQE) of solar cells with different absorber layer thickness.

Table 4-3 Ideality factor (A), the dark saturation current (J_0) are derived from dark (D) and Illuminated (I) J-V measurement, doping density and depletion with are derived from C-V measurement.

Thickness (nm)	**A (D)**	**A (I)**	**J_0 (D) ($\times 10^{-5}$)**	**J_0 (I) ($\times 10^{-5}$)**	**Doping Density ($\times 10^{15}$ cm^{-3})**	**W (nm)**
300	2.35	4.26	0.15	3.20	600	70
700	2.13	2.35	2.00	8.00	330	51
1000	2.9	2.90	0.70	15.00	70	74
1200	1.41	2.24	0.05	3.00	8	284
1700	1.28	1.90	0.01	1.40	2	305

4.6 Conclusion

In conclusion, increasing the thickness improved the quality of CZTSe absorber layers prepared by selenization of e-beam evaporated Sn/Zn/Cu stacks. Thicker metal starting layers led to a larger Cu to Sn ratio in the final absorber, possibly because the thinner starting layers show faster interdiffusion of the metals and suppressed $SnSe_2$ evaporation. The enhanced physical quality of the absorber layers leads to higher performance of solar cells, especially due to a, longer minority carrier lifetime and accordingly higher V_{OC}. In addition, it was found that the doping of the absorber layer decreased with increasing sample thickness and the wider space charge region of the thicker devices lead to the better collection of photogenerated carriers and higher J_{SC}.

5 Optimization of precursors and selenization step

In this chapter, we will discuss several parameters of the fabrication process that can affect the performance of the baseline CZTSe solar cell.

5.1 Effect of precursor order on the performance of CZTSe solar cells

The order of metal elements in the stack precursors may affect the reaction of the elements and consequently influence the bulk properties of the CZTSe film. Usually, Cu is deposited as the last layer to suppress the decomposition reaction from the surface and decrease the loss of SnSe and Zn. In addition, formation of liquid CuSe at the beginning stages of annealing process leads to better crystallization and larger grains. Bigger grain size is reported for the stack orders in which Sn and Cu layer are beside each other because the formation of ternary $Cu_2SnS(Se)_3$ improves the crystal quality of the CZTSSe [19]. The stack order was already optimized in imec PV lab for precursors prepared by DC sputtering of $Cu_{10}Sn_{90}$, Zn, and Cu and the best results were achieved for a $Cu_{10}Sn_{90}$/Zn/Cu stack order [23]. Here we will investigate the effect of stack orders for e-beam evaporated precursors.

5.1.1 Fabrication of precursors with different stack orders:

Two set of precursors with different stack orders were deposited on Mo-coated SLG: (I) SLG/Mo/Sn(260)/Zn(125)/Cu(135) and (II) SLG/Mo/Zn(125)/Sn(260)/Cu(135). These precursors were selenized in RTP annealing system with the standard selenization recipe as explained in section 2.4. **Figure 5-1** shows the statistics of the efficiencies that has been achieved from several samples prepared from these two stacks. Each point in the graph represents the best efficiency of one sample including at least 12 solar cells. The scattering of the results that can be observed for both types of stacks shows the irreproducibility of the selenization process, as will be explained later. The best efficiency of 6.8 % was achieved for the stacks with Sn as the first layer (Type I) and the best efficiency of 6.6 % was achieved for the stacks with Zn as the first layer (Type II). It can be concluded statistically that these two types of precursors are quite similar regarding the efficiency of final solar cells. We chose Sn/Zn/Cu order as the baseline as there was no remarkable difference between these two types.

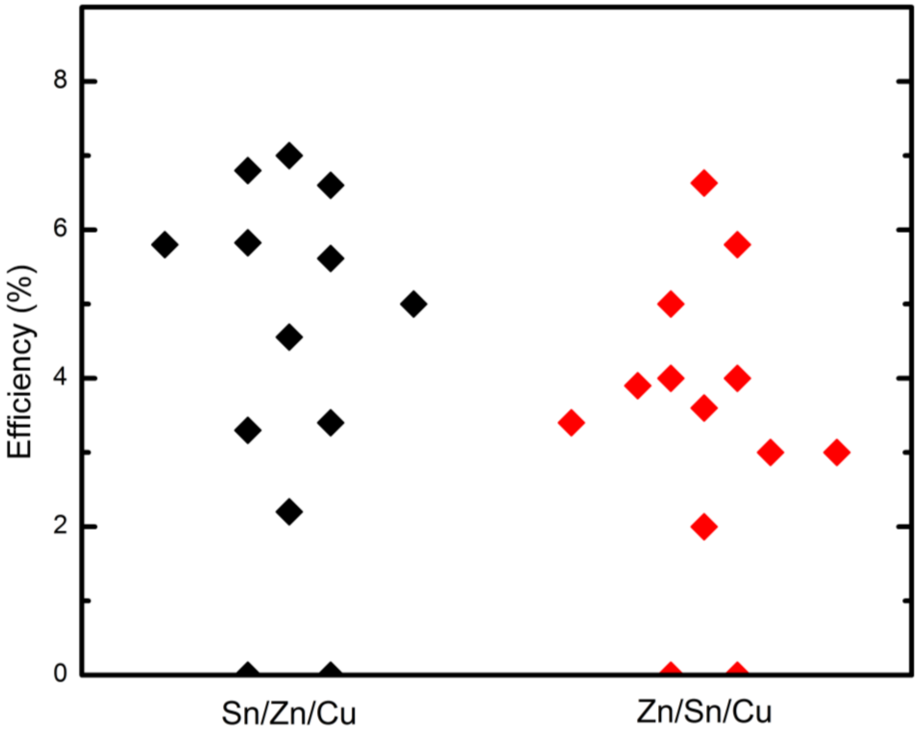

Figure 5-1 Best efficiencies of different samples prepared from precursor type (I) and (II) at different selenization runs.

5.2 Optimizing the selenization condition

To optimize the selenization condition, we varied several engineering parameters of the standard selenization recipe (See **Figure 2-2 (right)**) including the selenization temperature (440, **450**, 460, 470 and 480 °C), selenization dwell time (10, **15**, 20 min) and heating rate (0.5, **1**, 2 and 3 °C/s). We have observed that the standard selenization recipe (with the bold parameters) usually lead to the best results. The main issue of selenization at high temperatures (≥ 470 °C), fast ramping (≥ 2 °C/s) and long annealing time (≥20 min) was the delamination of the absorber from Mo after KCN treatment. In the next study, we investigate the effect of H_2Se flow rate during the selenization process.

5.2.1 Effect of H_2Se flow rate during the selenization process

In the baseline selenization recipe, the flow rate of H_2Se gas was 200 sccm. In order to keep the pressure below the safe pressure of the tool, which is 1 atm, two pumping steps were introduced during the 15 min selenization and the selenization chamber was pumped to 20 mbar when the pressure inside the chambers reaches to 990 mbar. In addition to the safety issue, introducing the pumping steps may have some advantages such as outgassing the residual gasses, the possibility to fill the chamber with a high H_2Se flow rate. However decreasing the pressure can also affect the reaction. It can increase the tendency toward decomposition reaction and increase the loss of volatile elements. In order to study the effect of the pumping during the selenization, we made 2 more selenization recipes with 150 and 80 sccm. By using 150 sccm H_2Se flow rate, only one pumping step is required in the middle of selenization and by using 80 sccm there is no need for pumping during the 15 min selenization.

Figure 5-2 shows the best efficiencies achieved for solar cells prepared by selenization at different flow rates. Each point in this figure represents the best efficiency of one sample including at least 12 solar cells. It can be observed that efficiencies from 0 to around 8 % can be achieved using all the 3 selenization recipes with 80,150 and 200 sccm. The scattering of the results again shows the irreproducibility of our fabrication process, as will be explained in the next section. It can be concluded statistically that all these 3 selenization recipes led to quite similar results in terms of efficiency and reproducibility. However, this study also suggests that there is no need of high flow rate of H_2Se and with a lower flow rate as 80 sccm (without a pumping step), we can still achieve similar results.

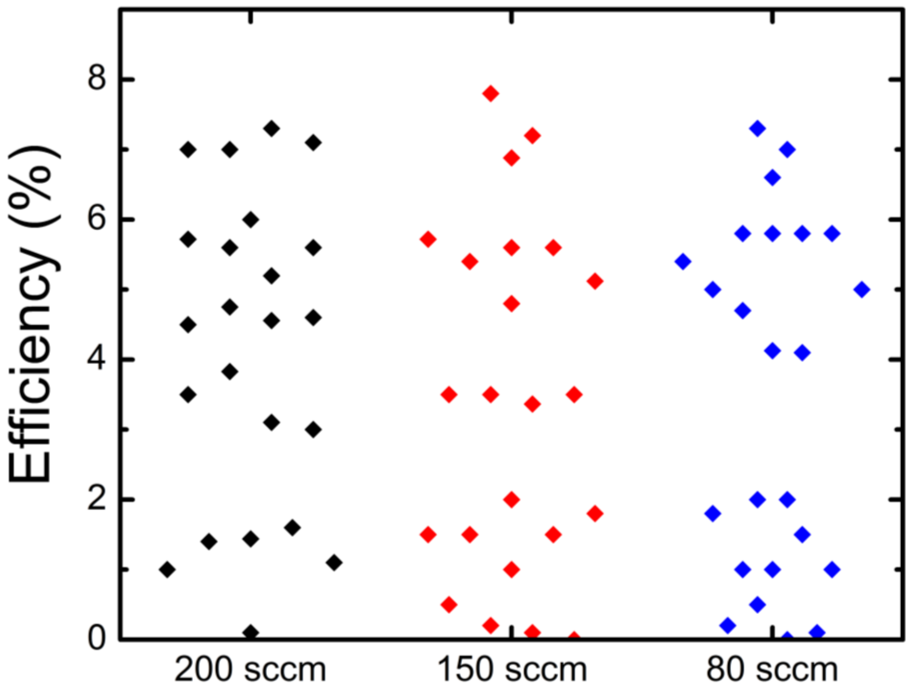

Figure 5-2 Best efficiencies achieved for different samples prepared by selenization at different flow rates at different selenization runs and different solar cell processing.

5.3 Irreproducibility of CZTSe solar cell fabrication process

Figure 5-3 shows the efficiency of some of the devices processed each month since July 2015 to June 2016. There is a big variation in the performance of the solar cells even though most of these samples had nominally the same processing recipes. In the following, we will discuss some of the possible reasons of irreproducibility in our baseline process.

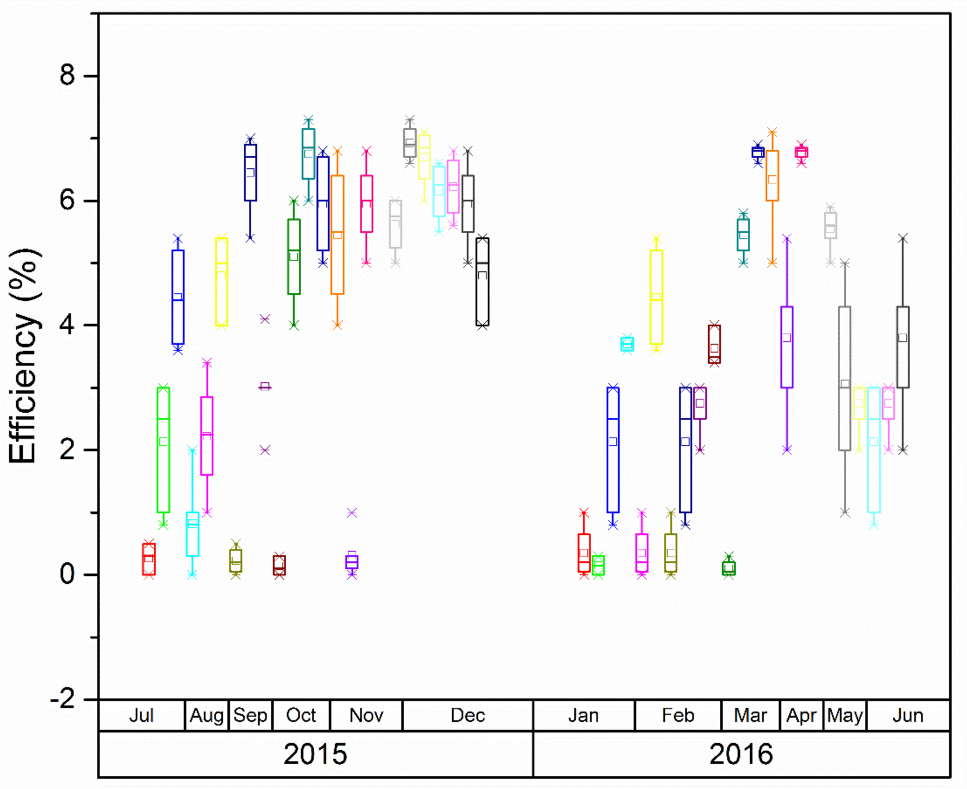

Figure 5-3 Efficiencies of some of the devices processed in our lab since July 2015 to June 2016.

5.4 Selenization irreproducibility

One of the main issues of our processing was selenization in the rapid thermal processor system. A memory effect observed in selenization process. **Figure 5-4** shows the best efficiency of solar cells prepared from absorber layers selenized in different days and in different selenization runs (Se-1 to Se-5). For example, in day 4, we did 5 selenization and the efficiencies of the samples selenized in the 1th, 2nd, 3rd, 4th and 5th run (represented by Se1,Se2, etc. in **Figure 5-4**) change from around 0 % to 7 %. It was found that samples selenized in the first selenization runs often has lower performance as compared to other samples and sometimes they had below 1 % efficiencies. Checking the history of these selenizations, we found that usually, this issue happens when other groups use the oven for sulfurization of their samples on different substrates such as Si wafers. Thus, this problem could be mainly due to a contamination in the chamber with Si, etc. To reduce the contamination, we used different susceptors for different samples. Also, an additional cleaning run was performed before starting a new series of selenizations. With those approaches, the reproducibility was improved. As it can be observed, the efficiency of the solar cell prepared from the absorber layer selenized in the first runs are higher than 3 %, in day 7 to 11 in which a cleaning run was introduced before the selenization. However, still, the efficiencies of solar cells prepared from absorbers selenized at different selenization runs are different. It may indicate that the irreproducibility of the selenization process exists. Another possibility could be the irreproducibility in other processing steps such as CdS and TCO deposition.

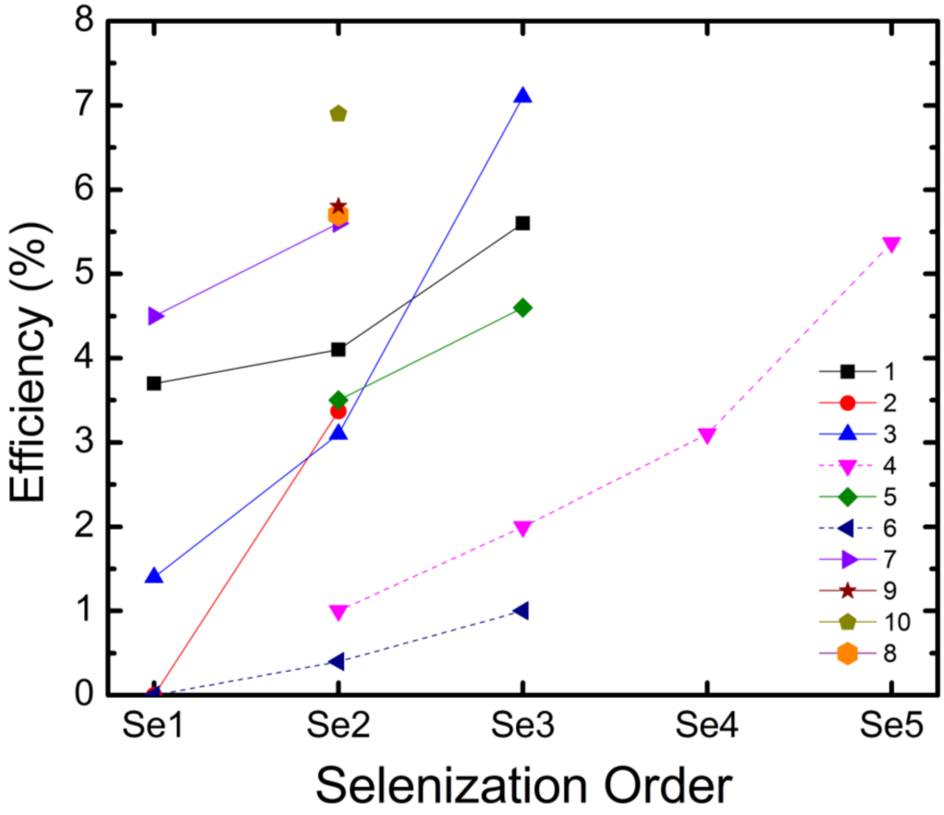

Figure 5-4 Best efficiencies of solar cells prepared from absorber layers selenized in different days (1-10) and in different selenization runs (Se1 to Se5).

5.5 Conclusion

Several processing parameters of our standard two-step fabrication technique of CZTSe absorber layers were studied in this chapter. It was observed that there is no significant difference between Sn/Zn/Cu and Zn/Sn/Cu precursors concerning the efficiency of final CZTSe solar cells. Moreover, the deviation of most of the parameters from standard selenization including selenization time, temperature, and ramping rate led to a lower performance of final solar cells. The effect of H_2Se flow rate was studied systematically. Selenization under three different values of flow rate including 200, 150 and 80 sccm in which 2, 1 and 0 pumping steps were required during 15 min selenization, was performed. It was observed, all these 3 selenization recipes can lead to 0 to 8 % efficiency that indicates using different flow rates or in other word introducing pumping steps during the selenization doesn’t have a remarkable impact on the performance of solar cells. As using a flow rate of 80 sccm during the selenization can lead to the same results as using 200 sccm, thus it is more convenient and cost effective to use this lower flow rate. Moreover, an irreproducibility or a memory effect was observed in the selenization process. This irreproducibility was reduced by introducing additional cleaning steps and avoiding the contamination sources.

6 Modification of CZTSe solar cell performance by Mo/MoO_{3-X} rear contact

Molybdenum (Mo) coated glass usually is used as the rear contact in CIGS and kesterite solar cells because of several advantages such as moderate reflectivity, good resistance to the selenization/sulfurization process and providing beneficial alkali elements such as Na and K for kesterite compound. Despite these advantages two main problems are attributed to the Mo rear contact in kesterite solar cells: (i) The decomposition reactions due to the instability of the Mo/kesterite interface that leads to the formation of secondary phases and voids at the rear surface that affect the film growth, and introduces defects into the absorber layer [32]. (ii) The existence of a Schottky barrier at the Mo/ kesterite interface decreases the hole transport and increases the recombination at the rear interface. Based on the thermal behavior of the series resistance (R_s) a barrier height up to 135 meV for CZTSe solar cells [35] and 320 meV for CZTS solar cells [87] are reported. In CIGS solar cell it has been shown that formation of a Mo chalcogenide layer decreases this Schottky barrier height [88]. However, in kesterite solar cells the formation of a too thick Mo chalcogenide layer due to the uncontrolled reaction between Mo and kesterite can be detrimental to the solar cell performance [31,51]. The existence of voids and secondary phases at Mo/CZTSSe rear surface is reported by several groups and we observed it frequently in our baseline samples in cross-sectional SEM and TEM images. **Figure 6-1** shows HAADF-STEM image and individual elemental maps of one of our baseline samples near the Mo rear interface. EDX spectra from the areas outlined in the HAADF-STEM image indicate the presence of Mo in region 1, Mo selenide and Cu-selenide in region 2 and 3. In this sample, Mo selenide and Cu-selenide layers and voids can be seen at the rear interface. These imperfections at the rear surface are detrimental to the performance of solar cells. The pores at the rear surface are not good for the adhesion of the film and they can suppress the charge carrier transport and decrease the J_{SC}. The decomposition of CZTSSe at the rear interface may introduce deep defects such as Se and Sn vacancies that increase the rear recombination rate at the rear interface and decrease of the open circuit voltage (V_{OC}).

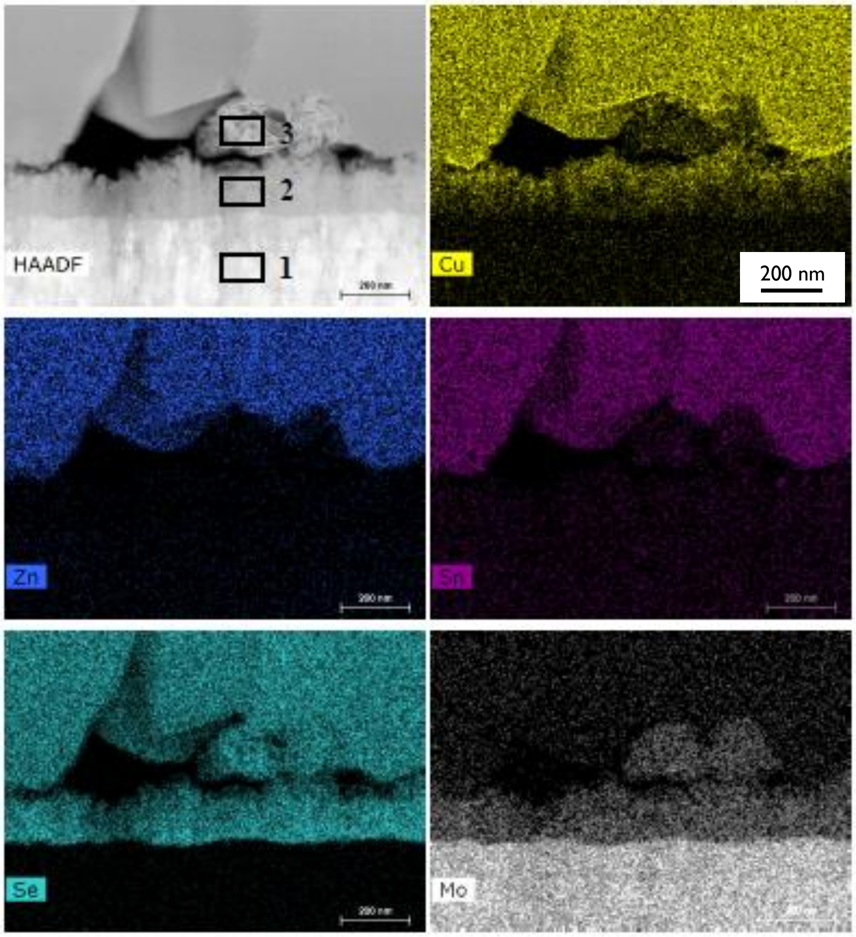

Figure 6-1 HAADF-STEM image and individual elemental EDX maps of a standard CZTSe solar cell.

To address these issues related to the Mo rear contact, different interfacial layers have been introduced between the Mo and absorber layer such as TiN [32,35,51], TiB [34], Ag [37], ZnO [36], Al_2O_3 [55], MoO_2 [33], etc. TiN layer was reported as a promising candidate to avoid the decomposition reactions [32] and also to improve the band alignment by decreasing the barrier height to 15 meV [35]. Ultra-thin ZnO layer was also introduced as an inert layer for avoiding the decomposition reactions [36], although it's an n-type semiconductor and it can alter the band alignment. Recently, using thermally evaporated MoO_2 layer, large open circuit voltage (V_{OC}) around 460 mV was achieved for a CZTSe solar cell [33]. We investigated several interfacial layers. By introducing sputtered TiN and ZnO no improvement has been achieved compared to our baseline solar cells. Using a solution based NiO interfacial layer (~ 10 nm) led to severe degradation of the solar cells mainly due to the diffusion of Ni into the CZTSe layer during the selenization process. Here we will report only the result achieved by introducing a MoO_{3-X} interfacial layer as it looks very promising. MoO_{3-X} layers were synthesized by an easy, fast and reproducible solution based process. Solution processed MoO_{3-X} is an appropriate interfacial layer for the rear contact application because it is a wide band gap p-type semiconductor (~ 3.8 eV) with high work function (~ 6.8 eV [89]) compared to the Mo rear contact that has a work function around 4.5 eV. Using a solution-based method has many advantages compared to thermally evaporated MoO_{3-x} layer. Besides reproducibility, feasibility, cost-effectiveness and industrial viability, solution-based techniques lead to conservation of highest oxidation state 6+ for the MoO_{3-X} layer ($X\rightarrow 0$), hence keeping its work function as high as possible. When MoO_{3-X} material is thermally evaporated - due to heat - some amount of oxygen is lost during the processing, which leads to lowering the oxidation state and formation of MoO_2 layer. Lower oxidation states of MoO_{3-x} leads to a lower work function (MoO_2 work function is ~ 5.9 eV [89]) compared to high work function of MoO_3. The Schottky barrier (ϕ_b) at the interface of a metal/ p-type semiconductor depends on the work function of the metal, the bandgap (E_g) and electron affinity (χ) of the semiconductor [52]:

$$\phi_b = E_g + \chi - \phi_m \qquad \text{Equation 6-1}$$

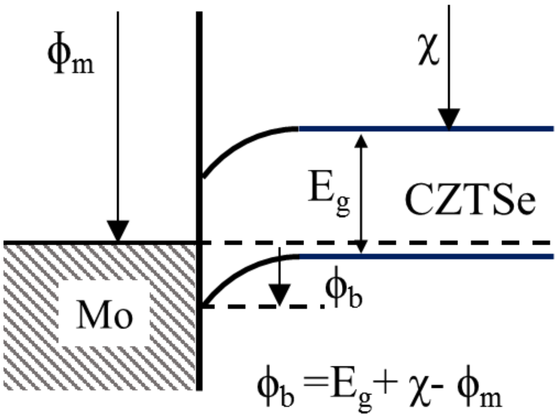

Figure 6-2 Band diagram at the Mo/CZTSe interface.

By using a p-type interfacial layer with high work function the barrier height will decrease and disappear if $\phi_m \geq (E_g + \chi)$ as shown schematically in **Figure 6-2**.

According to our previous study, explained in chapter 4, the thickness of the absorber layer is an important factor for the performance of CZTSe solar cells. We observed that by increasing the thickness of the absorber layer the performance of the solar cells improved significantly and part of this improvement was attributed to less recombination at the rear interface. By increasing the thickness, the distance between the p-n junction and the rear surface increases which lead to less rear interface recombination and enhancement of the minority carrier lifetime and V_{OC} [25]. Thus in this study, we aim to introduce an appropriate interfacial layer at the rear interface of kesterite solar cell, mainly to improve the band alignment, avoid the decomposition reactions and enhance the rear interface quality.

6.1 Preparation of SLG/Mo/MoO_{3-X} rear contact

Two types of rear contact were used in this study: (i) conventional Mo-coated Soda Lime Glass, SLG/Mo and (ii) Mo-coated SLG with an ultra-thin layer of MoO_{3-X} (thickness ~10 nm), SLG/Mo/MoO_{3-X}. Mo-coated SLG substrates were prepared and cleaned as explained in section 2.1. MoO_{3-X} was synthesized by spin coating of Ammonium Molybdate on SLG/Mo substrate. The speed for spin coater was set to 1000 rpm, with an acceleration of 5000 rpm/s^2. The substrates were rotated for 30 s and then were annealed on a hot plate at 200 °C for 10 min. More details about the physical characterization of this MoO_{3-X} layer are explained in reference [90].

6.2 CZTSe solar cells with SLG/Mo and SLG/Mo/MoO_{3-X} rear contact

CZTSe absorber layers were prepared in a two-stage process. First e-beam deposition of Sn, Zn and Cu followed by selenization of precursors by 10 % H_2Se gas diluted in N_2 for 15 min at 460 °C in a rapid thermal processing system with 1 °C/s heating rate, as explained with more details in section 2.4. Here the effect of the MoO_{3-X} interfacial layer for two types of solar cells is investigated: (a) solar cells with thin absorber layers prepared by selenization of Sn(215 nm)/Zn(100 nm)/Cu(110 nm) stack and (b) solar cells with thick absorber layers prepared by selenization of Sn(310 nm)/Zn(150 nm)/Cu(160 nm) stack. The final thickness of the absorber layers after the selenization is measured by cross-sectional scanning electron microscopy (SEM) to be around 1 µm and 1.7 µm for the thin and thick absorbers, respectively. Solar cells were then synthesized after KCN treatment, chemical bath deposition of CdS (~ 50 nm), sputtering of intrinsic ZnO (~ 50 nm) and Al-doped ZnO (~ 300-400 nm) and finally evaporation of Ni/Al/Ni grids. Solar cells with 0.5 cm^2 area were isolated laterally by needle scribing. Solar cells in this study were annealed in N_2 atmosphere at 200 °C for 1 hour and all the optical and electrical characterizations reported here are performed after the post-annealing step. The beneficial impact of this post annealing step was already reported by several groups [91]. Samples are named according to their rear contact type: with MoO_{3-X} layer (S) and without MoO_{3-X} layer (R). S/R-(i=1,2) samples are made from thin absorber layer while S/R-(i=3,4) are made from thick absorber layer.

6.3 Time Resolved-Photoluminescence (TR-PL) measurements

In **Figure 6-3**(a) and (b) the TR-PL spectra of the solar cells with Mo and Mo/MoO_{3-X} rear contacts are compared for thin and thick devices, respectively. Solar cells with MoO_{3-X} layer have longer PL decay time compared to the reference samples. Generally, the PL decay time is also remarkably longer for thicker devices, thus it can be concluded that both the rear surface and the bulk quality of CZTSe solar cells affect the recombination and consequently the minority carrier lifetime.

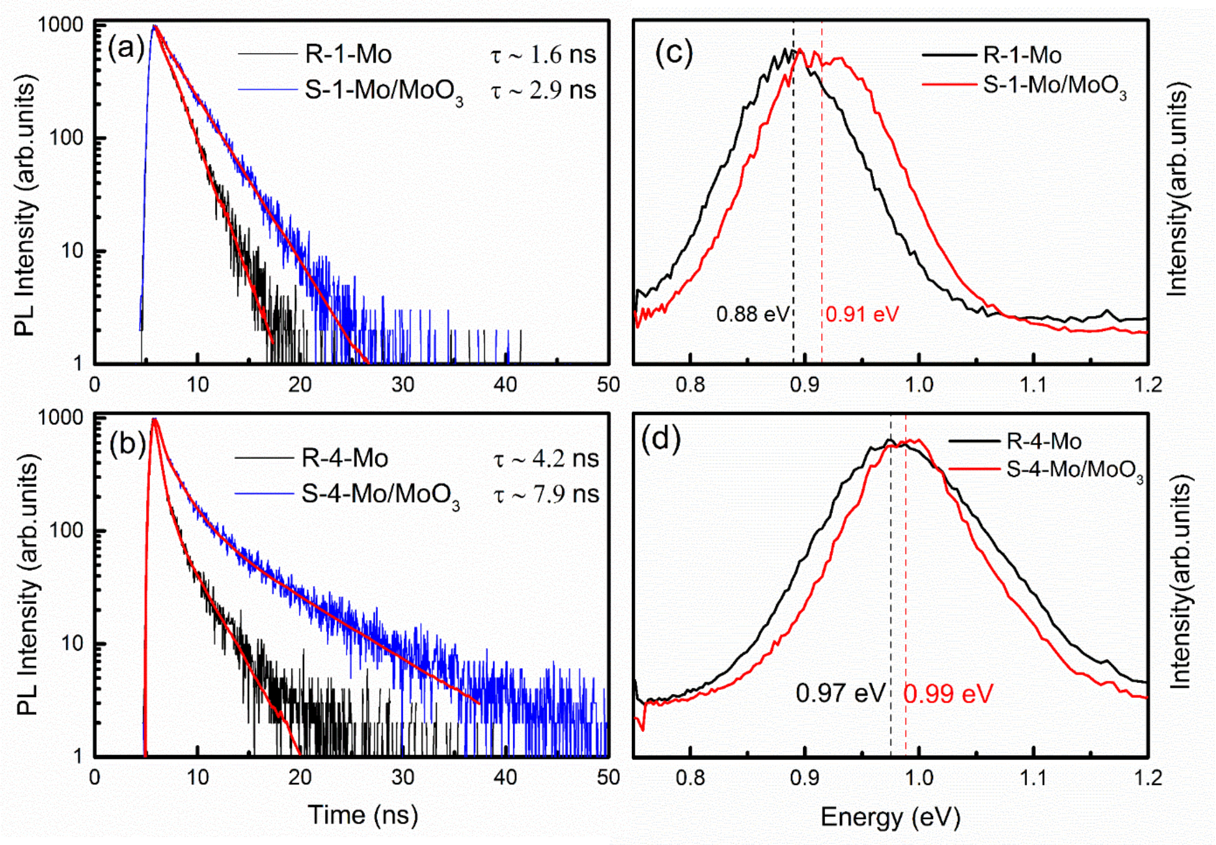

Figure 6-3 Room temperature TR-PL spectra of the samples with and without MoO_{3-X} layer (a) thin samples and (b) thick samples. Room temperature PL spectra of (c) thin and (d) thick samples.

The photoluminescence spectra of the thin and thick solar cells are also shown in **Figure 6-3(c)** and **(d)**, respectively. It can be observed that the PL peaks of solar cells with MoO_{3-X} layer move slightly toward higher energies closer to the band gap of CZTSe (1 eV). The PL peak shift is more pronounced in thin solar cells in which the effect of the rear surface is more important. It is reported that the PL peak position of kesterite solar cells is lower than their bandgap due to the existence of a large amount of tail states and potential fluctuation [63,82]. Part of the tail states in kesterite can be attributed to the formation of defects such as Sn and Se vacancies due to the decomposition reactions at the rear surface [31].

6.4 Electrical characterizations

In **Figure 6-4** the device parameters of 4 samples (each sample includes at least 12 solar cells) with MoO_{3-X} layer (S-i=1-4) are compared with their references (R-i=1-4). (e.g. S-1 is prepared under the same condition as its reference R-1). In general, by introducing the MoO_{3-X} layer the V_{OC} improved significantly while short circuit current (J_{sc}) and Fill Factor (FF) did not change considerably. Moreover, J_{SC} and FF improved significantly by increasing the thickness, mainly due to an enhanced bulk quality of the CZTSe absorber layer - as described in previous chapter.

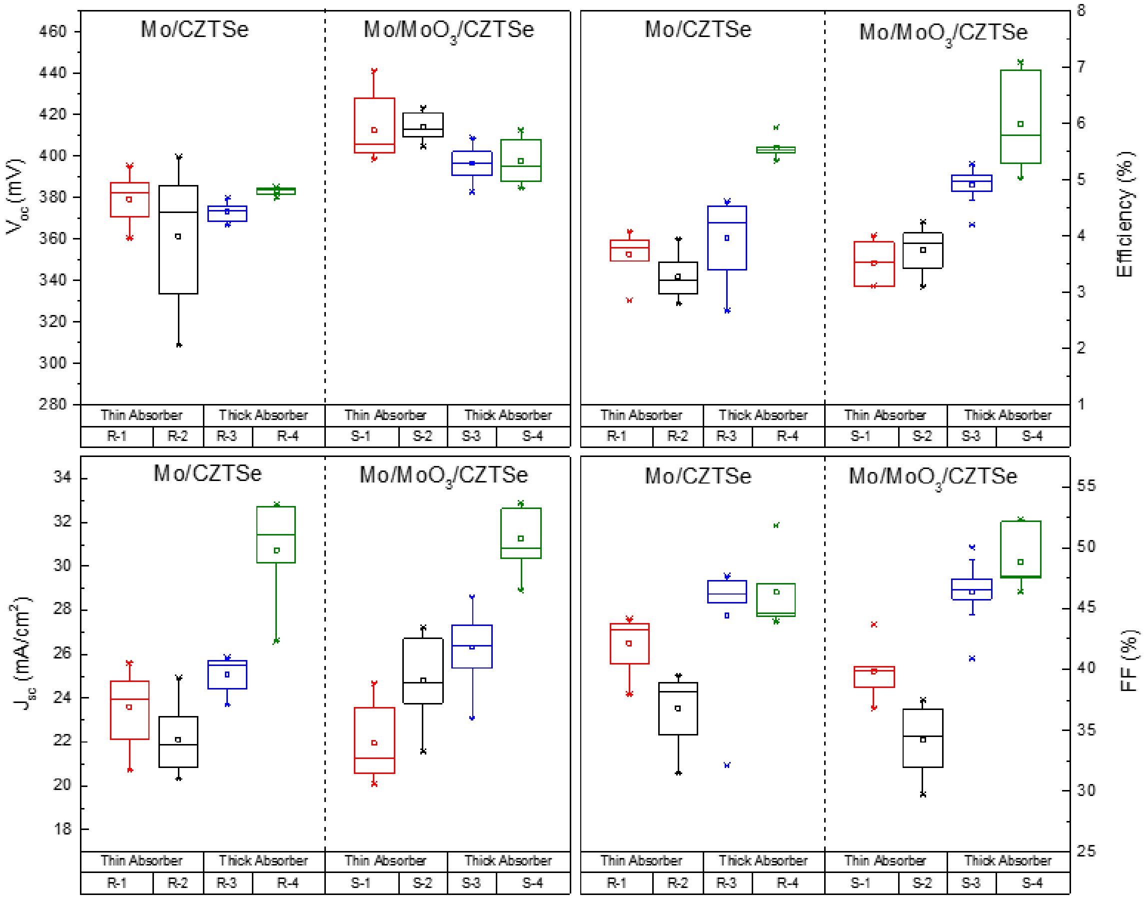

Figure 6-4 Electrical parameters of the samples made with/without MoO_{3-X} layer (S/R). Each box represents values measured from samples containing at least 12 solar cells.

Table 6-1 Electrical parameters of the best solar cells of the samples with different rear contact and absorber thickness: short circuit current (J_{sc}), open circuit voltage (V_{OC}), fill factor (FF), efficiency (η), shunt resistance (R_{sh}), series resistance (R_s) and ideality factor (A).

Sample	**Rear contact**	**Thickness** (µm)	**VOC** (mV)	J_{sc} (mA.cm^2)	**FF** (%)	**η** (%)	R_{sh} (Ω.cm^2)	R_s (Ω.cm^2)	**A** (/)
R-1	Mo	1	395	23.9	43.2	4.1	113	1.3	3.1
S-1	Mo/MoO_{3-X}	1	441	24.7	36.8	4	171	1	3.9
R-4	Mo	1.7	384	32.8	47	5.9	164	2.1	2.6
S-4	Mo/MoO_{3-X}	1.7	413	32.9	52.3	7.1	311	1.7	2.4

The AM 1.5 illuminated Current density-Voltage (J-V) curve of the champion solar cells with/without the MoO_{3-X} layer of one of the thin samples (S/R-1) and one of the thick samples (S/R-4) are illustrated in **Figure 6-5 (a)** and **(b)**, respectively. The diode parameters of the devices are derived by the procedure explained in reference [77], and are summarized in **Table 6-1**. Introducing the MoO_{3-X} layer leads to the significant improvement of V_{OC} from 395 to 441 mV for thin solar cells and from 384 to 413 mV for thick solar cells. Even though solar cell S-1 has a relatively large V_{OC} of 441 mV, it is suffering from low FF and quite large ideality factor (A). Large ideality factor above 2 indicates peculiar recombination mechanisms such as tunneling enhanced recombination, donor-acceptor pair recombination or fluctuation of activation energy of the main recombination path [53].

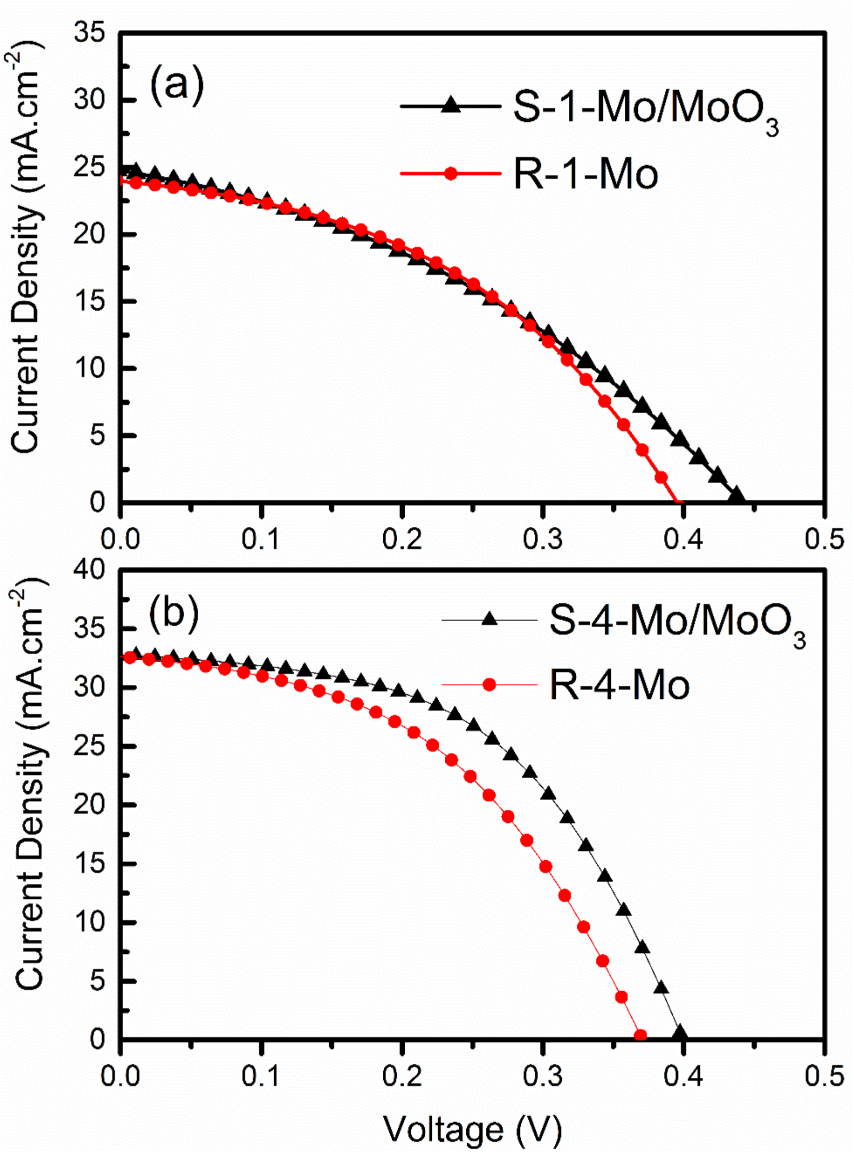

Figure 6-5 (a) Illuminated J-V curve of the champion thin and **(b)** thick solar cells with/without the MoO_{3-x} layer (S/R-1).

The illuminated and dark J-V curves of the best thin solar cells R-1 (without MoO_{3-X}) and S-1 (with MoO_{3-X}) were measured at different temperatures, as shown in **Figure 6-6** and **Figure 6-7**.

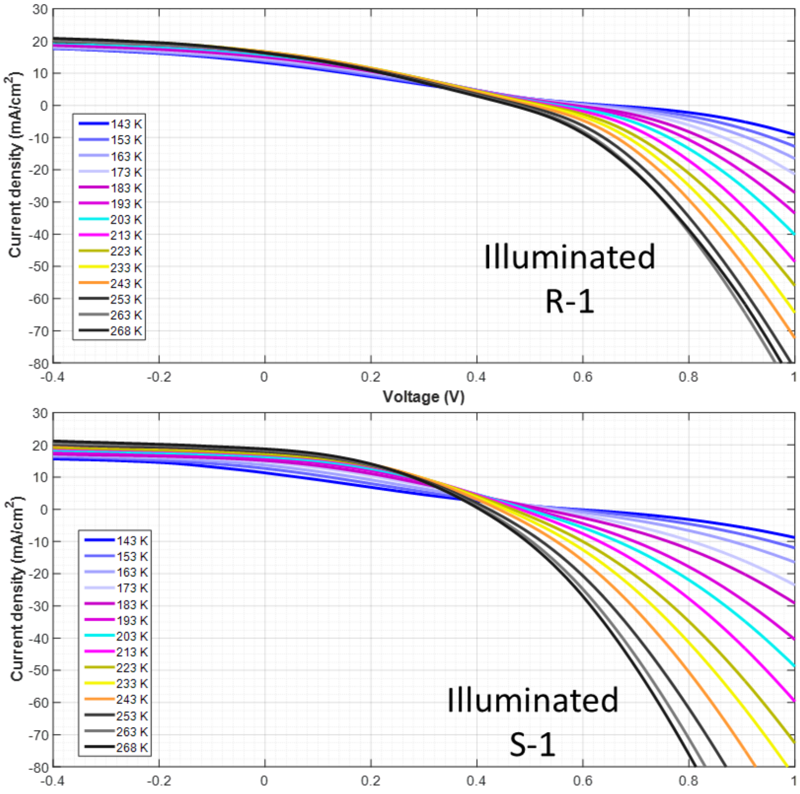

Figure 6-6 Illuminated curve of the best thin solar cells with/without MoO_{3-x} (R-1/S-1) were measured at different temperatures.

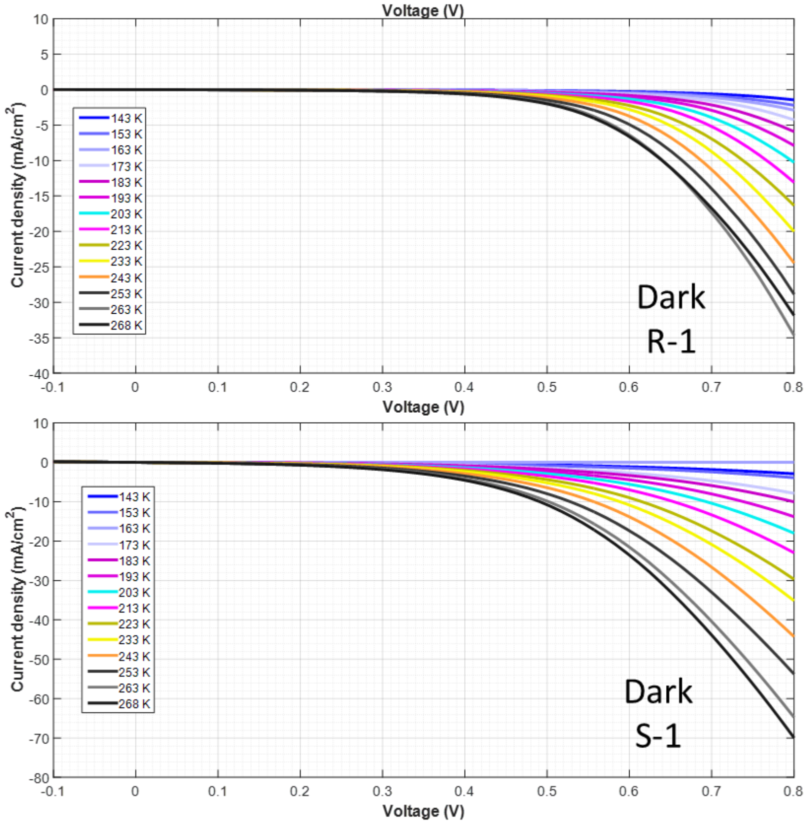

Figure 6-7 Dark J-V curve of the best thin solar cells with/without MoO_{3-x} (R-1/S-1) were measured at different temperatures.

Thermal behavior of V_{OC}, series resistance, Arrhenius plot of series resistance and ideality factor/dark saturation current are illustrated in **Figure 6-8 (c), (d), (e), (f),** respectively. As can be seen in **Figure 6-8 (c)** and **(d)** solar cells with and without MoO_{3-X} layer show quite similar series resistance (R_s) thermal behavior. By making an Arrhenius plot of R_s [92] the barrier height (ϕ_b) is estimated to be around 30 meV for both solar cells, i.e. with and without MoO_{3-X} layer (See **Figure 6-8 (d)**). Low barrier height of S-1 and R-1 indicates a good band alignment between Mo and CZTSe and can be due to the formation of a thin $MoSe_2$ layer, ($MoSe_2$ is found in XRD pattern of the CZTSe absorber layers, see **Figure 6-9**).

In **Figure 6-8 (e)** the thermal behavior of V_{OC} of the solar cells S-1 and R-1 are shown. The temperature dependence of V_{OC} can be explained by equation 6-2:

$$V_{oc} = \frac{E_A}{q} - \frac{AkT}{q}\ln\left(\frac{J_{00}}{J_L}\right) \qquad \text{Equation 6-2}$$

where E_A, A, k, J_{00}, and J_L are the activation energy, diode ideality factor, Boltzmann constant, reverse saturation current pre-factor, and the photocurrent, respectively [77]. Reverse saturation current pre-factor is related to the dark saturation current according to equation 6-3:

$$J_0 = J_{00}\exp(-\frac{E_A}{AkT}) \qquad \text{Equation 6-3}$$

Generally, the activation energy (E_A) is correlated to the main recombination path in the solar cell. When the bulk recombination is dominant then $E_A \sim E_g$ (E_g is the band gap of the absorber layer) while in the case of interface recombination (including the rear or front interface) $E_A < E_g$ [77]. However, other factors such as band gap fluctuation in the absorber layer (that is very likely in CZTSe) can also lead to lower activation energy than bandgap [53]. As shown in **Figure 6-8 (e)**, a solar cell with MoO_{3-X} has higher E_A around 837 meV compared to the reference solar cell for which E_A is around 770 meV. In **Figure 6-8 (f)**, the dark saturation current density (J_0) of solar cells with and without MoO_{3-X} layer at various temperatures, derived at intermediate voltage.

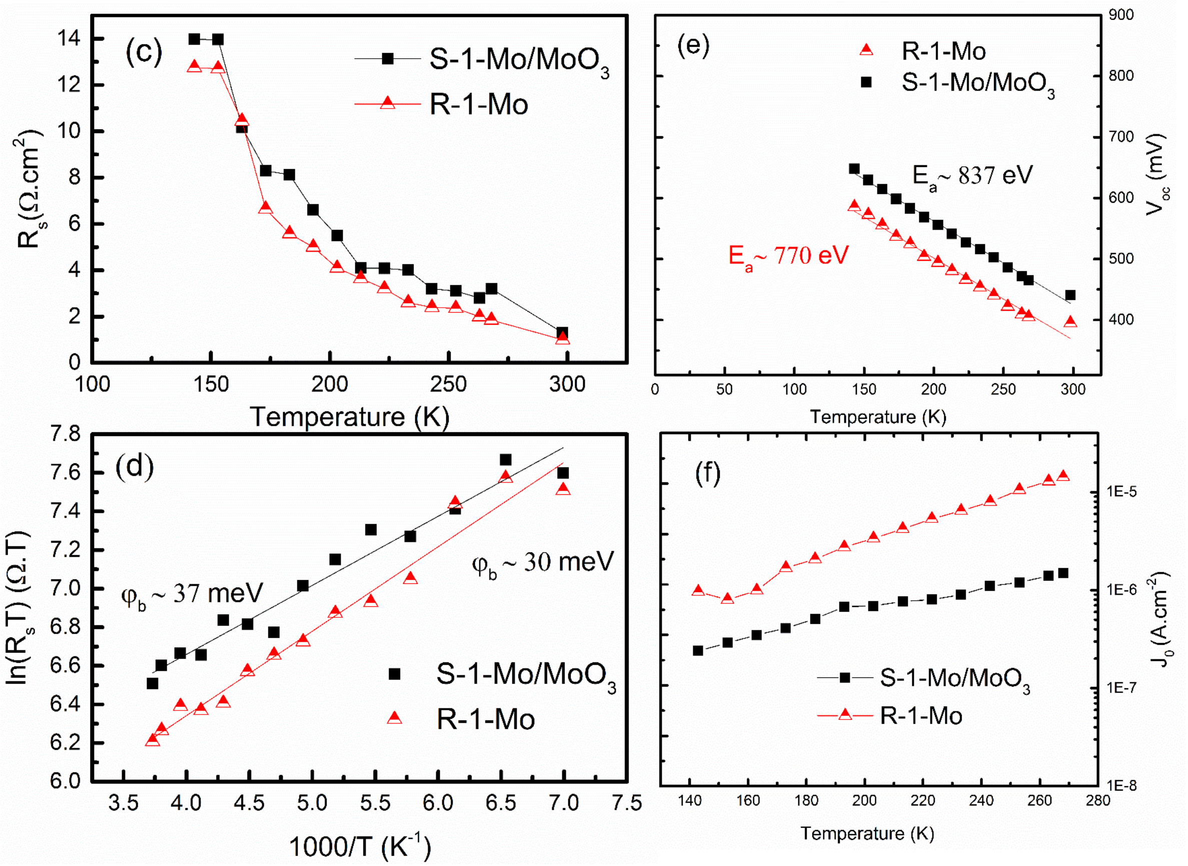

Figure 6-8 (c) Thermal behavior of series resistance (R_S), (d) Arrhenius plot of R_S, (e) Thermal behavior of V_{OC} and (f) dark saturation current (J_0) of the best thin solar cells with/without MoO_{3-x} layer (S-1/R-1).

Based on the optical and electrical measurements of this study, the beneficial effects of MoO_{3-X} layer is mainly due to the reduction of recombination. Larger V_{OC} of solar cells with MoO_{3-X} interfacial layer along with other results including higher activation energy, lower J_0 and longer minority carrier lifetime indicate a reduction of recombination. This might be due to the reduction of the decomposition reactions at the rear interface by introducing MoO_{3-X} layer and improvement of the rear surface quality. Several studies have already reported the instability of Mo during the selenization/sulfurization process that leads to the formation of voids, and secondary phases and introduce defects such as Se vacancies [16-25]. Another hypothesis could be the role of oxygen in passivation of defects, as in high temperature processing the oxygen can be released and fill the different vacancies.

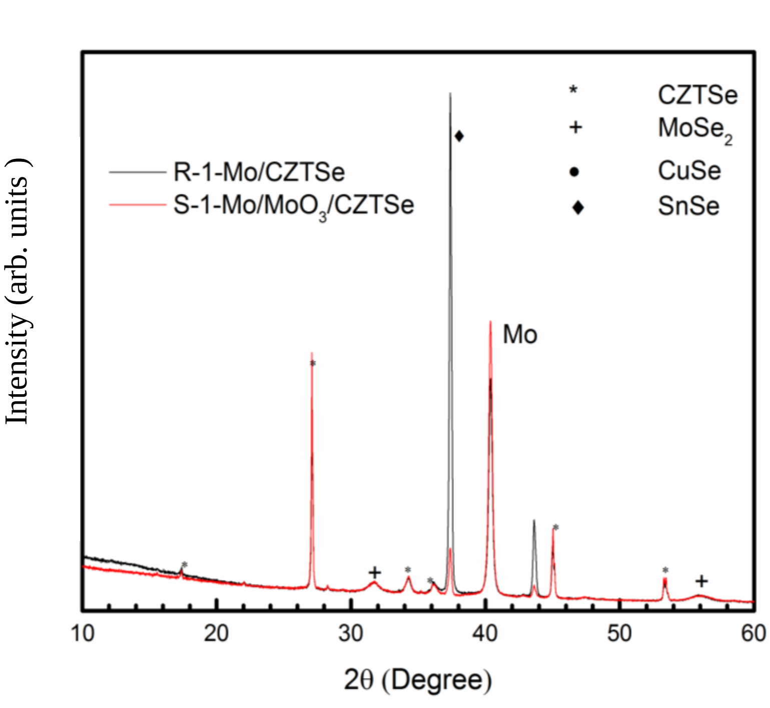

Figure 6-9 XRD pattern of the thin samples with/without MoO_{3-X} layer.

In order to investigate the impact of the MoO_{3-X} layer on the diffusion of alkali eement such as Na, GDOES measurements were performed on solar cells after removing the transparent conducting oxide and CdS layers by etching in diluted HCl. In **Figure 6-10** **(a)** and **(b)** the depth profile of different elements including Na in the reference solar cell R-4 (with Mo rear contact) and S-4 (with Mo/MoO_{3-X} rear contact) are shown, respectively. The GDOES measurements indicate that Na diffusion is even slightly higher in solar cells with MoO_{3-X} layer compared to the reference solar cells, thus MoO_{3-X} layer is not a barrier for diffusion of Na.

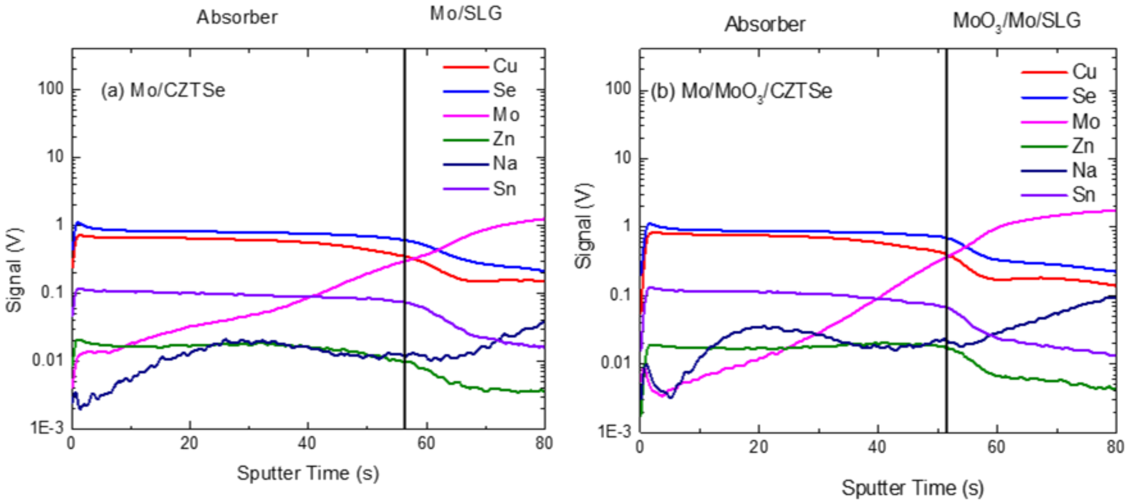

Figure 6-10 (a) GDOES measurements of SLG/Mo/CZTSe and (b) SLG/Mo/MoO_3/CZTSe. Sputter time = 0 s is the top surface of the CZTSe absorber layer.

In **Figure 6-11** top view SEM images of the corresponding absorber layers after removing the top layers are shown. SEM images revealed that the absorber layers especially the one prepared on conventional Mo substrate suffer from the existence of too many voids and secondary phases mainly ZnSe. The average chemical composition of normal regions (such as A) measured with EDS was Zn/Sn ~ 1.1, Cu/(Zn+Sn) ~ 0.8, and Se/(Cu+Zn+Sn) ~ 1.1. While, the average composition of the white spots (B) was Zn/Sn ~ 4, Cu/(Zn+Sn) ~ 0.3 and Se/(Cu+Zn+Sn) ~ 1.5. The CZTSe layer prepared on Mo/MoO_{3-X} substrate looks more compact and uniform with less secondary phases compared to the CZTSe layer on Mo substrate. Better morphology can be achieved due to the improvement of rear surface quality and better growth condition.

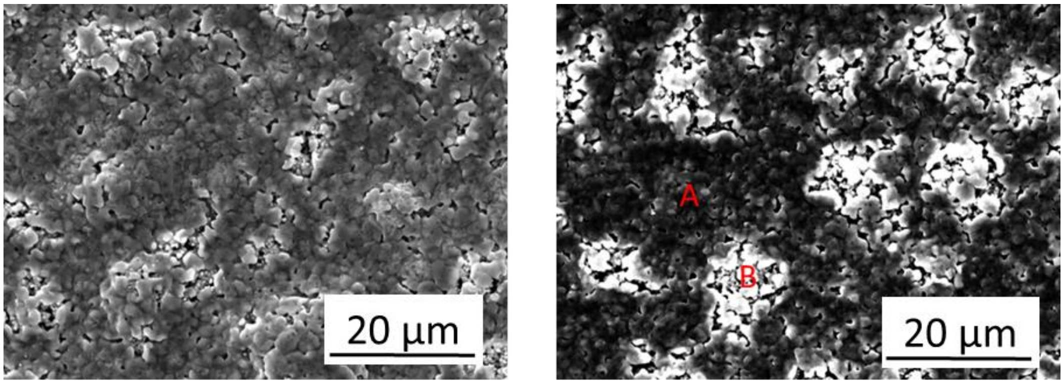

Figure 6-11 Top view SEM images of (left) sample R-4 (SLG/Mo/CZTSe) and (right) S-4 (SLG/Mo/MoO_{3-X}/CZTSe).

6.5 Conclusions

In this study, the effect of rear contact on the performance of two types of CZTSe solar cells including solar cells with thin and thick absorber layer was studied. It was shown that by introducing an ultra-thin layer of MoO_{3-X} between Mo rear contact and CZTSe absorber layer the minority carrier lifetime and V_{OC} improve remarkably. J_{SC} and FF did not change considerably by introducing the MoO_{3-X} layer but they improved significantly by increasing the absorber layer thickness. The temperature dependent J-V measurement showed that the band alignment at the rear interface doesn't change considerably by adding the MoO_{3-X} layer and the activation energy of the main recombination path shifts toward the higher energies. Top view SEM images of the absorber layers revealed that samples prepared on MoO_{3-X} layer are more uniform and compact. Thus, according to these measurements, the main role of MoO_{3-X} layer can be explained as avoiding or reducing the reaction between Mo and CZTSe during the selenization process and passivation of defects. The best solar cell in this study was the thick one with MoO_{3-X} interfacial layer that showed a 7.1 % conversion efficiency.

7 Modification of $Cu_2ZnSnSe_4$/CdS junction by introducing solution processed TiO_2 layer

Kesterite/CdS junction has a crucial impact on the performance of the kesterite solar cells. There are two main concerns about this junction: (i) the importance of band alignments at the absorber layer/buffer layer junction [58,59] and (ii) decomposition reactions of kesterite during the fabrication process that occur at the top surface [32,39]. According to the theoretical calculations by Minemoto et al. [58] the conduction band offset between the CIGS absorber layer and buffer layer has a crucial impact on the electrical parameters of CIGS solar cells. Based on this study a negative offset, also called cliff like band alignment, in which the conduction band of the buffer layer is lower than the one of the absorber layer (see **Figure 7-1b**) decreases the VOC in CIGS/CdS solar cells. This negative offset is a barrier for injected electrons under forward bias that leads to accumulation of injected electrons and increasing of the recombination. On the other hand, a positive offset, known as a spike like conformation (see **Figure 7-1a**) is not a barrier for injected electrons but for photogenerated electrons. If this positive offset is below 0.4 eV, photogenerated electrons can pass the barrier through the thermionic emission but when it is higher than 0.4 eV, it suppresses the transition of photogenerated electrons leading to the decrease of J_{SC} and FF [58]. The band alignment between CZTSe and CdS is reported to be a spike like band alignment with an offset value of 0.48 [93] or 0.34 eV [94] that is almost near to the optimum value.

Decomposition reactions during the fabrication process of kesterite absorber layer lead to the poor quality of the interfaces. Although several groups tried to suppress the decomposition reactions at the rear surface by introducing interfacial layers [36,38,55] and at the top surface by optimizing the fabrication process [39], these reactions, especially at the top surface, persist. The decomposition reactions at the top surface lead to the formation of secondary phases such as $SnSe_X$ and Cu_XSe. Even though chemical cleanings such as KCN treatment can remove most of these secondary phases [70] the formation and etching of these secondary phases can introduce defects, vacancies, and dangling bonds. Recently, several studies focused on

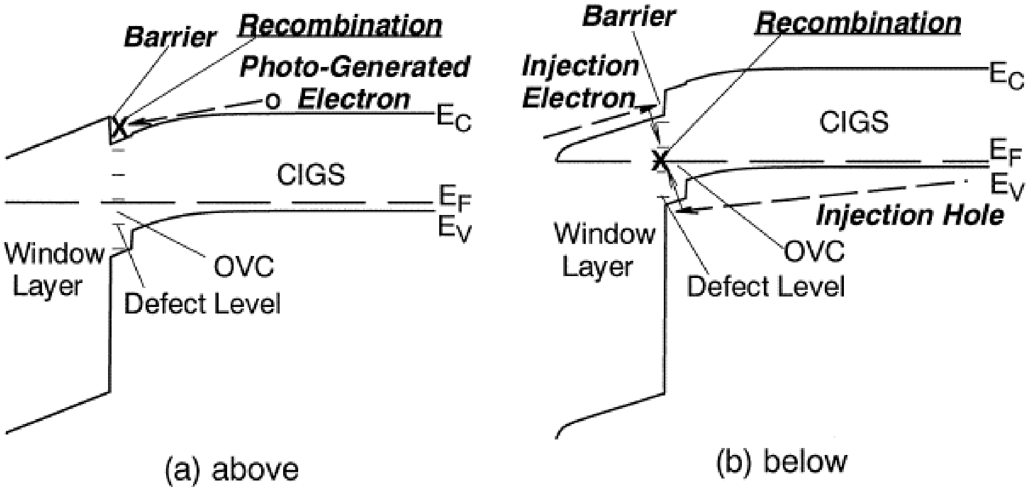

Figure 7-1 Schematics of band diagram of buffer layer/CIGS absorber structure when the conduction band of buffer layer is above (a) and below (b) that of CIGS [58].

passivation of the p-n junction in kesterite solar cells by introducing n-type metal oxide layers such as Al_2O_3 [61,62] or TiO_2 [60] layers between the kesterite absorber and CdS buffer layers which did improve V_{OC}. The beneficial effect of these passivation layers can be explained by reducing the interface recombination by chemical passivation (reduction of interface trap density) and field effect passivation (formation of a fixed charge density and consequently decreasing the charge carrier concentration at the interface) [55,95]. However, these passivation layers might have several drawbacks such as high resistivity and not optimized band alignment that can suppress the charge transport. Hence, passivation layers with nano-sized openings are desirable to improve the charge transport since the interface can be partially passivated while the photo generated carriers can be collected by use of the lateral openings. Passivation layers with nano-sized point openings have been already used in thin film solar cells including Cu(In,Ga)Se_2 [96–100] (and references therein) and CZTS [55] solar cells. So far, atomic layer deposition (ALD) is typically used for deposition of passivation layers and several approaches, e.g. e-beam lithography [55,98], are used to create the nano-sized openings through these layers. In this study, we introduce an easy and fast solution processed technique to synthesize a TiO_2 interfacial layer with lateral openings to be used as a promising passivation layer at the CZTSe/CdSe junction.

7.1 Experimental details

The processing steps of the modified CZTSe solar cells are shown in **Table 7-1**. CZTSe absorber layers were prepared by a two-step approach including e-beam deposition of Sn(310 nm)/Zn(150 nm)/Cu(160 nm) stack precursors followed by selenization in 10 % H_2Se gas in the N_2 atmosphere using a rapid thermal processing system. Standard CZTSe solar cells were processed after KCN treatment, chemical bath deposition of CdS buffer layer, sputtering of i-ZnO/Al-ZnO and e-beam evaporation of Ni-Al-Ni. In modified solar cells, a layer of TiO_2 was deposited on top of the CZTSe absorber layer after KCN etching and before the CdS deposition. We used two types of TiO_2 layers and named as (i) closed and (ii) open TiO_2 layers. To deposit the closed TiO_2 layer, an ethanol-based solution (sol-gel) was spin coated with 1000 rpm, 5000 rpm/sec^2 for 60 seconds. The closed TiO_2 layer is ready directly after the coating at room temperature and does not need any further treatment. This TiO_2 sol-gel and its physical and chemical properties are explained in more details in the reference [101]. The open TiO_2 layer was deposited in two steps, first, a closed TiO_2 layer was deposited on the CZTSe absorber layers and then another KCN treatment was performed on the samples.

Table 7-1 Overview of all steps required to fabricate closed and open TiO_2 layers.

Step	Description
1	Mo-coated SLG cleaning in 1 molar NH_4OH/Deionized water
2	e-beam evaporation
3	Selenization in 10 % H_2Se in N_2 at 460 °C
4	2 min KCN treatment
5	deposition of closed TiO_2 by spin coating
6	2 min KCN treatment only for open TiO_2
7	CBD CdS deposition
8	(i-)ZnO/Al-ZnO window sputtering
9	0.5 cm^2 solar cell scribing
10	Annealing in N_2 at 200 °C for 1 hour

The KCN treatment includes dipping the samples in a 5 wt % KCN solution in H_2O for 2 min, followed by rinsing the samples in deionized water and drying with an N_2 gun. Solar cells were annealed in N_2 atmosphere at 200 ºC for 1 hour and all the characterizations reported here are performed after this post-annealing step.

In this study, we present the results of one sample with closed TiO_2 (as named sample 1), four samples with open TiO_2 (samples 3, 5, 7 and 9) and their references (samples 2, 4, 6, 8 and 10, respectively). Each sample includes at least 12 solar cells and samples with TiO_2 layer (sample i, i=1, 3, 5, 7 and 9) were prepared along with their references (sample i+1) at the same processing condition to exclude the effect of irreproducibility of the fabrication process.

7.2 Results and discussions

High angle annular dark field scanning transmission electron microscopy (HAADF-STEM) images and energy dispersive X-ray (EDX) maps were acquired using an FEI Osiris microscope and Titan^3 microscope equipped with a Super-X detector and operated at 200 kV. EDX maps are generated from the intensity of the Mo-K, Se-K, Cu-K, Cd-L, Zn-K, Sn-L, S-K, Ti-K, O-K, C-K lines. The specimens for TEM were prepared using the focused ion beam (FIB) technique, on a Be support.

Overview HAADF-STEM images and STEM-EDX maps of the samples 1 (with closed TiO_2 layer), 3 (with open TiO_2 layer) and 4 (the reference of sample 3) are shown in **Figure 7-2**. The bluish areas on the STEM-EDX maps correspond to the occurrence of ZnSe grains. According to the STEM-EDX analysis a layer of $MoSe_2$ (~ 200-300 nm) and on top of it, a thin layer of copper selenide exists at the rear interface, in all samples. Note that in the samples 1 and 4 the CZTSe grains are densely packed. However, there are two different regions in sample 3, one consists of big and densely packed grains and the other region consists of small grains (inside the dashed circle). According to the STEM-EDX analysis, there is a 10-30 nm layer of copper and/or cadmium sulfide segregated at the grain boundaries of this region of sample 3. This segregation of copper and/or cadmium sulfide might happen during the chemical bath deposition of CdS through the pin holes in the absorber layer. In sample 1 the segregation of copper sulfide was only observed at the bottom part of the CZTSe layer. No segregation was observed in sample 4. The composition of 14 individual CZTSe grains of sample 1, 3 and 4 was measured and in sample 1, 3 and 4 the composition is found to be $Cu_{1.98(6)}Zn_{1.17(4)}Sn_{0.90(2)}Se_{3.95(9)}$, $Cu_{2.05(8)}Zn_{1.13(6)}Sn_{0.87(4)}Se_{3.95(10)}$ and $Cu_{2.06(7)}Zn_{1.13(5)}Sn_{0.91(9)}Se_{3.91(7)}$, respectively.

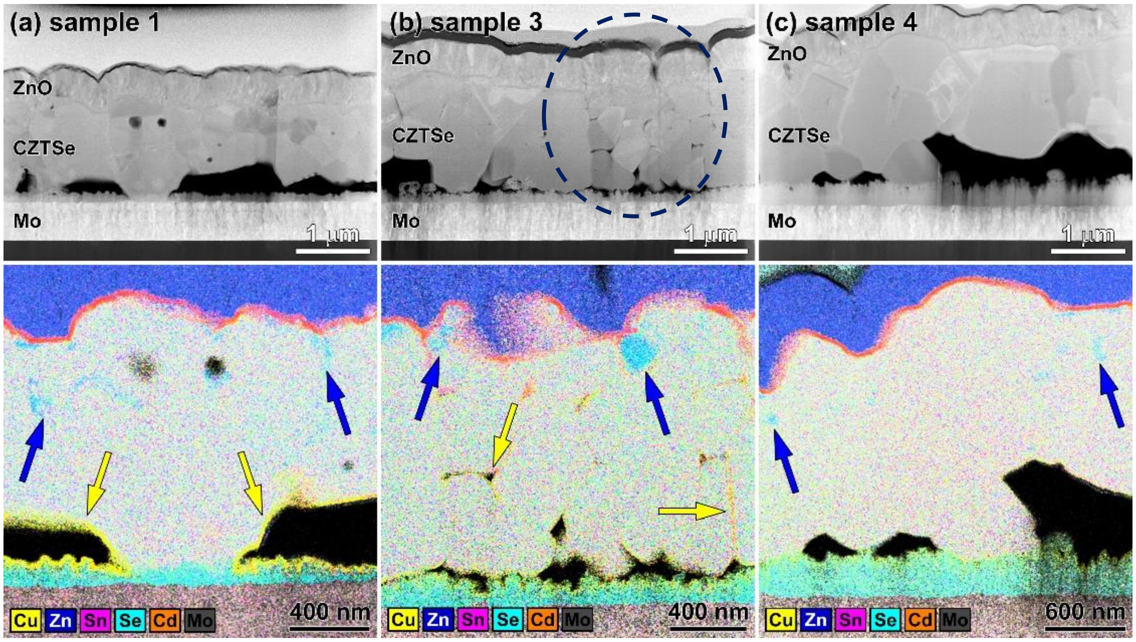

Figure 7-2 Overview HAADF-STEM images of the samples 1 (a), 3 (b) and 4 (c). The corresponding STEM-EDX maps are given at the bottom. The bluish areas inside the CZTSe region correspond to the ZnSe inclusions.

High-resolution TEM and composition profile analysis of these samples were performed at the CZTSe/CdS/ZnO interface. HAADF-STEM images and individual elemental maps of sample 1 with closed TiO_2 and sample 4 (without TiO_2) are shown in **Figure 7-3a** and **b**, respectively. Note that the peaks of Cd-L (3.13 keV) and Sn-L (3.44 keV) are very close giving an unavoidable erroneous presence of Sn in the CdS layer. We performed six EDX maps from different positions of sample 1 and a layer of Ti was found in all measurements, an example is shown in **Figure 7-3a**.

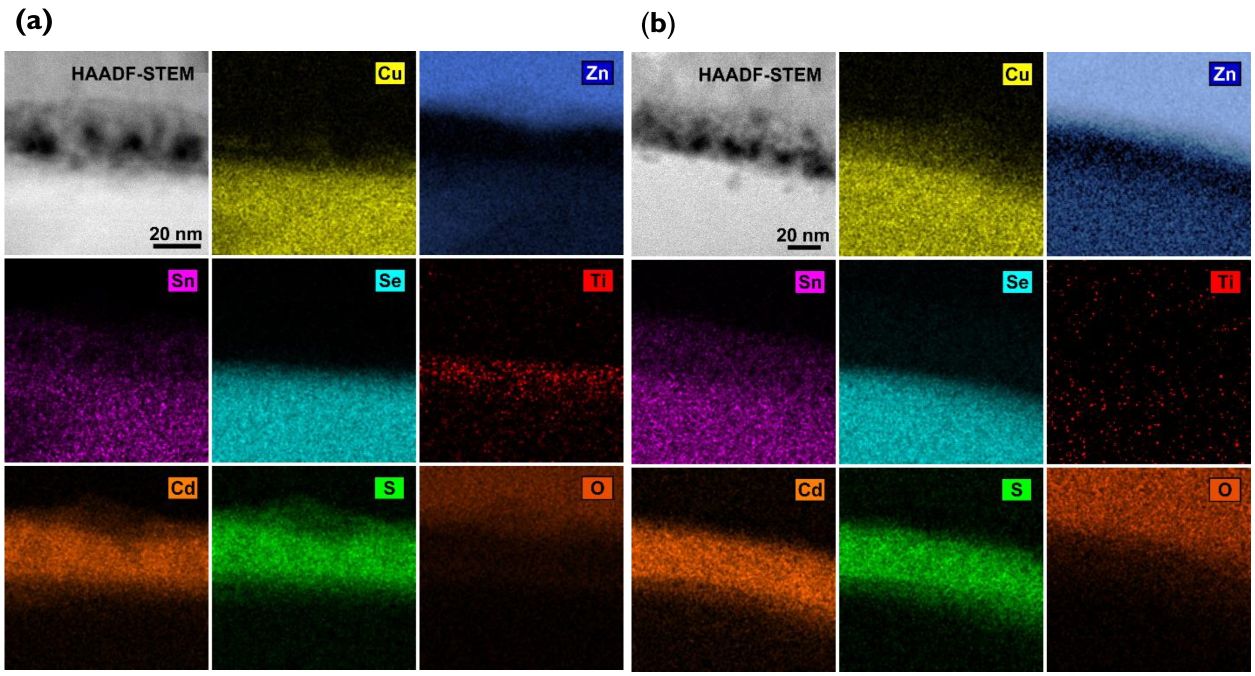

Figure 7-3 Elemental EDX maps of sample 1with closed TiO_2 (a) and sample 4 without TiO_2 (b).

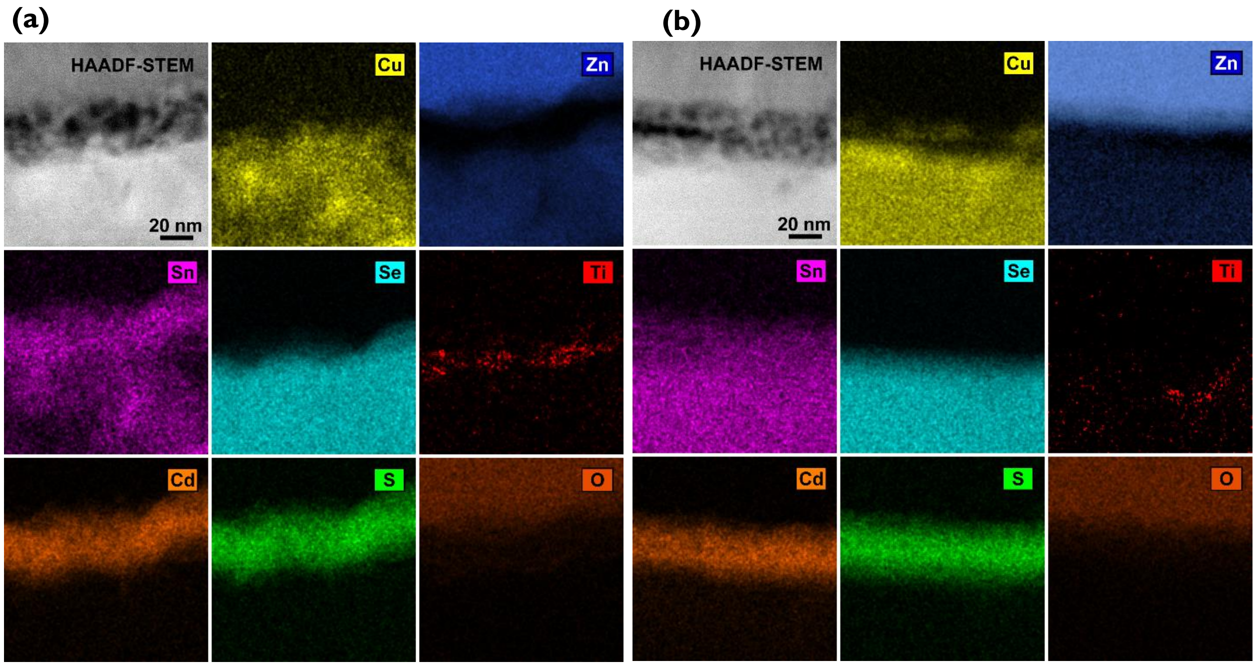

Figure 7-4 Elemental EDX maps of sample 3 with open TiO_2 in two different regions, EDX maps of this sample indicate that Ti containing layer is not continuous.

We also performed six EDX maps of sample 3 with an open TiO_2 layer. A layer of Ti was found in two EDX maps of this sample, one of them is shown in **Figure 7-4 a**. However, in the other four EDX maps of this sample, we couldn't find a continuous layer of Ti, as one shown in **Figure 7-4 b**. Based on these EDX measurements, we conclude that in the open TiO_2 layer there are some openings in certain regions (see **Figure 7-4 b**), while the closed TiO_2 layer is continuous. **Figure 7-5 a** and **b** show the EDX compositional profile of sample 1 with closed TiO_2 layer and sample 3 with an open TiO_2 layer in a region that Ti exists, respectively. As mentioned previously, the peaks of Cd-L (3.13 keV) and Sn-L (3.44 keV) are very close giving an unavoidable presence of Sn in the CdS layer.

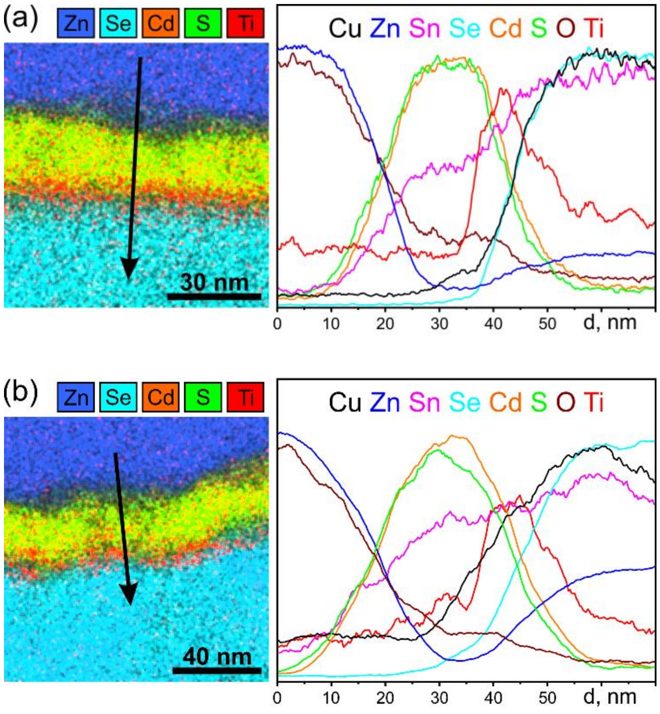

Figure 7-5 Mixed map of elements and the line profile measured perpendicular to the interface for sample 1 with closed TiO_2 (a) and sample 3 with open TiO_2 in a region where Ti exists (b).

Table 7-2 Electrical parameters of the best solar cells in samples 1 (closed TiO_2), 3 (open TiO_2), and 4 (reference).

Sample	**J_{SC} (mA/cm^2)**	**V_{OC} (mV)**	**FF (%)**	**Eff (%)**	**R_{sh} (I) (Ω.cm^2)**	**R_s (I) (Ω.cm^2)**
1- Closed TiO_2	26.2	425	31.7	3.5	141.6	2.6
3- Open TiO_2	32.5	426	50.0	6.9	324.2	1.7
4- Reference	26.6	391	51.9	5.4	335.7	1.9

Figure 7-6a shows the current-voltage (J-V) curves of the champion solar cells of sample 1 (closed TiO_2), sample 3 (open TiO_2) and its reference sample 4. Solar cell parameters of these samples are also summarized in Table 7-2. The J-V curve of the champion solar cell of sample 2 which is the reference of sample 1 is not shown in Figure 7-6 as it was very similar to results of sample 4 (see **Figure 7-7**). It can be observed that V_{OC} is ~ 35 mV higher in solar cells with TiO_2 layers (both open and closed types). However, the J-V curve of the sample with closed TiO_2 has a kink anomaly and FF is very low. This kink behavior might be attributed to a high positive conduction band offset at the absorber/buffer junction. A high positive offset (> 0.4 eV) can be a barrier for the photogenerated electrons, as shown schematically in Figure 7-1a. When the recombination velocity is low in the junction (due to the passivation of defects) and there is a positive offset at the junction, the photogenerated electrons accumulate at the junction. At a high forward bias, the accumulated electrons flow back to the absorber layer and recombine there. On the other hand, when the recombination velocity is high, which is the case in standard CZTSe solar cells, the electrons can recombine at the junction at an intermediate forward voltage [53]. By introducing a KCN etching after deposition of TiO_2 in sample 3 with an open TiO_2 layer, J_{SC} is improved. Moreover, FF is improved to match that value of the reference solar cell. Based on the TEM analysis the improvement of solar cells with open TiO_2 layer can be attributed to the formation of openings that facilitates the charge transport through the open TiO_2 layer. Series resistance (R_s) is slightly higher in samples with the TiO_2 layer. This increased resistance can be attributed to the TiO_2 layer and it is more pronounced in solar cells with a closed TiO_2

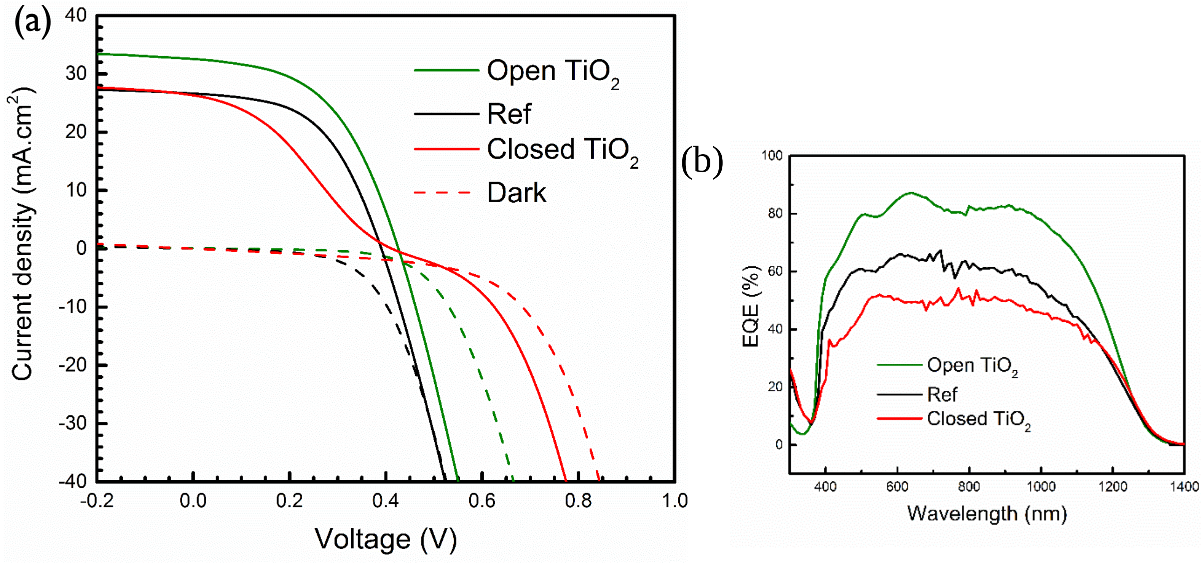

Figure 7-6 Illuminated and dark J-V curves of the champion solar cells with closed/open TiO_2 layers and the reference (a), EQE of the best solar cells with open and closed TiO2 and the reference (b).

layer as compared to the solar cells with an open TiO_2 layer which may have a lower thickness and lateral openings. **Figure 7-6 b** shows the EQE measurements of the champion solar cells of sample 3 with open TiO_2 layer and the reference sample 4 and sample 1 with the closed TiO_2 layer. The EQE measurements confirmed the J_{SC} values measured by J-V measurements and indicate that collection of photo-generated carriers is improved in the whole region of the spectrum. This improvement can be attributed mainly to the passivation of defects at the CZTSe/CdS junction and the reduction of recombination currents. **Figure 7-7** illustrates the solar cell parameters of several samples including sample 1 with closed TiO_2 layer (red boxes), samples 3, 5, 7 and 9 with open TiO_2 layer (green boxes) and their corresponding references 2, 4, 6, 8 and 10 (black boxes). It can be concluded statistically that by introducing a TiO_2 interfacial layer at the junction, V_{OC} improved. J_{SC}, FF, and the conversion efficiency are also statistically higher in solar cells with open TiO_2 layer as compared to their reference solar cells.

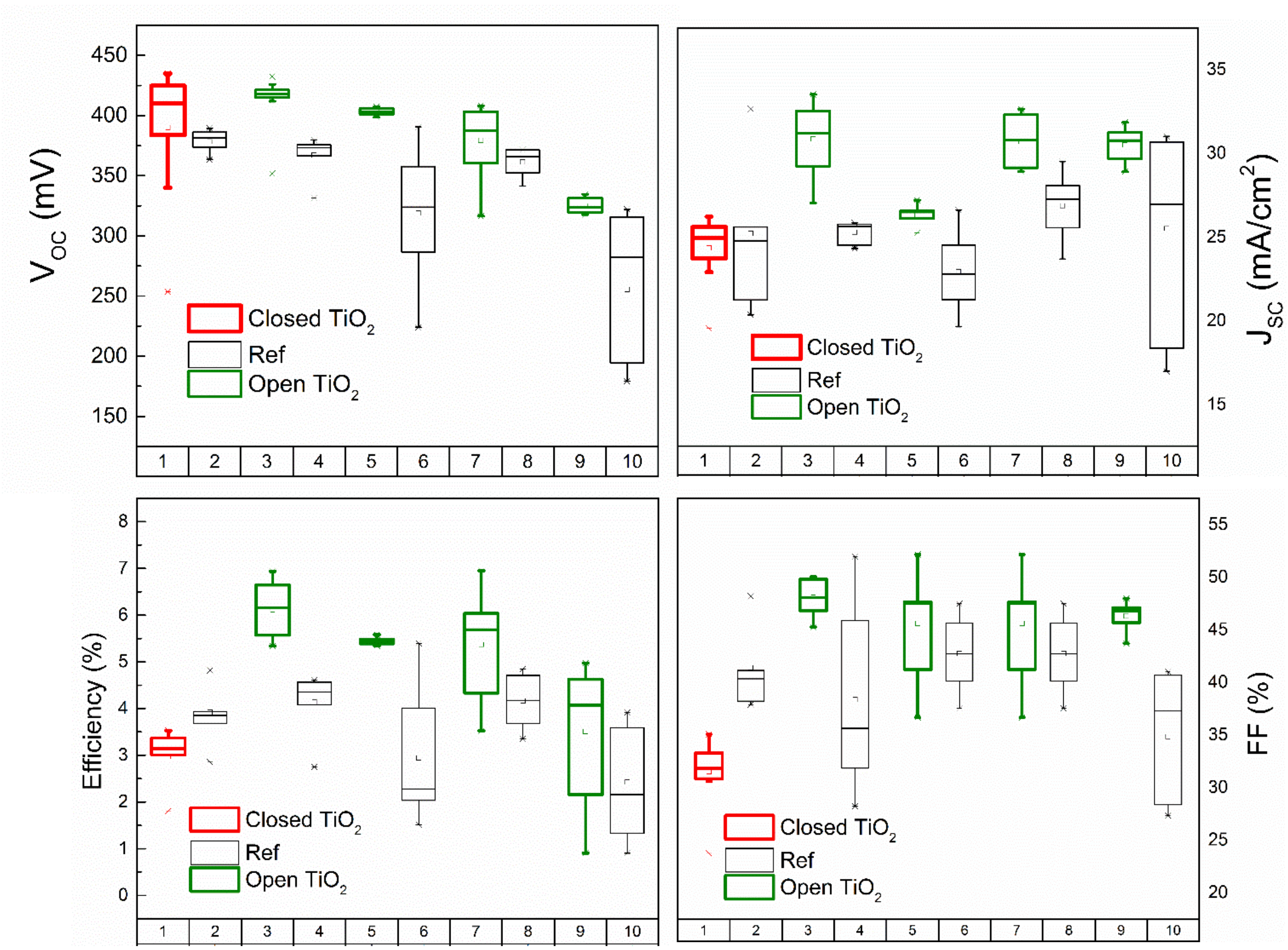

Figure 7-7 Electrical parameters of the samples with closed TiO_2/open TiO_2 layer (red/green boxes) and their references (black boxes). Each box represents values measured from samples containing at least 12 solar cells.

7.3 Conclusion

A few studies already reported on the passivation of kesterite solar cells by introducing ALD coated TiO_2 and Al_2O_3 layers between the kesterite absorber layer and CdS buffer layer. Here, by using a solution processed TiO_2 layer, a significant improvement of V_{OC} was observed, however, a kink anomaly appeared in samples with as deposited TiO_2 layer. This kink anomaly that severely degrades the FF might be attributed to a high barrier at the conduction band. By introducing an additional KCN treatment after spin coating of the TiO_2 layer, the kink anomaly vanished, short circuit current improved and FF also improved to match that of the reference solar cells. EDX mappings of the p-n junction using cross-sectional TEM indicated that in samples with as deposited TiO_2 there is a continuous layer of Ti at the junction while in samples with KCN treatment after deposition of TiO_2, the Ti layer is not continuous and there are openings at the Ti-containing layer. These openings at the TiO_2 interfacial layer can facilitate the charge carrier transport through this layer. Thus in addition to the beneficial effect of the passivation and reduction of recombination currents, the charge transport becomes easier through these openings in the interfacial layer. With a CZTSe/CdS/TiO_2/(KCN treatment)/TCO fabrication process, the best efficiency of 6.9 % was achieved as compared to the CZTSe/CdS/TCO baseline process for which 5.4 % efficiency was achieved.

8 Conclusions and suggestions for future work

In this thesis, we aimed to improve the performance of kesterite solar cells by two main approaches: (i) improvement of the bulk properties of kesterite absorber layer and (ii) modification of solar cell structure by introducing interfacial passivating layers at the back contact and the p-n junction. Improvement of kesterite absorber layer was our main focus in chapter 3, 4 and 5 and in chapter 6 and 7 the modification of solar cell structure was studied.

In chapter 3 we explained about a hybrid sputtering/evaporation technique to deposit binary sulfide precursors on Mo-coated SLG substrates (SLG/Mo/8×(Zn/SnS_2/CuS)). Selenization of binary sulfide precursors with selenium vapor were performed in two types of furnaces (i) a tube furnace (TF) and (ii) a rapid thermal processing system (RTP). The aim of this work was to control the S/Se ratio in CZTSSe films. Morphological, chemical and structural characterization of the absorber layers selenized at different temperatures in TF and RTP were analyzed. It was observed that at temperatures lower than 450 °C, irrespective of the selenization method, the precursor stack does not interdiffuse completely to form a uniform CZTSSe film. At higher temperatures ($\geq$ 450 °C) sulfur was replaced by selenium and a pure selenide CZTSe film was formed. Thus, in order to fabricate CZTSSe absorber layers with good crystalline quality and a controlled amount of S/Se ratio, it's not enough to incorporate sulfur only in the precursors and an annealing process in sulfur and selenium atmosphere is required.

The rest of the work was done in imec-PV lab where a two-step technique was used for fabrication of CZTSe absorber layers including (i) e-beam evaporation of Sn/Zn/Cu precursors on Mo-coated SLG (SLG/Mo/Sn/Zn/Cu) and (ii) selenization of precursors in a rapid thermal processing system using 10 % H_2Se gas in N_2 atmosphere. We prepared CZTSe solar cells with a standard structure of SLG/Mo/CZTSe/CdS/i-ZnO/Al-ZnO.

The thickness of Sn/Zn/Cu precursor was investigated in chapter 4. It was observed that physical properties of the absorber layers strongly depend on the thickness of precursors. Thicker metal starting layers led to a larger Cu to Sn ratio in the final absorbers, possibly because the thinner starting layers show faster interdiffusion of the metals and suppressed $SnSe_2$ evaporation. In addition increasing the thickness improved the morphological quality of CZTSe absorber layers. By increasing the thickness, the distance between the p-n junction and the rear surface was increased, thus the influence of imperfections at the rear surface was reduced. The enhanced physical quality of the absorber layers led to the higher performance of solar cells, especially due to a longer minority carrier lifetime and higher V_{OC}. It was found that the doping density of the absorber layer decreased with increasing the thickness. Lower doping density led to the increasing of the depletion region width and accordingly better collection of the photogenerated carriers and higher J_{SC}. Here, the best performance was achieved for a solar cell with an absorber layer thickness of 1700 nm that showed 406 mV V_{OC}, 36.4 mA/cm^2 J_{SC} and 7.8 % efficiency.

In chapter 5 we studied several processing parameters in order to improve the efficiency and reproducibility of CZTSe solar cells. We investigated the effect of the order of precursors for a large set of samples. It was observed statistically that selenization of the baseline Sn/Zn/Cu precursor and a Zn/Sn/Cu precursor lead to quite similar results concerning the efficiency of final solar cells. In another study, the effect of H_2Se flow rate was studied for a large set of samples. We used three different flow rates of H_2Se including 200, 150 and 80 sccm, in which 2, 1 and 0 pumping steps were required during 15 min selenization. All these 3 selenization recipes led to CZTSe solar cells with efficiencies up to 7 % efficiency. Thus, it can be concluded that the flow rate of H_2Se (or the number of pumping steps during the selenization process) doesn’t have a considerable impact on the performance of final solar cells. Moreover, an irreproducibility was observed in the selenization process. This irreproducibility was decreased by introducing additional cleaning steps and avoiding the contamination sources in selenization process.

In chapter 6, a solution processed MoO_{3-X} was introduced as a promising passivating interfacial layer between Mo rear contact and the CZTSe absorber layer. The effect of this ultra-thin MoO_{3-X} interfacial layer was studied for two types of CZTSe solar cells including solar cells with thin and thick absorber layers. Using this ultra-thin MoO_{3-X}, we aimed to (i) reduce the decomposition reactions at the rear surface (ii) improve the band alignment between CZTSe and Mo rear contact as MoO_{3-X} is a p-type semiconductor with a high work function. By introducing MoO_{3-X} interfacial layer, V_{OC} improved remarkably. J_{SC} and FF did not change considerably by introducing the MoO_{3-X} layer but they improved significantly by increasing the absorber layer thickness. The temperature dependent J-V measurement showed that the band alignment at the rear interface didn't change considerably by adding the MoO_{3-X} layer, but the activation energy of the main recombination path shifted toward higher energies. Top view SEM images of the absorber layers revealed that samples with MoO_{3-X} layer are more uniform. According to these measurements, the main role of MoO_{3-X} layer can be explained as reducing the decomposition reaction between Mo and CZTSe during the selenization process and/or passivation of defects. In this study, the best performance belonged to a thick solar cell with MoO_{3-X} interfacial layer that showed a 413 mV V_{OC}, 32.9 mA/cm^2 J_{SC}, 52.3 % FF and 7.1 % efficiency. While the reference solar cell showed a 384 mV V_{OC}, 32.8 mA/cm^2 J_{SC}, 47 % FF and 5.9 % efficiency.

The aim of chapter 7 was to improve the CZTSe/CdS junction by introducing a solution processed TiO_2 layer. Using, this ultra-thin TiO_2 interfacial layer (~ 3 nm) V_{OC} improved significantly. However, a kink anomaly appeared in the J-V curve of the solar cell with the TiO_2 interfacial layer. By introducing an additional KCN treatment after the spin coating of TiO_2 layer, the kink anomaly vanished, short circuit current improved remarkably and FF also improved to match that of the reference solar cells. EDX mappings of the p-n junction using cross-sectional TEM indicated that the as-deposited TiO_2 layer is continuous while in samples with the TiO_2 layer and additional KCN treatment, the interfacial layer is not continuous and there are lateral openings in the TiO_2 layer. The openings at the TiO_2 interfacial layer formed by the KCN treatment can facilitate the charge carrier transport through this layer. Thus in addition to the passivation of defects by the TiO_2 interfacial layer that led to the reduction of recombination and improvement of V_{OC}, the photo-generated carriers transport through the openings in the TiO_2 layer. Here, the best performance belonged to a solar cell with the TiO_2 interfacial and the additional KCN treatment that showed a 426 mV V_{OC}, 32.5 mA/cm^2 J_{SC}, 50.0 % FF, and 6.9 % efficiency. While the reference solar cell showed a 391 mV V_{OC}, 26.6 mA/cm^2 J_{SC}, 51.9 % FF and 5.4 % efficiency.

Comparing the results of chapters 4 to 6 it may be concluded that the best efficiency of 7.8 % was achieved for a standard Mo/CZTSe/CdS/i-ZnO/Al-ZnO structure. Bearing in mind the irreproducibility of the fabrication process, one can only compare solar cells prepared in the same processing run. Solar cells processed in different fabrication runs may be affected by the irreproducibility of each processing step including the fabrication of absorber layers, CdS buffer layer deposition, and i-ZnO/Al-ZnO deposition. Moreover, we showed statistically for several samples in this study that modification of CZTSe solar cell structure with appropriate passivating layers at the rear interface and p-n junction led to a significant improvement of V_{OC} and the performance as compared to their reference solar cells.

8.1 Suggestions for future work

The highest world record efficiencies for kesterite solar cells belong to a CZTSSe solar cell prepared by hydrazine solution-based technique (12.6 %) [50] and a pure CZTSe solar cell prepared by a co-evaporation technique (11.6 %) [47]. In this study, we achieved up to 7.8 % efficiency for pure selenide CZTSe solar cells prepared by selenization of e-beam evaporated Sn/Zn/Cu precursors. Although several studies showed CZTSSe absorber layers with Zn-rich and Cu-poor composition leads to higher efficiencies, here the composition of the best CZTSe absorbers was measured to be Cu/(Zn+Sn) ~ 0.8 and Zn/Sn ~ 1. A systematic study of the metallic ratios of the precursors is suggested for the further improvement of the composition of CZTSe absorber layers.

To improve the CZTSe absorber layer, one suggestion is to incorporate a thin layer of Ge in the precursors. We already tried selenization of Ge(30)/Sn(280)/Zn(150)/Cu(160) precursors in the RTP system which led to CZTSe absorber layers with big grain and good crystalline quality. Solar cells prepared by selenization of this Ge-containing precursors showed up to 6 % efficiencies. However, so far we selenized the Ge-containing samples in an upside down configuration. In the upside down configuration, samples are placed upside down on a graphite susceptor in which 4 holes are embedded for the 5×5 cm^2 substrates. The reason of upside down selenization is to avoid the contamination of quartz window as $GeSe_2$ evaporate from the surface of samples and it sticks to the quartz window. However, the $GeSe_2$ can be easily wiped off the stainless steel after the upside down selenization. So far, the highest efficiency achieved by this configuration was ~ 4 % for the standard Mo/Sn/Zn/Cu precursors and ~ 6 % for Mo/Ge/Sn/Zn/Cu precursors. Optimizing the upside down selenization may improve these efficiencies. We also suggest a systematic optimization of the thickness, metallic ratios and order of elements of the Ge-containing precursors.

We believe the standard selenization process using H_2Se gas in the RTP system is almost optimized. For future work, selenization using Se vapor instead of H_2Se gas is suggested. Several groups reported good results for kesterite absorber layers prepared by selenization using Se vapor in tube furnaces or hot plates. We had already achieved up to 3 % efficiency for pure CZTSe solar cells prepared by selenization of e-beam precursors in a tube furnace and it can be improved by further optimization of the selenization conditions such as time, temperature, etc. These CZTSe films selenized in the tube furnace are usually very compact and they have very good crystalline quality and big grains. The main problem of these samples is a thick layer of $MoSe_2$ which leads to a high series resistance in CZTSe solar cells. In order to decrease the thickness of $MoSe_2$ layer in theses samples, it is suggested to use appropriate interfacial layers such as MoO_{3-X}, TiN, etc. between Mo and CZTSe.

As shown in chapter 6, quality of the rear surface is a big challenge in kesterite solar cells. The imperfections such as voids and secondary phases at the rear surface not only increase the interface recombination but also they affect the film growth and bulk properties of the absorber layer. We observed by introducing MoO_{3-X} interfacial layer the performance of solar cells improves mainly due to the improvement of V_{OC}. A systematic study about optimizing the MoO_{3-X} interfacial layer for the rear surface application in kesterite solar cells is suggested.

In chapter 7 we showed by introducing an ultra-thin layer of TiO_2 at the p-n junction the performance of kesterite solar cells improved. This ultra-thin layer was prepared by spin coating of TiO_2 followed by a KCN treatment. Solar cells with this TiO_2 interfacial layer and without KCN treatment had a kink anomaly in their J-V curve that could be explained by a large positive conduction band offset at the CZTSe/TiO_2/CdS interface. We suggest optimizing the recipe of TiO_2 layer in order to improve the electrical properties of the TiO_2 interfacial layer for this application and avoiding the additional KCN treatment.

References:

[1] http://www.eia.gov, (n.d.).

[2] M.A. Green, K. Emery, Y. Hishikawa, W. Warta, E.D. Dunlop, D.H. Levi, A.W.Y. Ho-Baillie, Solar cell efficiency tables (version 49), Prog. Photovoltaics Res. Appl. 25 (2017) 3–13. doi:10.1002/pip.2855.

[3] D. Bauer, D. Diamond, J. Li, D. Sandalow, P. Telleen, B. Wanner, US Department of Energy: Critical Materiasl Strategy, December 2010, Agenda. (2010) 1–166. doi:10.2172/1000846.

[4] European Commission, No Title, Crit. Raw Mater. EU. (2010).

[5] T. Shibuya, Y. Goto, Y. Kamihara, M. Matoba, K. Yasuoka, L.A. Burton, A. Walsh, From kesterite to stannite photovoltaics: Stability and band gaps of the $Cu_2(Zn,Fe)SnS_4$ alloy, Appl. Phys. Lett. 104 (2014) 3–6. doi:10.1063/1.4862030.

[6] P.M.P. Salomé, P.A. Fernandes, J.P. Leitão, M.G. Sousa, J.P. Teixeira, A.F. Da Cunha, Secondary crystalline phases identification in $Cu_2ZnSnSe_4$ thin films: Contributions from Raman scattering and photoluminescence, J. Mater. Sci. 49 (2014) 7425–7436. doi:10.1007/s10853-014-8446-2.

[7] S. Schorr, H.-J. Hoebler, M. Tovar, A neutron diffraction study of the stannite-kesterite solid solution series, Eur. J. Mineral. 19 (2007) 65–73. doi:10.1127/0935-1221/2007/0019-0065.

[8] S. Schorr, The crystal structure of kesterite type compounds: A neutron and X-ray diffraction study, Sol. Energy Mater. Sol. Cells. 95 (2011) 1482–1488. doi:10.1016/j.solmat.2011.01.002.

[9] J.M. Raulot, C. Domain, J.F. Guillemoles, Ab initio investigation of potential indium and gallium free chalcopyrite compounds for photovoltaic application, J. Phys. Chem. Solids. 66 (2005) 2019–2023. doi:10.1016/j.jpcs.2005.09.097.

[10] P.M.P. Salomé, P.A. Fernandes, A.F. Da Cunha, Influence of selenization pressure on the growth of $Cu_2ZnSnSe_4$ films from stacked metallic layers, Phys. Status Solidi Curr. Top. Solid State Phys. 7 (2010) 913–916. doi:10.1002/pssc.200982748.

[11] P.A. Fernandes, P.M.P. Salomé, A.F. Da Cunha, Study of polycrystalline Cu$_2$ZnSnS$_4$ films by Raman scattering, J. Alloys Compd. 509 (2011) 7600–7606. doi:10.1016/j.jallcom.2011.04.097.

[12] P.M.P. Salomé, J. Malaquias, P.A. Fernandes, M.S. Ferreira, A.F. da Cunha, J.P. Leitão, J.C. González, F.M. Matinaga, Growth and characterization of Cu$_2$ZnSn(S,Se)$_4$ thin films for solar cells, Sol. Energy Mater. Sol. Cells. 101 (2012) 147–153. doi:10.1016/j.solmat.2012.02.031.

[13] S. Ranjbar, M.R. Rajesh Menon, P.A. Fernandes, A.F. Da Cunha, Effect of selenization conditions on the growth and properties of Cu$_2$ZnSn(S,Se)$_4$ thin films, Thin Solid Films. 582 (2015) 188–192. doi:10.1016/j.tsf.2014.11.044.

[14] A.D. Collord, H.W. Hillhouse, Germanium Alloyed Kesterite Solar Cells with Low Voltage De ficits, Chem. Mater. 28 (2016) 2067–2073. doi:10.1021/acs.chemmater.5b04806.

[15] H. Elanzeery, M. Buffière, K. Ben Messaoud, S. Oueslati, G. Brammertz, O. El Daif, D. Cheyns, R. Guindi, M. Meuris, J. Poortmans, Multistep deposition of Cu$_2$Si(S,Se)$_3$ and Cu$_2$ZnSiSe$_4$ high band gap absorber materials for thin film solar cells, Phys. Status Solidi - Rapid Res. Lett. 9 (2015) 338–343. doi:10.1002/pssr.201510125.

[16] G. Brramertz, B. Vermang, H. El Anzeery, S. Sahayaraj, S. Ranjbar, M. Meuris, J. Poortmans, Fabrication and characterization of ternary Cu$_8$SiS$_6$ and Cu$_8$SiSe$_6$ thin film layers for optoelectronic applications, Thin Solid Films. 616 (2016) 649–654.

[17] G. Brramertz, B. Vermang, H. El Anzeery, S. Sahayaraj, S. Ranjbar, M. Meuris, J. Poortmans, Fabrication of ternary and quaternary chalcogenide compounds based on Cu, Zn, Sn and Si for thin film photovoltaic applications, Phys. Status Solidi Curr. Top. Solid State Phys. (2017). doi:10.1002/pssc.201600162.

[18] T. Gershon, Y.S. Lee, P. Antunez, R. Mankad, S. Singh, D. Bishop, O. Gunawan, M. Hopstaken, R. Haight, Photovoltaic Materials and Devices Based on the Alloyed Kesterite Absorber (Ag$_x$Cu$_{1 - x}$) 2ZnSnSe $_4$, Adv. Energy Mater. 6 (2016) 1–7. doi:10.1002/aenm.201502468.

[19] S. Delbos, Kësterite thin films for photovoltaics : a review, EPJ Photovoltaics. 3 (2012) 35004. doi:10.1051/epjpv/2012008.

[20] M. Kumar, A. Dubey, N. Adhikari, S. Venkatesan, Q. Qiao, Strategic review of secondary phases, defects and defect-complexes in kesterite CZTS–Se solar cells, Energy Environ. Sci. 8 (2015) 3134–3159. doi:10.1039/C5EE02153G.

[21] S. Chen, J.H. Yang, X.G. Gong, A. Walsh, S.H. Wei, Intrinsic point defects and complexes in the quaternary kesterite semiconductor Cu_2ZnSnS_4, Phys. Rev. B - Condens. Matter Mater. Phys. 81 (2010) 35–37.

[22] T. Gershon, T. Gokmen, O. Gunawan, R. Haight, S. Guha, I.B.M. Tj, Understanding the relationship between $Cu_2ZnSn(S,Se)_4$ material properties and device performance, 4 (2014) 159–170. doi:10.1557/mrc.2014.34.

[23] G. Brammertz, Y. Ren, M. Buffière, S. Mertens, J. Hendrick, H. Marko, A.E. Zaghi, N. Lenaers, C. Köble, J. Vleugels, M. Meuris, J. Poortmans, Electrical characterization of $Cu_2ZnSnSe_4$ solar cells from selenization of sputtered metal layers, Thin Solid Films. 535 (2013) 348–352. doi:10.1016/j.tsf.2012.10.037.

[24] A. Nagaoka, H. Miyake, T. Taniyama, K. Kakimoto, K. Yoshino, Correlation between intrinsic defects and electrical properties in the high-quality Cu_2ZnSnS_4 single crystal, Appl. Phys. Lett. 103 (2013). doi:10.1063/1.4821279.

[25] S. Ranjbar, G. Brammertz, B. Vermang, A. Hadipour, A. Mule, M. Meuris, A.F. Cunha, J. Poortmans, Effect of Sn/Zn/Cu precursor stack thickness on two-step processed kesterite solar cells, Thin Solid Films. (2016). doi:10.1016/j.tsf.2016.09.040.

[26] F. Hergert, R. Hock, Predicted formation reactions for the solid-state syntheses of the semiconductor materials Cu_2SnX_3 and Cu_2ZnSnX_4 (X = S,Se) starting from binary chalcogenides, Thin Solid Films. 515 (2007) 5953–5956. doi:10.1016/j.tsf.2006.12.096.

[27] R. Schurr, A. Hölzing, S. Jost, R. Hock, T. Voβ, J. Schulze, A. Kirbs, A. Ennaoui, M. Lux-Steiner, A. Weber, I. Kötschau, H.W. Schock, The crystallisation of Cu_2ZnSnS_4 thin film solar cell absorbers from co-electroplated Cu-Zn-Sn precursors, Thin Solid Films. 517 (2009) 2465–2468. doi:10.1016/j.tsf.2008.11.019.

[28] I.D. Olekseyuk, I. V. Dudchak, L. V. Piskach, Phase equilibria in the Cu_2S-ZnS-SnS_2 system, J. Alloys Compd. 368 (2004) 135–143. doi:10.1016/j.jallcom.2003.08.084.

[29] H. Katagiri, Cu_2ZnSnS_4 thin film solar cells, Thin Solid Films. 480–481 (2005) 426–432. doi:10.1016/j.tsf.2004.11.024.

[30] A. Fairbrother, M. Dimitrievska, Y. Sánchez, V. Izquierdo-Roca, A. Pérez-Rodríguez, E. Saucedo, Compositional paradigms in multinary compound systems for photovoltaic applications: a case study of kesterites, J. Mater. Chem. A. 3 (2015) 9451–9455. doi:10.1039/C5TA02000J.

[31] J.J. Scragg, J.T. Watjen, M. Edoff, T. Ericson, T. Kubart, C. Platzer-Björkman, A Detrimental Reaction at the Molybdenum Back Contact in $Cu_2ZnSn(S,Se)_4$ Thin-Film Solar Cells, J. Am. Chem. Soc. 134 (2012) 19330–19333. doi:10.1021/ja308862n.

[32] J.J. Scragg, T. Kubart, J.T. Wätjen, T. Ericson, M.K. Linnarsson, C. Platzer-Björkman, Effects of back contact instability on Cu_2ZnSnS_4 devices and processes, Chem. Mater. 25 (2013) 3162–3171.

[33] S. López-marino, The Importance of Back Contact Modification in Cu2ZnSnSe4 Solar Cells : the Role of a Thin MoO_2 Layer, Chem. Mater. 2016, 28,. 28 (2016) 2067−2073. doi:10.1016/j.nanoen.2016.06.034.

[34] F. Liu, K. Sun, W. Li, C. Yan, H. Cui, L. Jiang, X. Hao, A. Martin, Enhancing the Cu_2ZnSnS_4 solar cell efficiency by back contact modification : Inserting a thin TiB_2 intermediate layer at Cu2ZnSnS4 / Mo interface, Appl. Phys. Lett. 104 (2015) 6–11. doi:10.1063/1.4863736.

[35] S. Oueslati, G. Brammertz, M. Buffière, H. ElAnzeery, D. Mangin, O. ElDaif, O. Touayar, C. Köble, M. Meuris, J. Poortmans, Study of alternative back contacts for thin film $Cu_2ZnSnSe_4$-based solar cells, J. Phys. D. Appl. Phys. 48 (2015) 35103. doi:10.1088/0022-3727/48/3/035103.

[36] S. Lopez-Marino, M. Placidi, P.T. Amador, J. Llobet, V. Izquierdo-Roca, X. Fontane, A. Fairbrother, M. Rodriguez, D. Sylla, A. Perez-Rodriguez, E. Saucedo, Inhibiting the absorber/Mo-back contact decomposition reaction in $Cu_2ZnSnSe_4$ solar cells: the role of a ZnO

intermediate nanolayer, J. Mater. Chem. A. 1 (2013) 8338–8343. doi:10.1039/c3ta11419h.

[37] H. Cui, X. Liu, F. Liu, X. Hao, N. Song, C. Yan, H. Cui, X. Liu, F. Liu, X. Hao, N. Song, C. Yan, Boosting Cu_2ZnSnS_4 solar cells efficiency by a thin Ag intermediate layer between absorber and back contact Boosting Cu_2ZnSnS_4 solar cells efficiency by a thin Ag intermediate layer between absorber and back contact, Appl. Phys. Lett. 104 (2014) 11–15.

[38] S. Ranjbar, G. Brammertz, B. Vermang, A. Hadipour, S. Cong, K. Suganuma, T. Schnabel, M. Meuris, A. F. da Cunha, and J. Poortmans, Improvement of kesterite solar cell performance by solution synthesized MoO_3 interfacial layer, Phys. Status Solidi A. 6 (2016) 1–6. doi:10.1002/pssa.201600534.

[39] A. Weber, R. Mainz, H.W. Schock, On the Sn loss from thin films of the material system Cu-Zn-Sn-S in high vacuum, J. Appl. Phys. 107 (2010) 013516–013521. doi:10.1063/1.3273495.

[40] K. Ito, T. Nakazawa, Electrical and Optical Properties of Stannite-Type Quaternary Semiconductor Thin Films, Jpn. J. Appl. Phys. 27 (1988) 2094–2097.

[41] H. Katagiri, N. Sasaguchi, S. Hando, S. Hoshino, J. Ohashi, T. Yokota, Preparation and Evaluation of CuZnSnS Thin Films by Sulfurization of E-B Evaporated Precursors, Sol. Energy Mater. Sol. Cells. 49 (1997) 407–414.

[42] H. Katagiri, K. Jimbo, W.S. Maw, K. Oishi, M. Yamazaki, H. Araki, A. Takeuchi, Development of CZTS-based thin film solar cells, Thin Solid Films. 517 (2009) 2455–2460. doi:10.1016/j.tsf.2008.11.002.

[43] K. Moriya, K. Tanaka, H. Uchiki, Cu2ZnSnS4 Thin Films Annealed in H_2S Atmosphere for Solar Cell Absorber Prepared by Pulsed Laser Deposition, Jpn. J. Appl. Phys. 47 (2008) 602–604. doi:10.1143/JJAP.47.602.

[44] S.A. Vanalakar, G.L. Agawane, S.W. Shin, M.P. Suryawanshi, K. V. Gurav, K. S. Jeon, P.S. Patil, C.W. Jeong, J.Y. Kim, J.H. Kim, A review on pulsed laser deposited CZTS thin films for solar cell applications, J. Alloys Compd. 619 (2015) 109–121. doi:10.1016/j.jallcom.2014.09.018.

[45] K. Sun, C. Yan, F. Liu, J. Huang, F. Zhou, J.A. Stride, M. Green, X. Hao, Over 9% Efficient Kesterite Cu2ZnSnS4 Solar Cell Fabricated by Using $Zn_{1-x}Cd_xS$ Buffer Layer, Adv. Energy Mater. 6 (2016). doi:10.1002/aenm.201600046.

[46] G. Brammertz, M. Buffière, S. Oueslati, H.Elanzeery, K. Ben Messaoud, S. Sahayaraj, C. Köble, M. Meuris, J. Poortmans, Characterization of defects in 9.7% efficient $Cu_2ZnSnSe_4$-CdS-ZnO solar cells, Appl. Phys. Lett. 103 (2013). doi:10.1063/1.4826448.

[47] Y.S. Lee, T. Gershon, O. Gunawan, T.K. Todorov, T. Gokmen, $Cu_2ZnSnSe_4$ Thin-Film Solar Cells by Thermal Co-evaporation with 11.6 % Efficiency and Improved Minority Carrier Diffusion Length, Adv. Energy Mater. 5 (2014) 1401372–1401377. doi:10.1002/aenm.201401372.

[48] K. Woo, Y. Kim, W. Yang, K. Kim, I. Kim, Y. Oh, J.Y. Kim, J. Moon, Band-gap-graded $Cu_2ZnSn(S_{1-x},Se_{(x)})_4$ solar cells fabricated by an ethanol-based, particulate precursor ink route., Sci. Rep. 3 (2013) 3069. doi:10.1038/srep03069.

[49] J. Kim, H. Hiroi, T.K. Todorov, O. Gunawan, M. Kuwahara, T. Gokmen, D. Nair, M. Hopstaken, B. Shin, Y.S. Lee, W. Wang, H. Sugimoto, D.B. Mitzi, High Efficiency $Cu_2ZnSn(S,Se)_4$ Solar Cells by Applying a Double In_2S_3/CdS Emitter, Adv. Mater. 26 (2014) 7427–7431. doi:10.1002/adma.201402373.

[50] W. Wang, M.T. Winkler, O. Gunawan, T. Gokmen, T.K. Todorov, Y. Zhu, D.B. Mitzi, Device characteristics of CZTSSe thin-film solar cells with 12.6% efficiency, Adv. Energy Mater. 4 (2014) 1–5. doi:10.1002/aenm.201301465.

[51] B. Shin, Y. Zhu, N.A. Bojarczuk, S.J. Chey, S. Guha, B. Shin, Y. Zhu, N.A. Bojarczuk, S.J. Chey, S. Guha, Control of an interfacial $MoSe_2$ layer in $Cu_2ZnSnSe_4$ thin film solar cells: 8.9 power conversion efficiency with a TiN diffusion barrier, Appl. Phys. Lett. 101 (2012) 053903–053906. doi:10.1063/1.4740276.

[52] S. Adachi, Earth-Abundant Materials for Solar Cells: Cu2-II-IV-VI4 Semiconductors, (n.d.).

[53] R. Scheer, H. Schock, T.F. Devices, Chalcogenide Photovoltaics, n.d.

[54] J.-S. Kim, J.-K. Kang, D.-K. Hwang, High efficiency bifacial $Cu_2ZnSnSe_4$ thin-film solar cells on transparent conducting oxide glass substrates, APL Mater. 4 (2016) 096101–096106. doi:10.1063/1.4962145.

[55] B. Vermang, Y. Ren, Donzel-Gargand, O. Frisk, C. Joel, Jonathan Scragg, P. Salome, J. Borme, S. Sadewasser, C. Platzer-Bjorkman, and M. Edoff, Rear Surface Optimization of CZTS Solar Cells by Use of a Passivation Layer With Nanosized Point Openings, IEEE J. Photovoltaics. 6 (2015) 332–336. doi:10.1109/JPHOTOV.2015.2496864.

[56] C. Platzer-Björkman, C. Frisk, J.K. Larsen, T. Ericson, S.Y. Li, J.J.S. Scragg, J. Keller, F. Larsson, and T. Törndahl, Reduced interface recombination in Cu_2ZnSnS_4 solar cells with atomic layer deposition $Zn_{1-x}Sn_xO_y$ buffer layers, 107 (2015) 243904–243907. doi:10.1063/1.4937998.

[57] M. Nguyen, K. Ernits, K.F. Tai, C.F. Ng, S.S. Pramana, W.A. Sasangka, S.K. Batabyal, T. Holopainen, D. Meissner, A. Neisser, L. H.Wong, ZnS buffer layer for $Cu_2ZnSn(SSe)_4$ monograin layer solar cell, Sol. Energy. 111 (2015) 344–349. doi:10.1016/j.solener.2014.11.006.

[58] T. Minemoto, T. Matsui, H. Takakura, Y. Hamakawa, T. Negami, Y. Hashimoto, T. Uenoyama, M. Kitagawa, Theoretical analysis of the effect of conduction band offset of window/CIS layers on performance of CIS solar cells using device simulation, Sol. Energy Mater. Sol. Cells. 67 (2001) 83–88. doi:10.1016/S0927-0248(00)00266-X.

[59] X. Liu, Y. Feng, H. Cui, F. Liu, X. Hao, G. Conibeer, D.B. Mitzi, M. Green, The current status and future prospects of kesterite solar cells: a brief review, Prog. Photovolt Res. Appl. 24 (2016) 659–676. doi:10.1002/pip.

[60] W. Wu, Y. Cao, J.V. Caspar, Q. Guo, L.K. Johnson, R.S. Mclean, I. Malajovich, K.R. Choudhury, Characterization of CZTSSe photovoltaic device with an atomic layer-deposited passivation layer, Appl. Phys. Lett. 105 (2014) 042108–042111. doi:10.1063/1.4891852.

[61] M.E. Erkan, V. Chawla, M.A. Scarpulla, Reduced defect density at the CZTSSe/CdS interface by atomic layer deposition of Al_2O_3, J. Appl. Phys. 119 (2016) 194504–194511. doi:10.1063/1.4948947.

[62] Y.S. Lee, T. Gershon, T.K. Todorov, W. Wang, M.T. Winkler, M. Hopstaken, O. Gunawan, J. Kim, Atomic Layer Deposited Aluminum Oxide for Interface Passivation of $Cu_2ZnSn(S,Se)_4$ Thin-Film Solar Cells, Adv. Energy Mater. 6 (2016) 1–5. doi:10.1002/aenm.201600198.

[63] T. Gokmen, O. Gunawan, T.K. Todorov, D.B. Mitzi, T. Gokmen, O. Gunawan, T.K. Todorov, D.B. Mitzi, Band tailing and efficiency limitation in kesterite solar cells, Appl. Phys. Lett. 103 (2013) 103506–6. doi:10.1063/1.4820250.

[64] B.G. Mendis, M.D. Shannon, M.C.J. Goodman, J.D. Major, A.A. Taylor, D P Halliday, The nature of electrostatic potential fluctuations in Cu_2ZnSnS_4 and their role on photovoltaic device performance, J. Phys. Conf. Ser. 471 (2013) 6–10. doi:10.1088/1742-6596/471/1/012014.

[65] J.J.S. Scragg, J.K. Larsen, M. Kumar, C. Persson, J. Sendler, S. Siebentritt, Cu–Zn disorder and band gap fluctuations in $Cu_2ZnSn(S, Se)_4$: Theoretical and experimental investigations., Phys. Status Solidi B. 253 (2016) 247–254. doi:doi:10.1002/pssb.201552530.

[66] G. Altamura, J. Vidal, Impact of Minor Phases on the Performances of CZTSSe Thin-Film Solar Cells, Chem. Mater. 28 (2016) 3540−3563. doi:10.1021/acs.chemmater.6b00069.

[67] J. Just, D. Lutzenkirchen-Hecht, R. Frahm, S. Schorr, T. Unold, Determination of secondary phases in kesterite Cu_2ZnSnS_4 thin films by X-ray absorption near edge structure analysis, Appl. Phys. Lett. 99 (2011). doi:10.1063/1.3671994.

[68] W. Yin, Y. Wu, S. Wei, R. Noufi, M.M. Al-jassim, Engineering grain boundaries in $Cu_2ZnSnSe_4$ for better cell performance: A first-principle study, Adv. Energy Mater. 4 (2014). doi:10.1002/aenm.201300712.

[69] G. Brammertz, S. Oueslati, M. Buffière, J. Bekaert, H. El Anzeery, K. Ben Messaoud, S. Sahayaraj, T. Nuytten, C. Köble, M. Meuris, J. Poortmans, Investigation of properties limiting efficiency in $Cu_2ZnSnSe_4$-based solar cells, IEEE J. Photovoltaics. 5 (2015) 649–655. doi:10.1109/JPHOTOV.2014.2376053.

[70] M. Buffière, G. Brammertz, S. Sahayaraj, M. Batuk, S. Khelifi, D. Mangin, A.A. El Mel, L. Arzel, J. Hadermann, M. Meuris, KCN Chemical Etch for Interface Engineering in $Cu_2ZnSnSe_4$ Solar

Cells, ACS Appl. Mater. Interfaces. 7 (2015) 14690–14698. doi:10.1021/acsami.5b02122.

[71] S. Sahayaraj, G. Brramertz, B. Vermang, S. Ranjbar, M. Meuris, J. Vleugels, J. Poortmans, Effect of the duration of a wet KCN etching step and post deposition annealing on the efficiency of $Cu_2ZnSnSe_4$ solar cells, Thin Solid Films. (2016). doi:10.1016/j.tsf.2016.09.055.

[72] M. Buffière, G. Brammertz, A.-A. El Mel, N. Barreau, M. Meuris, J. Poortmans, Effect of ammonium sulfide treatments on the surface properties of $Cu_2ZnSnSe_4$ thin films, Thin Solid Films. (2016) 9–14. doi:10.1016/j.tsf.2016.09.011.

[73] K. Ben Messaoud, M. Buffière, G. Brammertz, H. Elanzeery, S. Oueslati, J. Hamon, B.J. Kniknie, M. Meuris, M. Amlouk, J. Poortmans, Impact of the Cd^{2+} treatment on the electrical properties of $Cu_2ZnSnSe_4$ and Cu(In,Ga)Se_2 solar cells, Prog. Photovolt Res. Appl. 23 (2015) 1660–1667. doi:10.1002/pip.

[74] M. Neuschitzer, Y. Sanchez, S. Lopez-Marino, H. Xie, A. Fairbrother, M. Placidi, S. Haass, V. Izquierdo-Roca, A. Perez-Rodriguez, E. Saucedo, Optimization of CdS buffer layer for high-performance $Cu_2ZnSnSe_4$ solar cells and the effects of light soaking: Elimination of crossover and red kink, Prog. Photovoltaics Res. Appl. 23 (2015) 1660–1667. doi:10.1002/pip.2589.

[75] J. George, Preparation of Thin Films, 1992.

[76] P.M.P. Salomé, J. Malaquias, P.A. Fernandes, A.F. Da Cunha, Mo bilayer for thin film photovoltaics revisited, J. Phys. D Appl. Phys. 43 (2010) 345501–7. doi:10.1088/0022-3727/43/34/345501.

[77] S.S. Hegedus, W.N. Shafarman, Thin-Film Solar Cells: Device Measurements and Analysis, Prog. Photovoltaics Res. Appl. 12 (2004) 155–176. doi:10.1002/pip.518.

[78] D. Abou-Ras, T. Kirchartz, U. Rau, Advanced Characterization Techniques for Thin Film Solar Cells, Wiley-VCH, 2011.

[79] W.K. Metzger, R.K. Ahrenkiel, P. Dippo, J. Geisz, M.W. Wanlass, S. Kurtz, Time-Resolved Photoluminescence and Photovoltaics, (2005).

[80] A. Kanevce, D.H. Levi, D. Kuciauskas, The role of drift, diffusion, and recombination in time-resolved photoluminescence of CdTe solar cells determined through numerical simulation, Prog. Photovoltaics Res. Appl. 22 (2014) 1138–1146. doi:10.1002/pip.2369.

[81] J.P. Teixeira, R.A. Sousa, M.G. Sousa, A.F. Cunha, P.A. Fernandes, P.M.P. Salomé, J.C. González, J.P. Teixeira, R.A. Sousa, M.G. Sousa, A.F. Cunha, P.A. Fernandes, Comparison of fluctuating potentials and donor-acceptor pair transitions in a Cu-poor Cu_2ZnSnS_4 based solar cell, Appl. Phys. Lett. 105 (2014) 163901–163904. doi:10.1063/1.4899057.

[82] S. Oueslati, G. Brammertz, M. Buffière, C. Köble, T. Oualid, M. Meuris, J. Poortmans, Photoluminescence study and observation of unusual optical transitions in $Cu_2ZnSnSe_4$/CdS/ZnO solar cells, Sol. Energy Mater. Sol. Cells. 134 (2015) 340–345. doi:http://dx.doi.org/10.1016/j.solmat.2014.10.041.

[83] K. Muska, M. Kauk-Kuusik, M. Grossberg, M. Altosaar, M. Pilvet, T. Varema, K. Timmo, O. Volobujeva, A. Mere, Impact of Cu2ZnSn$(Se_xS_{1-X})_4$ (x = 0.3) compositional ratios on the monograin powder properties and solar cells, Thin Solid Films. 535 (2013) 35–38. doi:10.1016/j.tsf.2012.10.031.

[84] M. Dimitrievska, G. Gurieva, H. Xie, A. Carrete, A. Cabot, E. Saucedo, A. Pérez-rodríguez, S. Schorr, V. Izquierdo-roca, Raman scattering quantitative analysis of the anion chemical composition in kesterite $Cu_2ZnSn(S_xSe_{1-x})_4$ solid solutions, J. Alloys Compd. 628 (2015) 464–470. doi:110.1016/j.jallcom.2014.12.175.

[85] S.W. Shin, I.Y. Kim, K. V. Gurav, C.H. Jeong, J.H. Yun, P.S. Patil, J.Y. Lee, J.H. Kim, Band gap tunable and improved microstructure characteristics of $Cu\ _2ZnSn(S_{1-x},Se_x)_4$ thin films by annealing under atmosphere containing S and Se, Curr. Appl. Phys. 13 (2013) 1837–1843. doi:10.1016/j.cap.2013.06.022.

[86] Y. Ren, J.J.S. Scragg, C. Frisk, J.K. Larsen, S.Y. Li, C. Platzer-Bjorkman, Influence of the Cu_2ZnSnS_4 absorber thickness on thin film solar cells, Phys. Status Solidi Appl. Mater. Sci. 212 (2015) 2889–2896. doi:10.1002/pssa.201532311.

[87] K. Wang, O. Gunawan, T. Todorov, B. Shin, S.J. Chey, N.A. Bojarczuk, D. Mitzi, S. Guha,

Thermally evaporated Cu_2 $ZnSnS_4$ solar cells, Appl. Phys. Lett. 97 (2010) 2–5. doi:10.1063/1.3499284.

[88] K.-J. Hsiao, J.-D. Liu, H.-H. Hsieh, T.-S. Jiang, Electrical impact of $MoSe_2$ on CIGS thin-film solar cells., Phys. Chem. Chem. Phys. 15 (2013) 18174–8. doi:10.1039/c3cp53310g.

[89] M.T. Greiner, Z. Lu, Thin-film metal oxides in organic semiconductor devices : their electronic structures , work functions and interfaces, NPG Asia Mater. 5 (2013) e55-16. doi:10.1038/am.2013.29.

[90] S. Cong, T. Sugahara, T. Wei, J. Jiu, Y. Hirose, S. Nagao, K. Suganuma, Growth and Extension of One-Step Sol-Gel Derived Molybdenum Trioxide Nanorods via Controlling Citric Acid Decomposition Rate, Cryst. Growth Des. 15 (2015) 4536–4542. doi:10.1021/acs.cgd.5b00790.

[91] D. Hironiwa, N. Sakai, T. Kato, H. Sugimoto, Z. Tang, Impact of annealing treatment before buffer layer deposition on $Cu_2ZnSn(S,Se)_4$ solar cells, Thin Solid Films. 582 (2015) 151–153. doi:10.1016/j.tsf.2014.11.016.

[92] O. Gunawan, T.K. Todorov, D.B. Mitzi, Loss mechanisms in hydrazine-processed $Cu_2ZnSn(Se,S)_4$ solar cells., Appl. Phys. Lett. 97 (2010) 233506. doi:10.1063/1.3522884.

[93] R. Haight, A. Barkhouse, O. Gunawan, B. Shin, M. Copel, M. Hopstaken, D.B. Mitzi, Band alignment at the $Cu_2ZnSn(S_xSe_{1-x})_4$/CdS interface, Appl. Phys. Lett. 98 (2011) 253502–253504. doi:10.1063/1.3600776.

[94] J. Li, M. Wei, Q. Du, W. Liu, G. Jiang, C. Zhu, The band alignment at CdS/$Cu_2ZnSnSe_4$ heterojunction interface, Surf. Interface Anal. 45 (2013) 682–684. doi:10.1002/sia.5095.

[95] B. Vermang, V. Fjallström, X. Gao, M. Edoff, Improved rear surface passivation of $Cu(In,Ga)Se_2$ solar cells: A combination of an Al_2O_3 rear surface passivation layer and nanosized local rear point contacts, IEEE J. Photovoltaics. 4 (2014) 486–492. doi:10.1109/JPHOTOV.2013.2287769.

[96] P. Reinhard, B. Bissig, F. Pianezzi, H. Hagendorfer, G. Sozzi, R. Menozzi, C. Gretener, S. Nishiwaki, S. Buecheler, A.N. Tiwari, Alkali-templated surface nanopatterning of chalcogenide thin films: A novel approach toward solar cells with enhanced efficiency, Nano Lett. 15 (2015)

3334–3340. doi:10.1021/acs.nanolett.5b00584.

[97] R. Kotipalli, B. Vermang, J. Joel, R. Rajkumar, M. Edoff, and D. Flandre, Investigating the electronic properties of Al_2O_3/Cu(In,Ga)Se_2 interface, AIP Adv. 5 (2015) 107101–107106. doi:10.1063/1.4932512.

[98] B. Vermang, J.T. Watjen, C. Frisk, V. Fjallstrom, F. Rostvall, M. Edoff, P. Salome, J. Borme, N. Nicoara, and S. Sadewasser, Introduction of Si PERC rear contacting design to boost efficiency of Cu(In,Ga)Se_2 solar cells, IEEE J. PHOTOVOLTAICS. 4 (2014) 1644–1649. doi:10.1109/JPHOTOV.2014.2350696.

[99] B. Vermang, J.. Wätjen, V. Fjällström, F. Rostvall, M. Edoff, R. Kotipalli, F. Henry, and D. Flandre, Employing Si solar cell technology to increase efficiency of ultra-thin Cu(In,Ga)Se_2 solar cells, Prog. Photovolt Res. Appl. 22 (2014) 1023–1029. doi:10.1002/pip.2527.

[100] B. Vermang, V. Fjällström, J. Pettersson, P. Salomé, M. Edoff, Development of rear surface passivated Cu(In,Ga)Se_2 thin film solar cells with nano-sized local rear point contacts, Sol. Energy Mater. Sol. Cells. 117 (2013) 505–511. doi:10.1016/j.solmat.2013.07.025.

[101] A. Hadipour, R. Müller, P. Heremans, Room temperature solution-processed electron transport layer for organic solar cells, Org. Electron. 14 (2013) 2379–2386.